INFORMATION TO USERS

This manuscript has been reproduced from the microfilm master. UMI films the text directly from the original or copy submitted. Thus, some thesis and dissertation copies are in typewriter face, while others may be from any type of computer printer.

The quality of this reproduction is dependent upon the quality of the copy submitted. Broken or indistinct print, colored or poor quality illustrations and photographs, print bleedthrough, substandard margins, and improper alignment can adversely affect reproduction.

In the unlikely event that the author did not send UMI a complete manuscript and there are missing pages, these will be noted. Also, if unauthorized copyright material had to be removed, a note will indicate the deletion.

Oversize materials (e.g., maps, drawings, charts) are reproduced by sectioning the original, beginning at the upper left-hand corner and continuing from left to right in equal sections with small overlaps.

Photographs included in the original manuscript have been reproduced xerographically in this copy. Higher quality 6" x 9" black and white photographic prints are available for any photographs or illustrations appearing in this copy for an additional charge. Contact UMI directly to order.

Bell & Howell Information and Learning
300 North Zeeb Road, Ann Arbor, MI 48106-1346 USA
800-521-0600

ICE-WEDGE NETWORKS AND "WHALE-HOLE" PONDS IN FROZEN GROUND

A

THESIS

Presented to the Faculty

of the University of Alaska Fairbanks

in Partial Fullfillment of the Requirements

for the Degree of

DOCTOR OF PHILOSOPHY

By

Lawrence J. Plug, B.A.

Fairbanks, Alaska

May 2000

ICE-WEDGE NETWORKS AND

"WHALE-HOLE" PONDS IN FROZEN GROUND

By

Lawrence J. Plug

RECOMMENDED:

Advisory Committee Chair

Department Head

APPROVED:

Dean, College of Science, Engineering and Mathematics

Dean of the Graduate School

4-17-00

Date

Abstract

The patterns of ice-wedge networks and of "whale-hole" ponds in frozen ground self-organize by strong interactions between pattern elements. Mechanisms for the consistent spacing (15-25 m) and orientation between ice wedges are examined in a model encapsulating the opening of fractures under a combination of thermally-induced tensile stress, stress reduction near open fractures, and heterogeneity of frozen ground and insulating snow. Modeled networks are similar to ice-wedge networks on the Espenberg coastal plain, Bering Land-Bridge National Park, Alaska, at the level of variation among Espenberg networks, as indicated by: *i)* comparisons of distributions of relative orientation and spacing between wedges; and *ii)* application of nonlinear spatial forecasting to modeled and Espenberg network patterns. Spacing in modeled networks is sensitive to fracture depth and weakly sensitive to thermally-induced tensile stress and substrate strength, consistent with the narrow range of spacing between natural ice wedges in different regions. In an extended model that includes recurring fractures over thousands of winters, networks similar to natural ice-wedge networks form. The annual pattern of fractures diverges from the ice-wedge pattern, with only ½ - ¾ of wedges fracturing in a single year at a steady state reached after approximately 10^3 y. Short-lived sequences of extreme stress from cooling can permanently alter the spacing between and the fracture frequency of modeled ice wedges, suggesting that the existence and characteristics of existing and relic natural ice-wedge networks reflect extreme, not mean, climate conditions.

"Whale-hole" ponds on the Espenberg beach-ridge plain, approximately 2 m across and 1 m deep and surrounded by raised rings of ice-rich permafrost 2 m across and 0.5 m high, form through an interplay between localized bacterial decomposition of peat, thawing of frozen ground and frost heaving of peat in rings. Groups of hundreds of ponds at Espenberg assemble through time because new ponds are favored to form adjacent to raised rings around existing ponds.

The nonlinear behavior that results from strong interactions in patterns of ice-wedge networks and in ponds suggests general limitations in the application of linear approaches to inferring the response of geomorphic systems to changes in forcing, such as climate change.

Table of Contents

List of Figures

Chapter 1

Chapter 2

Chapter 3

List of Tables

Chapter 1

Chapter 3

For Kaslo

who would love Espenberg

Acknowledgments

Chapters 1 and 2 are manuscripts co-authored with Brad Werner at the Institute of Geophysics and Planetary Physics, Scripps Institution of Oceanography, University of California San Diego (UCSD). My contributions include conceiving of a spatially-extended model for fracture and ice-wedge network development and writing all computer programs used in simulating network development and in analysis and nonlinear forecasting of networks patterns. I wrote the majority of all sections of both manuscripts. Brad provided general modeling advice, suggested many of the ideas explored in both papers and played a large role in improving and organizing the text of both manuscripts.

The work presented in this thesis would not have been possible without the generous funding and support of the National Park Service, Bering Land-Bridge National Park (Espenberg-wetlands subcomponent of the Beringian Shared Heritage Program, to David Hopkins and Lawrence Plug, University of Alaska Fairbanks) and the National Science Foundation, Office of Polar Programs (OPP9530860 to B. T. Werner, UCSD).

I am grateful to David Hopkins at the University of Alaska Fairbanks (UAF) Geology Department for introducing me to the geomorphology of frozen ground regions in general and Espenberg, NW Alaska, in particular. Daniel Mann (UAF Institute of Arctic Biology and Alaska Quaternary Center) has provided friendship, encouragement and opportunities I happily exploited to explore with a shovel the surficial geology of far corners of Alaska.

Brad Werner (UCSD) has provided friendship, a great place to work and imaginative guidance on questions of ice wedges, geomorphology and science in general.

Many people at UAF, Scripps and Espenberg have helped me by providing ideas, critical reviews or shelter in a storm. These include members of my graduate committee at UAF: Jim Begét, Douglas Kane and Owen Mason. For life as a visiting graduate student, I doubt there is a more stimulating and fun place than the Complex Systems Laboratory at Scripps, thanks to past and present members Tom Burnet, Linden Clarke, Jason Foat, Mike Genewich, Mark Kessler, Brad Murray, Jon O'Brien, Michele Okihiro, Karen Scott and Brad Werner. June Champlin, Mary Edwards and Paul Layer at UAF have all been helpful. Perry Weiyouanna and Fred Goodhope Jr., from Shishmaref, Alaska, have been generous neighbors at Espenberg. Buck Maxson, Marc Rouleau, Linda Tae, Kaarin Tae and Tim Tannenbaum rendered cheerful assistance during field work.

I am grateful to the bogs and beach ridges of Espenberg for offering up a few secrets, and to my parents, Peter and Diane Plug, for instilling in me the value of education and drive to do my best. Most of all, my thanks and love go to Kaarin and K&G for their advice, understanding and unstinting support as I have worked on this project.

Introduction and Overview

Arctic and sub-Arctic landscapes commonly are characterized by a suite of patterns that form and are maintained by diverse physical processes, including heat and mass transfer, thermal contraction and fracture, and the phase transition between water and ice. Some patterns form, or are made visually distinctive, by interactions between physical processes and the growth and distribution of tundra vegetation. My goal in this thesis is to examine mechanisms for the origin and characteristics of two specific patterns: those of ice-wedge networks and those of patterns of whale-hole ponds. These patterns are investigated by a combination of numerical modeling and field measurements from the Espenberg region of the Bering Land-Bridge National Park (BELA), NW Alaska. Results of this work bear on the development of the landscape at BELA and frozen ground landscapes in general.

Ice-Wedge Networks

Ice-wedge networks are ubiquitous on lowland landscapes underlain by permafrost, approximately 5-10% of Earth's land surface, where they play a dominant role in determining surface morphology, drainage and patterns of vegetation (French, 1996). During periods in the past two million years when climate was cooler than today, ice-wedge networks formed at lower latitudes on most continents (Black, 1976). Relic troughs and ridges from these now-melted ice wedges persist today. At BELA, active ice-wedge networks, marked at the surface by ridges or troughs arranged in roughly rectilinear patterns, span the ice-rich silty terrain of the coastal plain, the floors of drained

thaw lakes and, in more disorganized form, the troughs between beach ridges at the Espenberg beach-ridge plain.

Ice wedges originate through tension fractures opened in perennially frozen ground that is cooled by falling air temperatures in winter. The cavity of a fracture partly fills with ice from melt water or frost hoar before it closes. Because this ice is weaker than frozen ground, fractures tend to follow the same path in subsequent winters (Lachenbruch, 1962). Whereas this basic mechanism for the initial formation of a single ice wedge has been outlined in field measurements in northern Canada and Alaska (Mackay, 1986), mechanisms for the organization of many ice wedges into networks with a consistent spacing and generally orthogonal orientation between wedges has not been addressed quantitatively.

In Chapter 1, *Fracture networks in frozen ground,* I present a new numerical model that encapsulates mechanics of fracture and the influence of open fractures on stress in adjacent frozen ground. Networks of modeled fractures that self-organize in this model are compared to the plan-view pattern of ice-wedge networks developed in ice-rich silt of the Espenberg Coastal Plain; first by using a new technique that quantifies the angles and spacing between adjacent fractures; and second, by applying an extension of nonlinear one-dimensional (time-series) forecasting methods to the two spatial dimensions of network patterns. The results of this model and comparisons with Espenberg networks suggest that the orderly pattern of ice wedges can be explained by fractures in frozen ground that occur sequentially as the ground is cooled. Open fractures affect stress in the ground and thereby determine the position of subsequent fractures.

The spacing between fractures is sensitive primarily to the depth of fractures and, to a lesser degree, to maximum thermal stress and the tensile strength of frozen ground.

Ice wedges grow from small veins of ice a few millimeters wide to massive wedges up to 5 m wide over hundreds to thousands of years because of the new increments of ice added to wedges each time they fracture (Black, 1976, Lachenbruch, 1962; Mackay, 1986). The relationship between the size and spacing of ice wedges and the winter climate that drives their formation is poorly understood, with understanding and measurements hindered by the long time scales of network development. Nevertheless, properties of modern ice wedges and the relic forms found in currently temperate regions frequently are used as assumed measures of duration and severity of past periods of cold climate (Black, 1976).

In Chapter 2, *The development of ice-wedge networks by annual fracturing,* the development of ice-wedge networks and the growth of individual ice wedges over thousands of winters is considered. The model presented in Chapter 1 is extended to include representation of ice that fills fractures and deformation of the ground surface in response to the growing volume of ice wedges. The spacing between and width of modeled ice wedges that develop under different scenarios for maximum annual stress over thousands of years are examined. The results of this work include: *1)* The characteristics of ice wedge networks, including wedge spacing and width, largely reflect extreme climatic conditions during the formation of the network, not mean conditions. *2)* the existence of relic networks, such as those delineating ice wedges melted long ago over vast expanses of North America, Europe, Asia and southern South America, are not

necessarily indicative of sustained cold climates in these locations during the Pleistocene. *3)* In mature modeled ice-wedge networks, only 35-75% of ice wedges fracture in a given winter. Measurements showing that only 40-70% of ice wedges at sites in northern Canada and Alaska fracture each winter might therefore be consistent with steady climate conditions, and do not necessarily imply warming. *4)* The fate of an individual ice wedge, once formed, depends on its position in the network and on variations in climate-derived thermal stress. Hence, information regarding the conditions under which ice wedges have developed and grown might be contained within the range of ice-wedge widths, and not the bulk properties of ice-wedge networks.

Whale-Hole Ponds

In Chapter 3, I propose a primarily biotic mechanism for the initiation of small ponds in ice-rich, organic permafrost soils on the Espenberg beach-ridge plain in BELA, NW Alaska. These ponds, roughly 2 m across and 1 m deep, are called "whale-hole" ponds because of an Inupiat legend that attributes their origin to whales that breached while swimming beneath the Espenberg spit (Fred Goodhope Jr. and Perry Weiyouanna of Shishmaref, Alaska, personal communication, 1995). Field measurements of the distribution of these ponds and of the stratigraphy of peat exposed in pond walls are consistent with localized bacterial decomposition of peat as the mechanism for pond formation. I argue that formation of the first whale-hole ponds is triggered by micromorphology caused by hummock-forming vegetation that are part of the successional sequence of vegetation on the Espenberg beach-ridge plan.

Whale-hole ponds are surrounded by a ring of raised peat that supports a community of bog vegetation (shrubs and mosses). Rings stand up to 1 m above the surface of the pond and the surrounding wetland. Some of this height is due to bog vegetation on rings, which accumulates peat at approximately twice the rate of sedge and cotton grass that dominates surrounding wetland surfaces at Espenberg. The peat in rings is frost churned and ice-rich, indicating that rings also grow by frost heaving.

On surfaces of young and middle-aged swales of the Espenberg beach-ridge plain (formed 1000-1400 years before present) whale-hole ponds occur in isolation or in small groups. On older surfaces, whale-hole ponds occur in groups of tens to hundreds of ponds with a spacing between ponds of approximately 2 m. Three rule-based numerical models, each representing different hypotheses for this distribution of ponds, are constructed. Results of comparisons between modeled groups of ponds and groups of whale-hole ponds at Espenberg show that this distribution may form because new ponds primarily form adjacent to the raised rings around existing ponds where the accumulation of peat is depressed by persistent snow patches.

The pattern of whale-hole ponds in organic soils of the Espenberg beach-ridge plain is an outstanding example of the spread of a pattern by interactions between elements in the pattern; in this case, the heaving of peat around regions of decomposing peat favors the onset of peat decomposition, and hence the development of a new adjacent pond. Implications of this hypothesis for the beach-ridge landscape at Espenberg include: *1)* As swales at Espenberg age, new ponds will form in swale wetlands. The ongoing development of new ponds might be indicated on the modern Espenberg landscape by

discontinuous moats formed by depressions and shallow regions of decomposing peat around raised rings; *2)* During the mid-Holocene, when no swale surfaces greater in age than approximately 1200 years were present, the wetland landscape at Espenberg was a sedge and cotton grass wetland more uniform than wetland surfaces at Espenberg today, which support sedge and cotton grass vegetation interrupted by patterns of ponds and bog vegetation on raised rings. This constrains the terrestrial resources that were available to early inhabitants of the Espenberg beach-ridge plain, as fresh-water lakes exploited by some water fowl and the fruit of shrubs (especially blueberry and salmonberry) were probably less common than today.

General Conclusions

The patterns of ice-wedge networks and of whale-hole ponds are shown to self-organize through strong interactions between elements of the pattern. In the case of whale-hole ponds, an interaction between frost heave and localized peat decomposition leads to spreading of the pattern of ponds. In the case of ice-wedge networks, their characteristics and their response to climatic forcing reflect an interplay between propagating fractures, annual patterns of open fractures and the long-term evolution of the pattern of ice wedges.

For both these patterns, the nonlinear behavior that results from strong interactions suggest that linear approaches to their study, those approaches that average across the properties of the pattern, are unlikely to capture their important properties or provide a basis for accurate predictions of future behavior. For ponds, for example, a prediction of

future CO_2 flux based on measurements of flux from existing whale-hole ponds is insensitive to the release of CO_2 by the formation and growth of new ponds. The complex and time-dependent behavior under a range of climate scenarios shown by the model suggests the need for caution in inferring the response of ice-wedge networks and other, more complicated geomorphic systems to climate change using simple models or conceptions of their behavior.

References

Black, R.F. (1976). Periglacial features indicative of permafrost: Ice and soil wedges, *Quaternary Research* 23, 3-26.

French, H.M. (1996). "The Periglacial Environment." Addison Wesley, Harlow.

Lachenbruch, A.H. (1962). Mechanics of thermal contraction cracks and ice-wedge polygons in permafrost, *Geological Society of America Special Paper 70,* 69 p.

Mackay, J.R. (1986). The first 7 years (1978-1985) of ice wedge growth, Illisarvik experimental drained lake site, western Arctic coast, *Can. J. Earth Sci. 23,* 1782-1795.

Fracture Networks in Frozen Ground[1]

Abstract

Fractures in frozen ground self-organize into networks through interactions between sequentially emplaced fractures, tensile stress and the developing fracture pattern. From this viewpoint, we model the development of networks on a lattice representing the ground surface on which fractures initiate, propagate and arrest under a combination of uniform thermally-induced tensile stress, stress reduction near existing fractures and stochastic parameterization of heterogeneity in frozen ground and in insulating snow. Tensile stress from cooling, tensile strength, propagation threshold, fracture depth and elastic properties are chosen to approximate properties of frozen ground. Using these parameters, networks assemble with characteristic spacing of 22 m and predominantly orthogonal intersections. Joint distributions of relative orientation and spacing between fractures from modeled networks and ice-wedge networks at Espenberg, Alaska are comparable at the level of variation amongst different ice-wedge networks. Application of nonlinear spatial forecasting to network patterns indicates i) modeled networks can be used to predict Espenberg networks to distances exceeding the characteristic spacing, with prediction error comparable to that of forecasts using another ice-wedge network; and ii) modeled and Espenberg networks form through a similar combination of nonlinear deterministic and stochastic mechanisms. Spacing in modeled networks is sensitive to fracture depth and relatively insensitive to thermally-induced tensile stress. This is

[1]Lawrence J. Plug and B.T. Werner (In revision) *Journal of Geophysical Research.*

consistent with the narrow range of spacing between ice wedges in differing climates. Three-way equant intersections, recurring in modeled and Espenberg networks, form where modeled fractures arrest on the outside of bends in earlier fractures.

Introduction

Networks of interconnected wedges of ice form patterns in perennially frozen ground characterized by consistent spacing and relative orientation between wedges (Figure 1.1). These patterns span lowland Arctic and sub-Arctic tundra landscapes. Similar forms of comparable and larger size have been described on Mars [*Mellon*, 1997].

The development of a network begins when a fracture opens because falling ground temperature gives rise to tensile stress exceeding the strength of frozen ground [*Leffingwell*, 1915]. A fracture initiates at or near the ground surface and propagates in both vertical and horizontal directions [*Mackay*, 1983; 1986] at rates measurable in mh^{-1} [*Knight*, 1971; *Mackay*, 1993a]. Downward opening of the fracture is limited by decreasing tensile stress with depth and changes in properties of the frozen ground. The direction of horizontal propagation can change in response to patterns of stress resulting from neighboring open fractures [*Lachenbruch*, 1962] and heterogeneity in frozen ground and snow depth. The fracture arrests where it intersects an earlier open fracture or where the rate of strain energy released through propagation falls below a threshold dependent on properties of frozen ground. By modifying tensile stress in the surrounding ground, an open fracture affects the position and orientation of subsequent fractures [*Lachenbruch*, 1962; 1966]. Ice can fill the cavity of the fracture by frost hoar or infiltration of water

from melting snow that then freezes, preventing closure of the fracture through rising ground temperature in spring or through inelastic creep [*Black*, 1974; *Mackay*, 1986]. In subsequent winters, fractures generally follow the same path [*Mackay*, 1974; 1986] because this vein of ice is weaker than the surrounding frozen ground. Repeated cycles of fracture and filling of cavities by ice lead to growth of ice wedges that locally deform frozen soil. The resulting surface morphology reveals the location of fracture paths below.

Whereas these mechanisms for fracture of frozen ground and development of ice wedges are well documented, no quantitative model that treats the temporal and spatial development of networks has been attempted. Such a model could be used to quantify relationships between properties of relict network patterns in present-day temperate regions that were underlain by permafrost during Pleistocene glacial periods [e.g., *Johnson*, 1990] and the conditions under which these networks formed. Such a model could also be used to evaluate differing mechanisms for angles of intersections between fractures, which have been hypothesized to vary systematically between networks [*Black*, 1952; *Lachenbruch*, 1966; *French*, 1996 p. 94].

An alternative to treating the temporal and spatial development of networks is to attempt to infer macroscopic properties of networks, namely spacing and relative orientation between ice wedges, from the effect of a single, infinitely long fracture on stress in the surrounding frozen ground. Calculations of this stress at the ground surface, assuming that the tensile strength of frozen ground is 95% of the prefracture stress, have been used to predict the position where a new, parallel fracture initiates [*Lachenbruch*,

1961, 1962; *Al-Moussawi*, 1988]. This prediction for spacing is consistent with diameters of polygonal regions formed by interconnected ice wedges, but its value is sensitive to parameters with large uncertainties, such as those characterizing rheology and distribution of flaws in frozen ground. In addition, propagating fractures near a single, open fracture bend toward a path normal to the axis of the open fracture, which is the axis of maximum principal stress [*Lawn*, 1993, p. 47]. Therefore, intersections between wedges are predicted to be orthogonal [*Lachenbruch*, 1962; 1966], as is commonly observed for ice-wedge networks and other patterns generated by tension fracture (*e.g.*, desiccation cracks).

One difficulty with an approach based on initiation of a new fracture parallel to a single straight fracture is that this condition probably is rarely realized for fractures that lead to ice wedges. Initiation at an orientation parallel to a single fracture is unlikely to occur under a prefracture thermal stress that is isotropic, because the axis of the new fracture would lie parallel to the maximum component of the residual anisotropic stress resulting from the earlier fracture. Moreover, new fractures are added to a pattern of existing fractures [*Mackay*, 1986] as stress increases in frozen ground; those fractures that determine the spacing between ice wedges, being among the last to be added to a pattern, initiate in the context of many existing fractures. Even the earliest fractures in newly frozen ground are not straight [*Mackay*, 1986] because they propagate through heterogeneous frozen ground and nonuniform stress.

A second difficulty with this approach is that fracture paths in networks might be determined principally by horizontal propagation rather than by initiation position: for

example, spacing and lengths of fractures in linear networks in rock are sensitive to propagation, not initiation, characteristics [*Renshaw and Pollard*, 1994; *Olson*, 1993]. Once initiated, a fracture continues to propagate as long as the rate at which stored strain energy released through propagation exceeds the energy expended in forming new fracture surfaces at the tip [*Irwin*, 1958]. Because the energy required to drive a fracture tip forward is supplied by strain along the fracture, which is a function of prefracture stress and fracture length, fractures can propagate into regions near open fractures where tensile stress is insufficient for initiation.

If ice-wedge networks develop through sequential initiation and propagation in heterogenous frozen ground and the placement of individual fractures is influenced by surrounding open fractures, then the large-scale ordering of the network results from local interactions among the fractures, a hallmark of self-organization [*Nicolis and Prigogine*, 1977]. Quantifying the implications of this self-organization hypothesis for the morphology of networks and for their sensitivity to material and climatic conditions requires a model for the dynamical development of a network.

An appropriate time scale with which to model the development of a network is that associated with the emplacement of a single fracture, the path of which comprises the set of dynamical variables in the model. In open nonlinear systems, coupled variables with widely dissimilar intrinsic time-scales can develop an asymmetrical relationship, with the long-term behavior of fast variables following, or being slaved by, that of slow variables [*Haken*, 1983]. In these cases, common for pattern forming systems such as landforms, the dynamics of slaved fast variables can be abstracted into minimal rules [*Werner*, 1995;

1999]. We present a model for ice-wedge network development in which sets of simple nondynamical rules encapsulate the initiation and propagation of individual fractures and the effect of emplaced fractures on stress, controlled by the more slowly developing pattern of open fractures. Inherent in this approach are the assumptions that precise determination of the effect of open fractures on stress is irrelevant and that network morphology transcends details of short-time-scale fracture tip behavior.

Properties of Ice-Wedge Networks

Ice-wedge networks share four primary properties that constrain models for their development.

1. Ice-wedge networks require perennially frozen ground and low and rapidly falling winter temperatures. Other than these general conditions, the occurrence of ice-wedge networks is insensitive to *i)* the composition of frozen ground, as networks form in a broad range of substrates, including poorly drained silt and colluvium and, less commonly, weathered bedrock, cobbles, coarse sand, gravel and clay [e.g., *Black*, 1974; *Mackay*, 1995]; *ii)* mean annual temperature, as networks form in regions with a wide range of mean annual temperatures below -4 to -6 °C [*Péwé*, 1966; *Burn*, 1990]; *iii)* winter temperature extremes, as fracturing in ice wedges has been measured at daily mean air temperatures ranging from -15 to -35 °C and during cooling rates of 1.8 to 10 $^{\circ}C\ day^{-1}$ over one to several days [*Lachenbruch*, 1962; *Mackay*, 1993b].

2. Individual ice wedges are tens to hundreds of meters in length and most terminate at an intersection with another wedge [*Black*, 1952]. Most wedges in non-aggrading sediment penetrate 4 - 6 m below the ground surface [*Black*, 1974].

3. Intersections between ice wedges are principally orthogonal in most networks [*Black*, 1952; *Lachenbruch*, 1962]. However, many non-orthogonal intersections have been reported in some networks [*Leffingwell*, 1919; *Black*, 1952]. The overall orientation of most networks with orthogonal intersections is random, but some networks adjacent to lakes and rivers have orientation following that of the shoreline [*Black*, 1952; *Lachenbruch*, 1966].

4. Interconnected ice wedges enclose regions that range in shape from squares, parallelograms and crude hexagons to incompletely closed figures. The diameter of these regions ranges from 5 to 80 m, with most lying between 15 and 30 m [*Black*, 1974].

Fracture in Frozen Ground and Ice Wedges

Fracture that leads to development of ice wedges is driven by tensile stress in a shallow layer near the ground surface. This tensile stress results from decreases in air temperature and corresponding strains too rapid for significant compensation by inelastic creep [*Lachenbruch*, 1962]. Air temperature changes of the magnitude and duration of those correlated with fracture episodes [*Mackay*, 1993b; *Allard and Kasper*, 1998] are sharply attenuated with depth in the ground; significant tensile stress therefore occurs only at depths less than approximately 1 m [e.g. *Lachenbruch*, 1962]. Fractures in new, developing permafrost (in a recently drained lake basin) have been observed to initiate at

the ground surface [*Mackay*, 1986]. Most fractures in ice wedges initiate at the top of the wedge (0.2 to 1.0 m below the ground surface) because ice in wedges is significantly weaker than frozen ground [*Lachenbruch*, 1962; *Mackay*, 1983]. Fractures propagate to a depth below the layer in which thermally-induced stress is significant; however, this depth is approximately uniform within most networks and similar between networks. Fractures in new permafrost reach depths of 2 to 3 m, comparable to the depth of the frozen (and hence brittle) layer [*Mackay*, 1986; *Yershov*, 1998 p. 193]. Fractures in ice wedges consistently reach depths of 3 to 5 m [*Mackay*, 1974; *Black*, 1974], similar to the depth of the wedge. Because fractures propagate to similar depth and are driven by stress in a thin layer at the ground surface, fracture in permafrost can be approximated as a two-dimensional (plan view) phenomenon.

Individual fractures open asynchronously in both frozen ground and ice wedges. In frozen ground, new fractures occur sporadically throughout winter and remain open as subsequent fractures propagate [*Mackay*, 1986]. The paths of these fractures are maintained from year to year because most cavities fill with ice before closing and that portion that is below the seasonally thawed layer does not melt. In subsequent winters, fractures generally recur within centimeters of the longitudinal axis of these veins of ice before new fractures open elsewhere in frozen ground [*Mackay*, 1986]. Synchronous fracturing rarely is observed in ice wedges [*Mackay*, 1974]. Because fractures in frozen ground affect patterns of tensile stress, preexisting fractures determine the initiation and propagation of subsequent fractures. Therefore, the development of an ice-wedge

network can be treated approximately as the sequential initiation and propagation of fractures under the influence of existing fracture paths through their effect on stress.

Model

Overview

If fractures are emplaced sequentially in a network, the fast-time-scale dynamics of initiation and propagation are slaved to slower-time-scale evolution of the network and its associated stress field, suggesting that the mechanics of fracture need not be treated in detail. Network evolution can be modeled using a minimal abstraction of fracture mechanics, retaining only those characteristics that persist over longer temporal scales [*Werner*, 1999]: principally, the effect of the tensile stress field caused by open fractures on the propagation of a new fracture. Our hypothesis for this abstraction, described below, can be tested by comparing the model to measured networks. The abstraction given here probably is not minimal; suggestions for paring the abstraction are given in the discussion section.

In the model, fractures initiate and propagate one at a time on a two-dimensional periodic lattice of square cells representing the ground surface. Cells in the lattice either are unoccupied or can be irreversibly transformed into a fracture segment characterized by an angle specifying the direction in which a fracture propagated through the cell. An iteration begins with initiation of a fracture at a position and orientation in the lattice where tensile stress exceeds a minimum threshold that is uniform throughout the lattice. The fracture propagates in two approximately opposing directions by successively

extending to cells neighboring those at the two fracture tips. The cells entered by a fracture tip are determined by patterns of modeled stress owing to earlier fractures and by random heterogeneities. Each tip of the propagating fracture arrests independently where propagation becomes energetically unfavorable or upon encountering a cell already containing a fracture segment. The length of fractures is limited to 50% of the edge length of the lattice to prevent the first few fractures in a network from propagating beyond one edge of the lattice and reappearing on another edge repeatedly because of periodic boundaries. Beyond the first few model iterations, the length of fractures in modeled networks is not sensitive to this value. For example, only 8 out of 700 modeled fracture tips on a 400×400 m lattice were artificially arrested. A fracture persists on the lattice and affects the modeled tensile stress that determines the initiation and propagation of subsequent fractures. The next iteration of the model begins with the initiation of a new fracture.

Initiation

Macroscopic fractures in natural materials, such as those that give rise to ice wedges in frozen ground, initiate at flaws [*Ingraffea*, 1987]. These can occur in frozen ground because of voids, discontinuities in properties of frozen ground at geologic contacts or at loci of ice segregation processes [e.g., *Tsytovich*, 1975] and through accumulated effects of strain without fracture [*Al-Moussawi*, 1988]. If flaws are small and distributed uniformly and densely, the position and orientation of fracture initiation might be unrelated to their position. Alternately, widely spaced flaws might determine initiation

position but not the angle of subsequent macroscopic extension beyond the zone of the flaw, because propagating fractures generally adopt an orientation independent of orientation of an initial small flaw [*Cotterell and Rice*, 1980; *Lawn*, 1993 p. 49]. Finally, the position and orientation of large widely-spaced flaws, such as those at substrate discontinuities, might determine both initiation position and the initial direction of propagation.

In the model, the potential influence of flaws on initiation is parameterized by selecting the cell, *ij*, and initial orientation of the fracture, θ, according to one of three strategies that correspond to the cases outlined above: *i)* select the cell and orientation that maximize tensile stress across the initial fracture segment; *ii)* select a cell randomly but set the orientation of the first fracture segment perpendicular to the axis of maximum principal stress; or *iii)* randomly select both cell and orientation.

Propagation

Fractures in frozen ground propagate by converting stored strain energy, released by relative motion of the fracture surfaces, into the work required to form new fracture surfaces. For a fracture to continue to propagate, the rate at which strain energy is released per unit area of new fracture, G, must exceed a material-dependent minimum energetic threshold, G_O: $\Delta G = G - G_O > 0$. For materials such as frozen ground, ice and metals, G_o is a function of the surface energy of the material and work in inelastic deformation in a small zone at the fracture tip. Assuming planar fractures and purely

elastic deformation of the frozen ground surrounding the fracture, G can be expressed as [*Irwin*, 1958; *Lawn*, 1993 p. 29]

$$G = \left((K^t)^2 + (K^s)^2\right)\left(\frac{1-\upsilon^2}{E}\right), \tag{1}$$

where υ and E are the Poissons coefficient and elastic modulus of frozen ground and K^t and K^S are stress intensity factors that specify the amplitude of tensile and shear stress near the fracture tip, respectively.

A propagating fracture bends toward an orientation that maximizes the rate at which strain energy is released [*Lawn*, 1993 p. 47]. Under purely tensile stress, a fracture tends to continue along its original plane. Under an imposed shear stress, a fracture deflects away from its original plane toward the orientation that minimizes shear stress across the plane of the fracture. Fractures also can bend because of nonuniformity in stress or material heterogeneity.

In the model, a fracture propagates through cell kl if $\Delta G_{kl} > 0$. The propagation direction is reevaluated following the addition of each new fracture segment, with a tendency to select a change in propagation direction, $\Delta\theta$, that maximizes $\Delta G_{kl}(\theta+\Delta\theta)$. The effect of sub-cell scale material and stress heterogeneity is parameterized by setting the probability of $\Delta\theta$, $P(\Delta\theta)$, proportional to a Boltzmann distribution, specifically:

$$P(\Delta\theta) \propto e^{\left(\frac{\Delta G_{kl}(\theta+\Delta\theta)}{\Delta G_{random}}\right)}, \tag{2}$$

where the value of ΔG_{random} determines the magnitude of random variations in G resulting from small-scale heterogeneities.

The stress intensity factors for a fracture tip, K^t and K^s, depend on the length of the fracture, the distribution of prefracture stress along the fracture path and the geometry of the surrounding boundaries. Under non-uniform loading, $K^{(t,s)} \approx L^{1/2} \int_0^L \tau(x) Y(L,x)\, dx$, where x is a distance along the fracture path, L is a characteristic fracture dimension and Y is a function that weights stress, $\tau(x)$, along the fracture path and depends on boundaries and geometry of a fracture [*Bueckner*, 1970; *Rice*, 1972]. In the model, the tensile and shear stress intensity factors for a fracture tip entering a cell kl are approximated as

$$K^t_{kl} = \left(L_{kl}/\pi\right)^{1/2} \sum_{ij \in [F_{kl}]} \tau^t_{ij} s_{ij} \Big/ \left(L_{kl}^2 - L_{ij}^2\right)^{1/2} \qquad K^s_{kl} = \tau^s_{kl} \sqrt{\pi\, s_{kl}}\ , \tag{3}$$

where τ^t_{ij} is the prefracture tensile stress perpendicular to the fracture segment in cell ij, ij are members of the set of previously opened segments on the current fracture, $[F_{kl}]$, and τ^s_{kl} is the shear stress across the plane of the fracture in the current cell, kl. L_{kl} is the half-length of the fracture as it enters the cell kl and s_{ij} and s_{kl} are the lengths of fracture segments in cells ij and kl. Equation (3) overestimates K^t and hence G (Equation 1) for fractures in frozen ground, because the finite depth of fractures limits strain and hence stress concentration at the propagating tip. An alternative approach is to further weight

values of τ^t_{ij} as a function of position, favoring those closest to the fracture tip. The effect of this overestimate on results is discussed in the section on the sensitivity of modeled networks to parameters.

Stress

The stress in frozen ground crossed by fractures is a complicated combination of tensile stress from thermal contraction and from spatial variations in stress, proportional to thermal stress, arising from open fractures. Overlaid on this are variations owing to temperature and material-varying rheology of frozen ground [e.g., *Goughnour and Andersland*, 1968; *Ladanyi et al*, 1981]. In general, strain resulting from the opening of a fracture both reduces and imposes anisotropy on stress in the surrounding frozen ground. The reduction in stress rapidly decreases with distance from a fracture; for a finite straight fracture in an elastic, isotropic material under uniform tensile loading, contribution from displacement at the fracture approximately decays as d^{-2}, where d is the distance from the fracture center [*Pollard and Segall*, 1987]. The orientation of the axis of maximum principal stress depends in a complicated way upon position, applied stresses, boundaries and the width of the fracture [*Pollard and Segall*, 1987]. In the simpler case of an infinitely long straight fracture, the reduction in stress parallel to the fracture is the product of the reduction in stress perpendicular to the fracture and Poissons coefficient [*Lachenbruch*, 1962], which can vary for frozen ground as a function of grain size and decreases sharply with decreasing temperature. For frozen silt, Poissons coefficient decreases from 0.35 at -0.3°C to 0.13 at -4.0°C [*Tsytovich*, 1975]. Because of

the low temperature at which fractures occur in frozen ground, the reduction in stress along the plane parallel to an open fracture probably is insignificant.

In the model, the far-field stress affecting the initiation and propagation of fractures is a uniform, isotropic tensile stress, τ_o, modified by neighboring open fractures. This modification in stress is approximated by summing linearly over all open fracture segments, giving

$$\tau_{kl} = \tau_o \left(1 - \sum_{ij} R_{ijkl} \right) , \tag{4}$$

where τ_{kl} is the tensile stress in the cell *kl* projected across the angle θ. A simple representation of the reduction of stress by a fracture segment is employed that exhibits the following features: a power law decrease with distance and maximum reduction perpendicular to the fracture. Specifically, R_{ijkl} is the fraction of stress across the plane θ at cell *kl* that is relieved by the fracture segment in cell *ij* and is approximated as

$$R_{ijkl} = \frac{C}{\left(d_{ijkl} \right)^{\eta}} \cos(\beta_{ijkl}) \sin(\alpha_{ijkl}) , \tag{5}$$

where d_{ijkl} is the distance from the center of cell *ij* to the center of cell *kl*, β_{ijkl} is the difference between the angle of the fracture in cell *ij* and the angle across which stress is projected in cell *kl*, and α_{ijkl} is the angle between the line segment connecting cell *kl* and cell ij and the normal to the fracture segment in cell *ij* (Figure 1.2). *C* is a scaling factor that depends on cell size and fracture depth and η is the exponent specifying the decay of

stress relief with distance from a fracture. Patterns of stress modeled using this function are shown in Figure 1.3.

Equations (4) and (5) do not account for the shadowing effect of an open fracture on the stress relief of a second, more distant, open fracture; this shadowing arises because stress relief from a fracture is not transmitted across the discontinuity of another fracture. Inclusion of shadowing imposes a severe computational cost (roughly an order of magnitude). The influence of shadowing is minimal in most cases because of a combination of a large background stress, monotonic decrease of stress relief with distance and the dependence of stress relief on orientation (nearby fracture segments that would be shadowed generally are oriented normal to the direction of propagation: $\alpha \approx 0$). The measured difference between the median spacing between fractures for modeled networks with and without shadowing is less than 5%.

Reference Model

Parameters of the reference model, some poorly constrained, were chosen to approximate measurements of frozen ground during periods when fracture occurs.

Calculated values for prefracture tensile stress owing to cooling are sensitive to assumptions regarding the rheology of frozen ground, which is a function of ice content, size of soil particles, temperature and unfrozen water content [*Ladanyi* et al., 1981; *Bragg and Andersland*, 1981]. One calculated value, 1.6 MNm^{-2}, is based on a viscoelastic deformation law for frozen ground at high stresses, a sustained rate of cooling of approximately 10 °C day^{-1} at the ground surface over durations of one to several days

and a mean absolute surface temperature of -25 °C [*Lachenbruch*, 1962]. Tensile stresses can be expected to be comparable to but slightly above the tensile strength of freshwater ice, which has values of 1 to 2 MNm^{-2} at loading rates greater than about 10^{-5} s^{-1} [*Gold*, 1977], because lake ice generally fractures only during extreme winter cooling events [*Lachenbruch*, 1966]. Therefore, τ_o is set to 2 MNm^{-2} in the reference model.

The parameters governing the effect of modeled fracture segments on stress (Equation 5) are set to $\eta = 2$ and $C = 3$ so that modeled stress perpendicular to a long straight fracture approximates the solution to two-dimensional elastic equations for stress at the ground surface in a plane perpendicular to an infinitely long, 5 m deep straight fracture [*Lachenbruch*, 1961; *Plug and Werner*, 1998].

The measured strength of frozen ice-saturated silt in uniaxial tension is approximately 0.9 MNm^{-2} at -5 °C [*Zhu and Carbee*, 1987]. Measured values for sandy silt and fine sand are comparable, whereas gravelly substrates have measured tensile strength of approximately 0.1 MNm^{-2} [*Sayles*, 1991]. Although properties of frozen ground vary with temperature, ice content, loading rate and sample size, as well as grain size, tensile strength is relatively insensitive to temperature and strain rate [*Andersland and Ladanyi*, 1994 p. 146]. A value of 1 MNm^{-2} is selected as the minimum tensile stress at which a modeled fracture can initiate.

In the reference model, the cell where a modeled fracture initiates is chosen at random but the initial orientation of the fracture is perpendicular to the axis of maximum tensile stress for that location.

To our knowledge, no measurements of G_o for frozen ground have been conducted. For ice, G_o has been measured to range from 5 Jm^{-2} to greater than 10 Jm^{-2} at temperatures of -16 to -20 °C [*Goodman and Tabor*, 1978], with G_o tending to increase with temperature. These measured values for G_o far exceed the surface energy of the ice-vapor interface, 0.24 Jm^{-2} (which would equal G_o if ice were perfectly brittle), indicating a large contribution to G_o from plastic deformation in the small zone around the tip. As the unfrozen water content is greater at a given temperature in frozen ground than in ice, the work expended in the plastic zone at a fracture tip probably is greater in frozen ground. Because propagation in frozen ground therefore is assumed to require a greater energy input, a value of 20 Jm^{-2} is used in the reference model. In calculations of the energetic cost of propagation, fractures are assumed to penetrate to a fixed depth of 5 m, approximately the depth of ice wedges and fractures in ice wedges.

In calculations of G, stress is assumed to be vertically uniform to a depth of 1 m. This value supported by the calculation (based on a formula from *Birch* [1948]) that a 10°C step-function decrease in ground surface temperature is attenuated after one day to 80% of its original magnitude at a depth of approximately 1 m (assuming a thermal diffusivity of 5 x 10^{-6} m^2s^{-1}, comparable to that for frozen silty clay to sandy loam at temperatures below -5°C [*Williams and Smith*, 1991 p. 93]).

A value of 5 Jm^{-2} is used for G_{random} (appearing in the Boltzmann factor for fracture orientation) so that modeled fracture paths under a uniform, isotropic stress are similar to the meandering paths of isolated fractures in frozen ground.

Reference Model Networks

In our reference model, networks emerge through sequential addition of fractures (Figure 1.4). The character of fracture paths changes as the network evolves. The first few fractures propagate through regions of largely isotropic and uniform stress because fractures are widely spaced. Paths followed by these initial fractures are characterized by irregular, gentle bends resulting from small deflections of the fracture tip by random variations in G, as modeled with a Boltzmann distribution (Figure 1.4a-b). As the number of fractures increases, the paths of fractures become correspondingly more influenced by neighboring fractures and the length of individual fractures decreases as the network is increasingly dissected (Figure 1.4c). The paths of later fractures are determined by strong anisotropy in stress induced by neighboring fractures; some later fractures form small-radius-of-curvature bends near intersections and others follow short, straight paths perpendicular to the longer fractures that first dissected the lattice (Figure 1.4d).

Most fractures in modeled networks terminate on other fractures at approximately orthogonal intersections. The first few fractures are artificially terminated at the imposed maximum fracture length. Only a few fracture tips, generally those of fractures that are among the last to be added to the network, arrest because $G < G_o$ before intersecting another fracture; specifically, four fracture tips were arrested in this manner in a 400 × 400 m network. Most intersections in modeled networks are orthogonal.

In steady-state networks (those where stress is below strength throughout the lattice), fractures bound multi-sided regions of generally consistent size. The average spacing

between parallel fractures of these closed forms is approximately 22 m. Although enclosed forms display a range of shapes, most are rectilinear and equidimensional.

The characteristics of steady-state modeled networks are sensitive to the size of the simulation space when the edge length of the lattice is less than approximately ten times the mean spacing between fractures. Mean spacing and variations in spacing between fractures are larger in small networks; orientation of small networks can be dominated by the absolute orientation of the first fracture. To avoid artifacts of finite lattice size, a simulation space at least as large as 300 × 300 m is used in all modeled networks discussed here.

Ice-Wedge Networks

Ice-wedge networks on the upland coastal plain of the Seward Peninsula, Alaska (Figure 1.5) are compared to modeled networks because active, well-developed, visually clear networks occur there in areas having uniform substrates in which isotropic stress is assumed to prevail. In this region, near the mouth of the Espenberg River (commonly referred to as Espenberg [*Schaaf*, 1998]), relief is subdued, less than ten meters, suggesting that pronounced spatial variability in temperature or precipitation is unlikely. Sediments are ice-rich silt, some deposited as loess and some reworked in thaw-lake deposits, capped by a shallow layer of peat [*Hopkins*, 1982]. Ice wedges form continuous networks on upland surfaces and in the shallow basins of naturally drained lakes. The position of ice wedges is revealed on the ground surface by ridges 0.25 to 1 m high and up to 3 m across, which are inhabited by shrubs and mosses that favor dry soils. The low,

flat surfaces between these ramparts are flooded during the spring and summer and are occupied by wet sedge-tundra vegetation. These moisture and vegetation differences make ramparts distinctive in 1:6000 scale near-infrared aerial photographs (Figure 1.1).

The modern climate at Espenberg is consistent with estimates of prefracture thermal stress in frozen ground employed in the reference model. Climatic conditions at Espenberg are similar to those at Kotzebue, the nearest permanent meteorological station, which is located 40 km to the east at a similar altitude and distance from the coast [*NOAA*, 1999; *WRCC*, 1999]. The average daily minimum temperature during December through March is -23°C; daily minima can be as low as -47°C. Conditions suitable to cause fracturing often occur. Diurnal fluctuations in air temperature of 10°C or more during periods of absolute temperature below -18°C are common during November through February. For example, cooling episodes of this intensity occurred 3 - 5 times in each of these months during the winter of 1997-98. The depth of accumulated snow is shallow; the 30 y average snow depth reaches an annual maximum in late April of approximately 0.5 m and is below 0.25 m for November and December. Strong winds can blow the ground clear of snow. Gusts greater than 32 kmh^{-1} lasting up to 2 minutes occur most days during the winter months (all climatological data from *WRCC* [1999]).

The Seward Peninsula was located near the middle of the mostly unglaciated Beringian subcontinent during the last glaciation [*Hopkins*, 1982]. Some ice-wedge networks there consequently have had a long time to develop under conditions that may range from colder and dryer than present during the Last Glacial Maximum to warmer during the early Holocene. To address the possibility that differences in ages of networks

might affect their characteristics, networks considered here are drawn from upland surfaces and the basins of drained lakes within the upland, which are presumably younger than surrounding uplands. Although some variations are observed, the spacing between ice wedges in these two types of networks is not consistently different, suggesting that the influence of surface age is not significant.

Ten 450 × 450 m regions of ice-wedge networks were selected from areas where networks are not visibly oriented with respect to a neighboring riverbank or lake shoreline. The positions of ice wedges were recorded by manual digitization of 1:6000 scale near-infrared aerial photographs using moisture and vegetation differences of ramparts to delineate the network pattern (Figure 1.6). Ice wedges that have not caused visible surface deformation or localized changes in soil moisture and vegetation, because of infrequent fracture, might be missed using this procedure. However, good correlation between the scale of surface deformation and the size of an underlying ice wedge has been found in exposures of ice wedges at river banks and lake- shore bluffs at Espenberg and has been reported for other regions of ice-wedge terrain [*Mackay*, 1974].

Comparisons of Espenberg and Modeled Networks

Methods

New statistical metrics are required for performing quantitative comparisons between modeled and the natural Espenberg networks and for characterizing the properties of irregular network patterns (Figure 1.6). Single measures of length scale, such as the mean distance between parallel fractures [*Lachenbruch*, 1966], do not include information on

scatter nor on the distance between fracture segments that are not parallel. Two-dimensional power spectra cannot capture many of the geometrical properties of networks, because of insensitivity to details of relative orientation between fracture segments in neighboring fractures. Categorization of networks as orthogonal or nonorthogonal based on the relative orientation between ice wedges near intersections [e.g. *Black*, 1952; *Black*, 1974; *French*, 1996 p. 94] does not quantify intersection angles and is insensitive to orientation of paths that are not close to intersections.

To address these difficulties, measurements of the distributions of fracture spacing and relative orientation over a network region are required. This is accomplished by measuring the spacing and relative orientation between successive fractures along sample lines that dissect a network at randomly selected angles and originate from randomly selected locations (Figure 1.7). Spacing is the distance between two successive intersections between the sample line and fractures, measured along the sample line. Relative orientation is the absolute value of the angle between successive fractures (ranging from 0° to 180°). Measurements collected where a sample line crosses the same fracture twice in close succession (these have spacings of less than 5 m and relative orientations less than 10°) are rejected, because the digitization procedure for Espenberg networks is insensitive to small-scale meandering of a fracture.

Binned distributions of spacing and relative orientation from different networks are compared using two-sample, two-dimensional Kolmogorov-Smirnov (K-S) tests. The essence of the K-S test is to characterize the difference between two distributions using the maximum value of the difference between the corresponding cumulative distributions

[*Peacock*, 1983]. For each bin in a two-dimensional distribution, the cumulative distribution is taken to be the sum of the values in the bins at smaller spacing and smaller relative orientation, *i.e.*, the quadrant to the upper left of a selected bin in Figure 1.8a-d. Then, the maximum difference between the cumulative distributions is found. This procedure is repeated for the other three quadrants, with the overall maximum of the cumulative differences, normalized by square root of the number of observations, Z, retained [*Fasano and Franceschini*, 1987]. The probability, P, that two sets of samples are not drawn from different distributions is estimated by comparing Z to published results of Monte Carlo tests using synthetic normal distributions [*Smallwood*, 1996]. If $P < 0.001$, the two distributions are significantly different, whereas $P > 0.20$ implies there is no detectable difference between the two distributions [*Smallwood*, 1996].

Although the binned K-S test is very nearly independent of number of observations when observations are drawn from joint normal distributions [*Smallwood*, 1996], it is sensitive to measurements of relative orientation and spacing collected along sample lines because correlated measurements are introduced as sample size increases. This exaggerates the difference between two distributions because the K-S test becomes more rigorous although no new information has been added. To avoid this difficulty, sample size is selected by finding the inflection point in $P(Z)$ as a function of numbers of measurements. This corresponds to 1000 observations from each network for the comparisons presented here.

The characteristic spacing of fractures in a network, D, is taken to be the median value of the unbinned spacing measurements. For example, for periodic networks of squares or hexagons, D is the distance between parallel sides.

One-dimensional distributions of relative orientation between successive fracture segments are bimodally distributed with peaks at 0° and 90° for the Espenberg and reference model networks. These distributions are biased toward small angles because sample lines are less likely to pass through those pairs of neighboring fracture segments that have relative orientations near orthogonal than those near parallel. The effect of this bias is removed by normalizing the angle distributions drawn from networks against a distribution drawn from randomly placed lines with random lengths similar to lengths of individual fractures in reference model networks. The degree to which successive fractures along a sample line are orthogonal and parallel is characterized by three values drawn from a least-squares fit of the relative orientation distribution to the sum of two normal distributions centered at 0° and 90°: O, the standard deviation of the peak at 90°; P, the standard deviation of the peak at 0°; and, R, the ratio of area under the normal distribution at 0° to area under the normal distribution at 90°. For example, as measured for a network of squares, O and P are both 0 because all values of relative orientation are either 90° or 0°. R for squares is 1.5. For a network of randomly placed lines, $O \approx P \approx$ 55° and $R \approx 1$.

Results

Properties of networks are revealed by joint distributions of the spacing and relative orientation between fractures, as illustrated for the mean distributions over the two sets of networks (Figure 1.8a-b) and for selected Espenberg and reference model networks (Figure 1.8c-d). Peaks centered around a spacing of 22 m at 0° in both reference model and Espenberg networks indicate the typical spacing of parallel fractures. The predominance of orthogonal intersections in Espenberg and reference model networks is shown by peaks in the distributions at small spacings around 90°, which extend in ridges out to approximately the spacing between parallel fractures.

K-S comparisons of the joint distributions reveal that some of the ten measured Espenberg networks are statistically consistent with some of twenty realizations of the reference model (Table 1.1). The variation between individual Espenberg networks and individual reference model networks is similar to the variation within Espenberg networks and within modeled networks. Variations within modeled networks are probably attributable to the influence of the first long fractures. Variations amongst Espenberg networks might arise in a similar manner, but also are correlated with variations in the spacing, D. A comparison of mean distributions from Espenberg with reference model networks has variation comparable to the mean of individual network comparisons. These comparisons amongst distributions, although widely variable between networks, are consistent with the hypothesis that reference model and Espenberg networks are drawn from the same ensemble.

The characteristic spacing and relative orientation between fractures are similar in Espenberg and reference model networks (Table 1.2). Both modeled and Espenberg networks are strongly orthogonal. Most orthogonal relative orientations for modeled and Espenberg networks occur at distances well below the characteristic spacing between fractures (Figure 1.8). For modeled networks, this orthogonality results from sequential emplacement of fractures and the tendency of fractures to bend toward an orientation perpendicular to the axis of maximum principal stress, which is orthogonal to an existing fracture as it is approached. This increase in orthogonality close to intersections for both modeled and Espenberg networks is in conflict with mechanisms proposed to explain apparently equant, non-orthogonal intersections, such as branching [*Yoffe*, 1951] of fast-propagating fractures [*Lachenbruch*, 1962] or initiation of multiple fractures at a single point [*Black*, 1952; *French*, 1996 p. 96].

Whereas orthogonality of fractures in networks can be attributed to stress around a single fracture, the tendency toward parallel orientation between fractures arises in the model through a three-step sequence of fracturing: i) initial fracture; ii) fracture orthogonal to the first; and iii) fracture orthogonal to the second. Because the emplacement of a parallel fracture depends on two orthogonal emplacements, networks should always be less parallel than orthogonal, in agreement with measured values of O and P for both Espenberg and modeled networks (Table 1.2).

Evaluating Network Properties with Forecasting

The placement of new fractures in modeled networks is influenced by existing neighboring fractures, the existing path of the current fracture and stochasticity representing heterogeneity introduced in both initiation and propagation. The need to characterize the relative contribution of these deterministic and stochastic processes to the network pattern, particularly for natural networks, is analogous to a similar problem for chaotic time series, which has been addressed with methods for time-series forecasting [*Abarbanel* et al., 1993; *Casdagli* et al., 1992].

Deterministic chaotic time series are characterized by sensitivity to initial conditions and by a compact representation in state space (*i.e.* instantaneous states of the system fall within a finite volume in the n-dimensional space that is spanned by the n variables that describe the system) [e.g., *Nicolis*, 1995]. Modeled network patterns are expected to share these characteristics in that small shifts in the placement of a fracture can have significant and cumulative effects on the placement of later neighboring fractures. For example, the placement of the first, long fractures affects the position and orientation of subsequent fractures, even those not immediately neighboring, thereby contributing to the determination of the pattern over extended regions of the network. The constraints of existing fractures on the initiation and propagation of later fractures (through stress) imply that only a small subset of the range of all possible relative configurations of fractures will be realized. Therefore, by analogy, we employ an extension of time-series

forecasting techniques to spatial patterns [*Rubin*, 1992] to characterize and compare modeled and Espenberg networks.

Forecasting Method

The forecasting method acts on pixelated images of the networks, with the pixels corresponding to cells in the model or to cell-sized squares overlying the digitized Espenberg aerial photographs. Cells containing modeled or digitized fractures are assigned a value of 1 and cells without fractures are assigned a value of 0. Each image is then smoothed with a two-dimensional gaussian filter with standard deviation equal to 4 pixels (4 m), approximately the width of the ridges above ice wedges in Espenberg networks and about 20% of the spacing between ridges.

The image is divided into two parts (Figure 1.9); in the first part, an $m \times m$ pixel subregion, drawn at random, is used to predict the value of a pixel a distance of t pixels from the edge of the $m \times m$ region; in the second part, the N most similar $m \times m$ subregions are found by selecting those with the least sum-of-square differences from the subregion in the first part. A linear relationship between the $N \times m^2$ pixel values from these similar subregions and the value of the associated N pixels located t pixels from the regions is established by solving for m^2 regression coefficients using a least squares fit [*Rubin*, 1992]. A prediction is made by summing the values of the $m \times m$ pixel subregion drawn from the first part, weighted by the matrix of coefficients. Prediction error is calculated over many realizations of this procedure as a root mean square error of the predicted versus measured values of the displaced pixel, normalized against the standard

deviation of the pixel values in the image. The networks are characterized and compared using the dependence of prediction error on N and t. In analogy to time-series forecasting, N corresponds to the number of nearest neighbors in state space of the data set, t to the delay time and m^2 to the embedding dimension.

Images drawn from Espenberg and modeled networks are evaluated against the following synthetic images, which can be considered as null hypotheses for the mechanisms underlying network patterns: *i)* randomly placed straight lines (randomly placed lines); *ii)* modeled fractures that initiate at randomly selected positions and propagate according to reference model parameters, but do not interact via modeled stress relief (non-interacting modeled fractures); *iii)* network of squares (periodic network); *iv)* network of squares with lines displaced by a random distance, normally distributed with standard deviation equal to one-half the mean spacing between lines (periodic with uncorrelated noise); *v)* rectilinear network, with lines added in step-fashion across the network, with the placement of the next line displaced by a random distance as in pattern *iv* (periodic with correlated noise); and *vi)* an unsmoothed pattern of uncorrelated noise (white noise), to illustrate forecasting properties with the simplest case.

Results

For synthetic patterns with no or uncorrelated noise, prediction error is independent of distance (Figure 1.10a). For white noise, prediction error is 1 at all distances because the predicted value is approximately the mean of the image. For the synthetic pattern with straight lines displaced by correlated noise, the cumulative effect of randomness leads to

increasing prediction error with distance. Prediction error for random lines increases with distance but is below 1 over the range of forecast distances used because predictions that fall along the axis of long lines are successful over long forecast distances. Prediction error for non-interacting modeled fractures also increases with distance, but rises to 1 at short distances because of random meandering of fracture paths (Figure 1.10b).

Prediction error for Espenberg and modeled networks increases more slowly with distance (Figure 1.10b). Prediction error is low over forecasting distances equivalent to the characteristic spacing between fractures, but rises with distance. For modeled networks, this behavior can be interpreted as indicating stress-mediated interactions both between and along fractures. These interactions and the predictability of the pattern extend to distances greater than the characteristic spacing between fractures because of sequential placement of fractures. The corresponding trend in Espenberg network prediction error as a function of distance might be similarly explained.

Forecasts employing all possible configurations in state space maximize noise reduction but minimize sensitivity of the prediction to the particular configuration of the $m \times m$ region [*Rubin*, 1992]. For example, prediction errors for the white noise pattern and periodic network with uncorrelated noise decrease as more neighbors in state space are included in predictions (Figure 1.10c). At the other extreme, where only the most similar nearest neighbors in state space are employed in predictions, noise reduction is poorer but sensitivity of the prediction to the local pattern is improved. Prediction error

for the periodic network is zero for a small set of neighbors but rises as the number of nearest neighbors in state space used in predictions becomes greater than the number of near identical regions in the finite size image. Forecasting error is minimized for Espenberg and model networks when intermediate numbers of nearest neighbors in state space are employed in predictions (Figure 1.10d).

The results derived from spatial forecasting indicate the following properties for modeled and Espenberg ice-wedge networks: *i)* local predictability of the pattern, consistent with either deterministic, nonlinear dynamics or with correlated noise; and *ii)* best predictability at intermediate numbers of nearest neighbors in state space, compatible with dynamics that combine both nonlinear deterministic and stochastic mechanisms. These properties indicate that the local network pattern has a compact representation in state space, which is compatible with our simplifications for variables and the dynamical mechanisms by which networks are assembled.

Prediction of Espenberg Networks

Predictions of an Espenberg ice-wedge network, using either a modeled network or an Espenberg network, are better than predictions using straight lines and non-interacting fractures at both short and long distances, indicating that the predictability of the pattern arises from across-fracture, rather than along-fracture, correlations (Figure 1.11). Predictions based on a modeled network are comparable to those based on an Espenberg network, suggesting that modeled networks capture both the deterministic and stochastic properties of ice-wedge networks.

Sensitivity Of Modeled Networks To Parameters

The dependence of modeled networks on model parameters and strategies is characterized to test the robustness of the model to changes in parameters and to test the variation of networks properties with environmental conditions and material properties.

Initiation Strategy

The characteristic spacing between fractures in modeled networks is weakly sensitive to initiation strategy (Table 1.2). In eleven modeled networks for which the position and angle of initiation were chosen randomly, the characteristic spacing is similar to that for reference model networks, for which initiation position is selected at random but orientation is perpendicular to the axis of maximum principal stress. The spacing is detectably greater between fractures in optimized networks, for which fractures initiate at the position and orientation at which tensile stress is greatest. This difference results from the sequential addition of fractures to a network. Using the optimized strategy, fractures are initiated at positions as distant as possible from earlier fractures, minimizing the total number of fractures that form. Conversely, randomly placed fractures divide an unfractured region unequally, allowing for additional fractures in the larger of the two resulting regions, if residual tensile stress is above the minimum stress for initiation. For example, an optimized model starting with a square grid of fractures with 60 m spacing is subdivided by sequential fracturing into a network with D = 30 m spacing. From the same initial configuration, a modeled network in which fractures initiate at random positions and orientations evolves to D = 23 m.

Modeled networks in which initiation position and orientation are chosen at random are less orthogonal than reference or optimized networks (Table 1.2). This difference in orthogonality stems from the random orientation of initial fracture segments far from other fractures for the random strategy, contrasted with the tendency of initial fractures to be orthogonal for reference and optimized strategies. This is supported by the consistency of values of O for all strategies if separation is restricted to less than $\frac{1}{2}D$. Of the three strategies, random initiation networks are least similar to Espenberg networks (Table 1.1), owing to lesser degree of network organization.

Weighting of Along-Fracture Stresses

To evaluate the effect of limitation in the magnitude of stress intensity factor, K^I (Equation 3) owing to finite fracture depth, the contribution of stress along a fracture to K^I was weighted using a factor that linearly decreases from 1 at the tip to 0 10 m back along the fracture. G_{random} was set to 3 Jm^{-2} so the first fractures in a network with weighting follow paths similar to isolated fractures in frozen ground, but all other parameters remained as in the reference model. Spacing is insensitive to weighting (D = 22.2 ± 0.5 m for five networks with weighting). Weighted networks are more organized than reference model networks (O = 14 ± 2°, P = 30 ± 2°, R = 1.5 ± 0.3), probably because weighting constrains propagating tips to more closely reflect patterns of stress near the tip.

Initiation Threshold (Strength)

As strength decreases, the spacing between fractures in modeled networks decreases (Figure 1.12a). Spacing is most sensitive to strength for values of strength comparable to reference model values. For values of strength well above the reference model value, where strength approaches the applied thermal stress, increases in D are limited by propagation of fractures into regions where fractures could not initiate. For much lower strengths, fractures that would not have initiated at higher strengths cannot propagate far and so do not decrease spacing. This result suggests that propagation threshold might impose a limitation on minimum spacing under conditions where strength is low. Such a condition, different than reference model values, might arise in frozen ground at high temperatures (near 0°C) because the strength of frozen ground decreases and plasticity increases with rising temperature. However, initiation and propagation of fractures might also be limited by the relief of tensile stress by plastic strain prior to fracture under these conditions.

Applied Tensile Stress

Modeled networks respond to increases in applied tensile stress, τ_o, with decreases in fracture spacing (Figure 1.12b). For a two-fold increase in applied thermal stress from the reference model value, the characteristic spacing between fractures in modeled networks decreases from 22 to 18 m. D is not highly sensitive to τ_o over high values

because reduction of stress by a fracture segment is assumed proportional to the pre-fracture tensile stress (Equation 4).

Propagation Threshold

The characteristic spacing between fractures in modeled networks is generally insensitive to variations in the energetic propagation threshold, G_o, from the reference model value over the range of values 1 - 190 Jm^{-2} (Figure 1.12c), because over this range almost all fractures arrest at other fractures.

Randomness in Propagation Paths

Increases in G_{random} from the reference model value cause individual fractures to follow more irregular, sinuous paths. The characteristic spacing between fractures, as measured by D, is insensitive to the value of G_{random} (Figure 1.12d). However, the relative orientation between fractures in modeled networks is sensitive to the value of G_{random}, because organization of networks into fractures at parallel and orthogonal relative orientations is disrupted by irregular paths of earlier fractures and by paths of later fractures that diverge from an orientation perpendicular to the maximum principal stress because of modeled randomness.

Modeled Stress (η and C)

Parameters η and C encapsulate the effect of a modeled fracture segment on stress in the surrounding frozen ground. The spacing of fractures in modeled networks is sensitive to these parameters (Figure 1.12e-f). Although modeled networks are sensitive to η, the

value for frozen ground probably does not vary significantly from the reference model value, because frozen ground probably can be approximated as an elastic medium for the magnitude of stress and time-scales over which fractures interact via stress. For $\eta < 2$, all but the first fractures, which are long, arrest before intersection with an earlier fracture because of low strain energy release rate. Fractures organize to enclose polygonal regions for $\eta \geq 2$. The sensitivity of modeled networks to C and η, coupled with the observation that the spacing between ice wedges in frozen ground lies within a narrow range across diverse localities, suggests that both the rheology of frozen ground (related to η) and depth of fractures (proportional to C) are nearly uniform across sites where ice-wedge networks form.

Discussion

A rule-based model for sequential initiation and propagation of fractures in frozen ground produces fracture networks quantitatively similar to ice-wedge networks at Espenberg in Northwestern Alaska. The relative orientation between fracture segments is primarily orthogonal and parallel in modeled and Espenberg networks. The dependence of spatial forecasting error on distance and number of nearest neighbors in state space indicates similar degrees of deterministic and stochastic mechanisms in the development of modeled and Espenberg networks. Forecasts employing modeled networks can predict the configuration of an Espenberg ice-wedge network over distances greater than the characteristic spacing between fractures, with predictions as good or better than those made with other Espenberg networks. Spacing between fractures in modeled networks is

insensitive to initiation strategy, propagation threshold and random heterogeneities in propagation and is weakly sensitive to strength and applied thermal stress, a result consistent with nearly uniform characteristic spacing between ice wedges across a broad range of climates and substrates. The match between model and measurements and the lack of strong dependence on model parameters suggest that fracture networks in frozen ground are insensitive to the many details of fracture dynamics omitted from the model. Networks in frozen ground are a member of a larger class of fracture patterns driven by tension, including desiccation cracks, columnar jointing in basalt and subaqueous shrinkage cracks in clay [*Burst*, 1965]. The approach taken here may be applicable to these and other fracture patterns.

Modeled networks are primarily sensitive to variations in a model parameter that represents the functional dependence of stress at a point on the depth of nearby open fractures (C). Because the value of this parameter is chosen to reflect the measured depth of fractures in frozen ground and in ice wedges, this result suggests that consistent spacing in ice-wedge networks can be attributed to the consistent depth to which fractures propagate. Constraints on the downward opening of a fracture in frozen ground are imposed by the strain energy release rate and the energetic cost of propagation, G_O. The former is a function of the state of stress in a shallow layer at the ground surface, and is likely to vary widely as a function of air temperatures and snow depth. Because G_O for frozen ground probably is sensitive to temperature, the temperature and ice-content profile with depth might be the most important factor in determining the depth of downward propagation and hence the fracture spacing.

Insensitivity of the model to some parameters suggests the abstraction of fracture mechanisms probably is not minimal. The development of networks might be modeled by setting fracture tip behavior to reflect tensile and shear stress across the plane of the fracture at the tip only. Given the insensitivity of modeled networks to G_o over a wide range of values, all fractures could be allowed to propagate until arresting on existing fractures.

The marked orthogonality of Espenberg networks refutes speculations that the regions enclosed by ice wedges should be hexagonal. Given uniform, isotropic thermal stress and substrate properties, it has been argued that fractures arranged in hexagons maximize strain relief for a given area of fracture surface [*Black*, 1974]. Although ice-wedge networks frequently are described as hexagonal [e.g. *Leffingwell*, 1919; *Black*, 1952], the shape of enclosed regions has not been quantified. These qualitative characterizations probably arise from frequent intersections with relative orientation of approximately 120° between three fractures. Such equant intersections can develop in modeled networks by an alternative mechanism.

Modeled networks do not form hexagons because feedbacks between the developing fracture pattern and anisotropy of stress around open fractures lead to orthogonal intersections and crudely rectilinear enclosed regions. Moreover, the first fractures achieve lengths much longer than the characteristic spacing between fractures in well-developed networks. These mechanisms preclude hexagonal networks; nevertheless, equant three-way intersections do form, where a propagating fracture preferentially moves toward and arrests on the outer bend of a sinuous existing fracture (see box in

Figure 1.4d). Therefore, the frequency of equant intersections is increased where the initial fractures are more sinuous, as G_{random} is increased in the model or as material properties or stress become more heterogeneous in nature. However, further increase in G_{random} leads to disorganized modeled networks with large variations in fracture spacing and incompletely closed regions, rather than hexagonal networks, because pattern-scale articulation between equant intersections does not occur.

Differences in material heterogeneity or uniformity of prefracture stress, as parameterized in the model by G_{random}, might account for variations between Espenberg ice-wedge networks as measured by values of O and P. One Espenberg network is distinguished from all other Espenberg networks by greater orthogonality and parallelity between neighboring fracture segments, as shown by lower values for O and P (15° and 25° respectively). The range of values of O and P between this network and the least organized of the Espenberg networks (O = 26°, P = 31°) can be reproduced in reference model networks by varying G_{random} from 3 Jm^{-2} to 6 Jm^{-2} (the reference model value of G_{random} = 5 Jm^{-2}).

The measured variation of spacing (D) between Espenberg networks might be attributable to landscape position. The two Espenberg networks with largest characteristic fracture spacing (D = 28.3 and 27.8, respectively) are similar ($P > 0.200$) and are drawn from positions near margins of drained lakes, whereas the two networks with the smallest characteristic spacing (D = 22.6 and 22.9 m respectively), also similar, are located near the center of drained lakes. This difference might be attributable to deeper depth of snow in the lee of the relict shoreline bluff (approximately 3 m high) and hence lower thermal

stress for the lake-margin networks, but depth of snow here has not been measured. The method employed for quantifying the characteristic spacing might be useful for evaluating such differences for ice-wedge networks developed under different climates, micro-climates or substrates.

Whereas modeled networks generally exhibit those characteristics of Espenberg ice-wedge networks that are measured by spacing and relative orientation between fractures along randomly placed sample lines, some properties of Espenberg ice-wedge networks that are visually apparent are not simulated. One of these is four-way orthogonal intersections between fractures, which are not captured in distributions of spacing and relative orientation because measurements along sample lines are collected only between neighboring fractures. Four-way crossing intersections, which are common in Espenberg ice-wedge networks, are less common in modeled networks because fracture paths persist on the lattice and propagating fractures cannot cross open paths. Such intersections do form in modeled networks through addition of two fractures to a configuration of earlier fractures that is roughly mirror-symmetric across the plane of the fracture that arrests the two later fractures. Such configurations constrain later, opposing fractures to arrest at a similar position along the earlier fracture. However, intersections formed by this mechanism are less frequent than four-way intersections in Espenberg networks.

Documentation of the first fractures and early development of ice wedges in newly frozen ground in a drained lake bed [*Mackay*, 1986] suggest that some ice-wedge networks initially develop under conditions different from those under which ice wedges grow through repeated annual fracturing. In the setting of a recently drained lake, where

snow cover is shallow because there is little or no vegetation to trap blowing snow [*Mackay*, 1986], thermal tensile stress might be much greater because absolute temperatures are lower and the rate at which ground temperatures falls is more rapid. In addition, fracture depth would be limited to the shallow depth of the frozen brittle layer. Representing these conditions in the reference model by decreasing C to 1 m^2 and increasing τ_O to 4 x 10^6 MNm^{-2}, the resulting modeled network has a characteristic spacing D = 9 m, a value similar to measured spacings of approximately 10 m between fractures arranged in crude polygons in the newly frozen basin of a drained lake [*Mackay*, 1986].

Possible divergence of an ice-wedge pattern from a network formed by the first fractures, as might occur for the scenario of the drained lake, cannot be addressed with the current version of the model. In the sequential representation of fracture emplacement, networks self-organize through interactions between tensile stress and the developing fracture pattern under the assumption that fractures persist and are open during subsequent development of the network. However, the selective recurrence of fractures along ice-wedge paths in subsequent winters, under naturally varying climate, might lead to an ice-wedge pattern different from the pattern of initial fractures, because fracture paths are influenced by both fractures and by a tendency to propagate along the paths of ice wedges. Divergence between the initial fracture pattern in permafrost and the ice-wedge pattern might underlie some of the properties of ice-wedge networks that are not well modeled, such as four-way orthogonal intersections. Moreover, a developing ice-

wedge pattern, by deforming the surface and thereby inducing changes in vegetation and snow accumulation, probably is coupled to the pattern of annual fractures in ice wedges. Modeling the dynamics of ice-wedge networks from the pattern of first fractures to wide ice wedges, already in progress, will permit more accurate treatment of ice-wedge networks and assessment of the effects of climatic changes on network patterns.

Acknowledgments

We are grateful to L. Clarke, J. Foat, M. Kessler and M. Okihiro at UCSD for discussions on modeling and analysis of fracture patterns. D.M. Hopkins and D.H. Mann at UAF gave advice on the geomorphology of the Espenberg region. D.M. Hopkins and D. Kane (UAF) provided helpful comments on the manuscript. Supported by the National Science Foundation, Arctic Natural Sciences Program (OPP-9530860), and the National Park Service, Bering Land Bridge National Preserve, Beringian Shared Heritage Program (Espenberg/Thaw-lakes component of the Beringian Shared Heritage Project to D.M. Hopkins and L.J. Plug).

References

Abarbanel, H. D. I., R. Brown, J. J. Sidorowich, and L. S. Tsimring, The analysis of observed chaotic data in physical systems, *Rev. of Mod. Phys., 65*, 1331-1392, 1993.

Al-Moussawi, H. M., Thermal contraction and crack formation in frozen soil, Ph.D Thesis, Michigan State Univ., Lansing, 1988.

Allard, M., and J. N. Kasper, Temperature conditions for ice-wedge cracking: field measurements from Salluit, northern Quebec, in *Permafrost Seventh International Conference Proceedings*, pp. 5-12, Univ. of Laval Press, Quebec, 1998.

Andersland, O. B. and B. Ladanyi, *Introduction to Frozen Ground Engineering*, 352 pp. Chapman and Hall, New York, 1994.

Birch, F., The effect of Pleistocene thermal gradients upon geothermal gradients, *American Journal of Science, 238*, 529-558, 1948.

Black, R. F., Polygonal patterns and ground conditions from aerial photographs, *Photog. Eng., 18*, 123-134, 1952.

Black, R. F., Ice-wedge polygons of northern Alaska, in *Glacial Geomorphology*, edited by D.R. Coates, pp. 247-275, State Univ. of New York, Binghampton, 1974.

Bragg, R. A., and O. B. Andersland, Strain rate, temperature, and sample size effects on compression and tensile properties of frozen sand, *Engineering Geology, 18*, 35-46, 1981.

Bueckner, H. F., A novel principle for computation of stress intensity factors, *Zeitschrift für Angewandte Mathematik und Mechanik, 50*, 529-540, 1970.

Burn, C. R., Implications for palaeoenvironmental reconstruction of recent ice-wedge development at Mayo, Yukon Territory, *Permafrost and Periglacial Processes, 1*, 3-14, 1990.

Burst, J. F. Subaqueously formed shrinkage cracks in clay, *Journal of Sedimentary Petrology, 35*, 348-353, 1965.

Casdagli, M., D. Des Jardins, S. Eubank, J. D. Farmer, J. Gibson, N. Hunter, and J. Theiler, Nonlinear modeling of chaotic time series: Theory and applications, in *Applied Chaos*, edited by J. Kim and J. Stringer, pp. 335-380, John Wiley, New York, 1992.

Cotterell, B, and J. R. Rice, Slightly curved or kinked cracks, *Int. J. of Fracture, 16*,155-169, 1980.

Fasano, G., and A. Franceschini, A multi-dimensional version of the Kolmorogov-Smirnov test, *Mon. Not. R. Astron. Soc., 225*, 155-170, 1987.

French, H. M., *The Periglacial Environment*, 341 pp., Addison Wesley, Harlow, 1996.

Gold, L.W., Engineering properties of fresh-water ice, *Journal of Glaciology, 19*, 197-211, 1977.

Goodman, D. J., and D. Tabor, Fracture toughness of ice: A preliminary account of some new experiments, *Journal of Glaciology, 21*, 651-660, 1978.

Goughnour, R. R. and O. B. Andersland, Mechanical properties of a sand-ice system, *American Society of Civil Engineers, Soil Mechanics and Foundations Division Journal, 94*, 923-950, 1968.

Haken, H., *Synergetics*, Springer-Verlag, Berlin, 1983.

Hopkins, D. M., Aspects of the paleogeography of Beringia during the Late Pleistocene, in *Paleoecology of Beringia*, edited by D. M. Hopkins, J. V. Matthews, C. E. Schweger and S. B. Young, pp. 3-28, Academic Press, New York, 1982.

Ingraffea, A. R., Theory of crack initiation and propagation in rock, in *Fracture Mechanics of Rock*, edited by B. K. Atkinson, pp. 71-110, Academic Press, San Diego, Calif., 1987.

Irwin, G. R., Fracture, in *Handbuch der Physik, 6*, Spring-Verlag, Berlin, 551, 1958.

Johnson, W. H., Ice-wedge casts and relict patterned ground in central Illinois and their environmental significance, *Quaternary Research, 33*, 51-72, 1990.

Knight, G. R., Ice-wedge cracking and related effects on buried pipelines, in *Symposium on Cold Regions Engineering Proceedings*, edited by J. L. Burdick, pp. 384-95, Am. Soc. Civil Eng., and Univ. Alaska, Fairbanks, 1971.

Lachenbruch, A. H., Depth and Spacing of Tension Cracks, *J. Geophys. Res.*, *66*, 4273-4292, 1961.

Lachenbruch, A. H., Mechanics of thermal contraction cracks and ice-wedge polygons in permafrost, *Geological Society of America Special Paper, 70*, 69 pp., 1962.

Lachenbruch, A. H., Contraction theory of ice-wedge polygons: A qualitative approach, *Proceedings: Permafrost International Conference*, pp. 63-70, NAS-NRC, Publication 1287, 1966.

Ladanyi, B., G.H. Johnston, N.R. Morgenstern and E. Penner, Engineering characteristics of frozen and thawing soils, in *Permafrost: Engineering Design and Construction*, pp. 73-147, edited by G. H. Johnston, Wiley, New York, 1981.

Lawn, B. R., *Fracture of Brittle Solids*, Cambridge Univ. Press, Cambridge, 1993.

Leffingwell, E. K., Ground-ice wedges, the dominant form of ground-ice on the north coast of Alaska, *J. Geol., 23,* 635-654, 1915.

Leffingwell, E. K., The Canning River Region, Northern Alaska, *United States Geological Survey Professional Paper, 109,* 251p, 1919.

Mackay, J. R. Ice-wedge cracks, Garry Island, Northwest Territories, *Can. J. Earth Sci., 11,* 1366-1383, 1974.

Mackay, J. R., The direction of ice-wedge cracking in permafrost: downward or upward? *Can. J. Earth Sci., 21,* 516-524, 1983.

Mackay, J. R., The first 7 years (1978-1985) of ice wedge growth, Illisarvik experimental drained lake site, western Arctic coast, *Can. J. Earth Sci. 23,* 1782-1795, 1986.

Mackay, J. R., Sound and speed of ice-wedge cracking, *Can. J. Earth Sci. 30,* 509-518, 1993a.

Mackay, J. R., Air temperature, snow cover, creep of frozen ground, and the time of ice-wedge cracking, western Arctic coast, *Can. J. Earth Sci. 30,* 1720-1729, 1993b.

Mackay, J. R., Ice wedges on hillslopes and landform evolution in the late Quaternary, western Arctic coast, Canada, *Can. J. Earth Sci. 32,* 1093-1105, 1995.

Mellon, M. T., Small-scale polygonal features on Mars: Seasonal thermal contraction cracks in permafrost, *J. Geophys. Res., 102,* 25,617-25,628. 1997.

National Park Service, Near-infrared aerial photographs of coastal regions of the Bering Land-Bridge National Preserve, Anchorage, Alaska, 1986.

Nicolis, G., *Introduction to Nonlinear Science*, 254 pp., Cambridge University Press, Cambridge, 1995.

Nicolis, G., and I. Prigogine, *Self-organization in Nonequilibrium Systems*, 491 pp., Wiley, New York, 1977.

NOAA (National Oceanographic and Atmospheric Administration), Unedited Local Daily Climatological Data for Kotzbue Ralph Wein Memorial Airport, Alaska, 1999.

Olson, J. E., Joint pattern development: Effects of subcritical crack growth and mechanical crack interaction, *J. Geophys. Res.*, *98*, 12,251-12,265, 1993.

Peacock, J. A., Two-dimensional goodness of fit testing in astronomy, *Mon. Not. R. Astron. Soc.*, *202*, 615-627, 1983.

Péwé, T. L., Ice wedges in Alaska - classfication, distribution and climatic significance, in *International Permafrost Conference Proceedings*, pp. 76-81, National Academy of Science and National Research Council, Publication 1287, 1966.

Plug, L. J. and B. T. Werner, A numerical model for the organization of ice-wedge networks, in *Permafrost Seventh International Conference Proceedings*, pp. 897-902, Univ. of Laval Press, Quebec, 1998.

Pollard, D. D., and P. Segall, Theoretical displacments and stresses near fractures in rock: With applications to faults, joints, veins, dikes and solution surfaces, in *Fracture Mechanics of Rock*, edited by B.K. Atkinson, pp. 277-349, Academic Press, San Diego, 1987.

Renshaw, C. E., and D. D. Pollard, Numerical simulation of fracture set formation: A fracture mechanics model consistent with experimental observations, *J. Geophys. Res.*, *99*, 9359-9372, 1994.

Rice, J. R., Weight function theory for three-dimensional elastic crack analysis, pp. 29-57, ASTM STP, 1020, American Society for Testing and Materials, Philadelphia, 1972.

Rubin, D. M., Use of forecasting signatures to help distinguish periodicity, randomness, and chaos in ripples and other spatial patterns, *Chaos*, *2*, 525-535, 1992.

Sayles, F. H., Stress-strain behavior of frozen soil in tension, in *Proc. Seminar on Gas Pipelines, Oil Pipelines and Civil Engineering in Arctic Climates, (Caen, France)*, pp. 61-72, Carleton Univ. Press, Ottawa, 1991.

Schaaf, J., *Ublasaun*, National Park Service, Shared Beringian Heritage Program, 143p. 1998.

Smallwood, R. H., Two dimensional Kolmorogov-Smirnov test for binned data, *Phys. Med. Biol.*, *41*, 125-135, 1996.

Tsytovich, N. A., *The mechanics of frozen ground*, 426 pp., McGraw-Hill, New York, 1975.

Werner, B. T., Eolian dunes; computer simulations and attractor interpretation, *Geology*, *23*, 1107-1110, 1995.

Werner, B. T., Complexity in natural landform patterns, *Science*, *284*, 102-104, 1999.

Williams, P. J., and M. W. Smith, *The Frozen Earth: Fundamentals of Geocryology*, 306 pp., Cambridge Univ. Press, Cambridge, 1991.

WRCC (Western Regional Climate Center), Kotzebue WSO Airport, Alaska Climate Summary, 9/1/1949 to 12/31/1998, http://www.wrcc.dri.edu, 1999.

Yershov, E. D., *General Geocryology*, 580 pp., Cambridge Univ. Press, Cambridge, 1998.

Yoffe, E. H., The moving Griffith crack, *Philos. Mag., 42*, 739-750, 1951.

Zhu, Y., and D. L. Carbee, *Tensile strength of frozen silt*, U.S. Army Cold Reg. Res. Eng. Lab., Report 87-15, 1987.

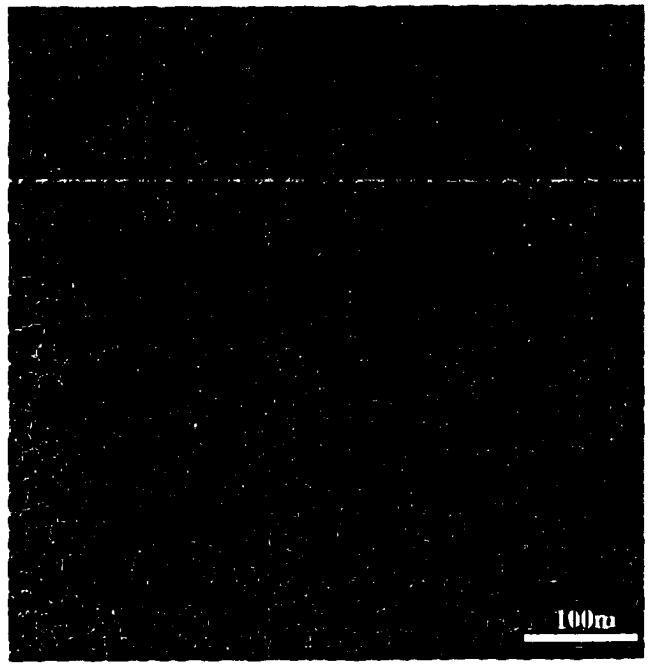

FIGURE 1.1. Near-infrared aerial photograph of an ice-wedge network near Espenberg, Alaska. Ridges (0.25-1 m in height) over ice wedges appear light because they are dry and covered by herbaceous vegetation. Low areas between ridges appear dark because of wet ground or standing water. Photograph from National Park Service [1986].

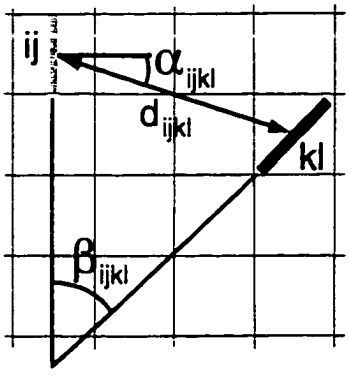

FIGURE 1.2. Measurements of distance (d_{ijkl}) and relative orientation (β_{ijkl} and α_{ijkl}) between fracture segments employed for determination of stress relief from open fractures, where *ij* is the cell at which stress is calculated and *kl* is a cell containing a fracture segment.

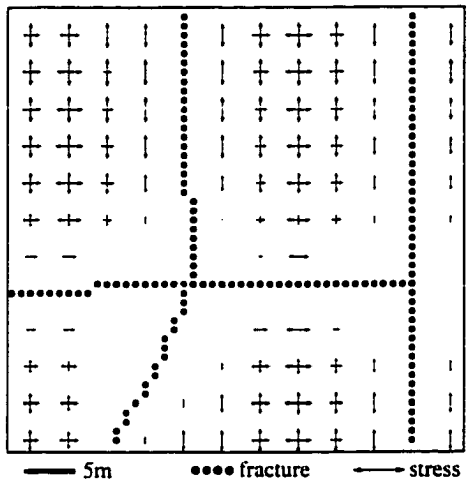

FIGURE 1.3. Modeled tensile stress field surrounding fracture segments. Length of arrows represent intensity of tensile stress projected across the two axes. Fractures reduce stress locally (stress reduction decreases as an inverse power law in distance from a fracture segment) and impose anisotropy (stress is relieved only in the direction perpendicular to the fracture). Region shown is an inset of a larger network; stress near boundaries are influenced by out-of-view fractures.

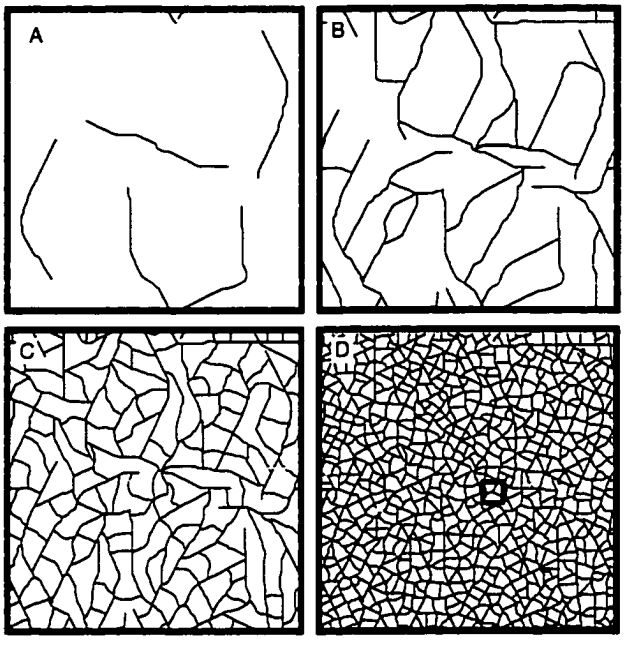

FIGURE 1.4. Development of a modeled fracture network using reference model parameters on an 800 × 800 lattice of 1 m^2 cells. Initial fractures are long, with irregular bends from heterogeneity as modeled with a Boltzmann function. Fractures first enclose regions of the simulation space with dimensions several times the spacing between parallel fractures in fully developed networks. These regions are subsequently subdivided by short, often straight fractures for which orientation is determined by patterns of stress imposed by the initial fractures. Most modeled fractures arrest at orthogonal intersections with existing fractures. Some arrest at the outside of a curve in an earlier fracture, forming roughly equant intersections (e.g., indicated by box). In steady-state networks (those where stress is everywhere below the minimum initiation stress), fractures enclose regions approximately 22 m across, similar to measurements from many ice-wedge networks.

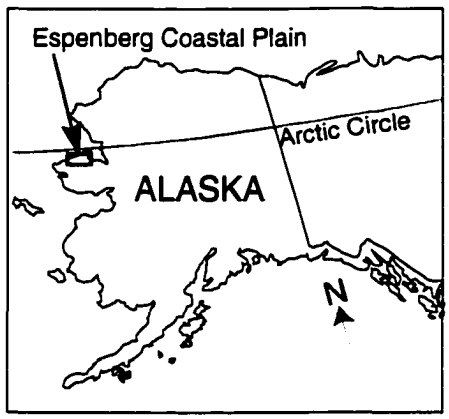

FIGURE 1.5. Location of the Espenberg region, from where natural ice-wedge networks are drawn.

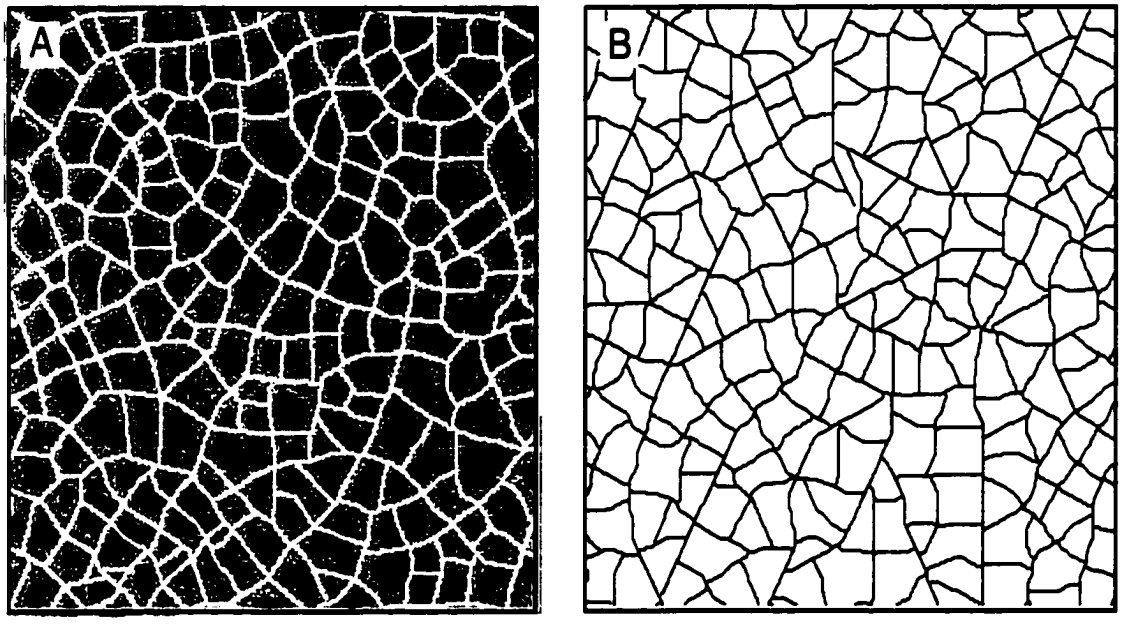

FIGURE 1.6. Examples of networks used in quantitative comparisons between natural and modeled networks; (A) Ice-wedge network from Espenberg. Espenberg networks are manually digitized from aerial photographs, using the assumption that the center line of an ice wedge lies below the center line of a rampart visible at the surface; (B) Reference model network.

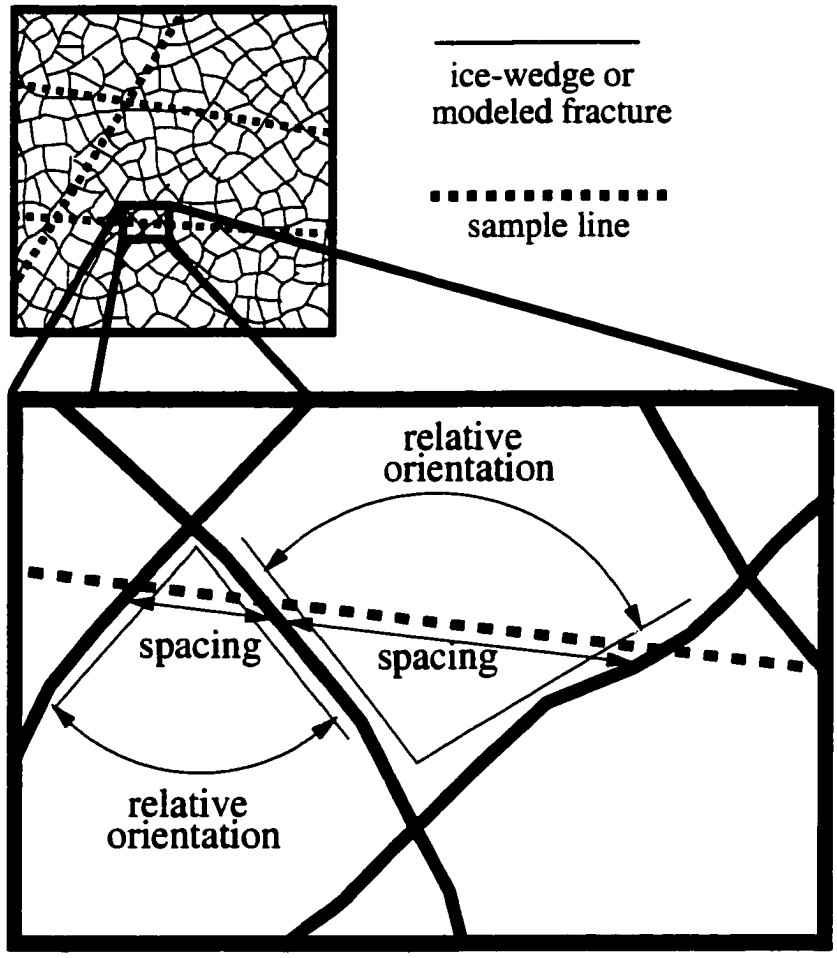

FIGURE 1.7. Spacing and relative orientation between fracture segments are measured along sample lines that dissect a network at randomly chosen orientations and positions.

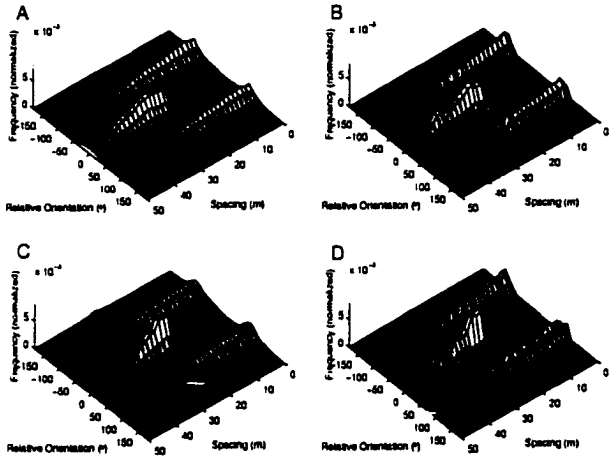

FIGURE 1.8. Two-dimensional distributions of relative angle and spacing between fractures for A) mean of 10 Espenberg ice-wedge networks; B) mean of 20 reference model networks; C) one Espenberg ice-wedge network; and D) one reference model network. Frequency is normalized against total number of observations. Parallel ice wedges are spaced approximately 25 m apart and those close to one another along the sample line are orthogonal. Modeled networks show similar distributions. A second spacing peak at parallel orientations (B, 37 m) occurs in modeled networks because some fractures are placed in a position too near to an earlier fracture for a later fracture to be added at a shorter distance.

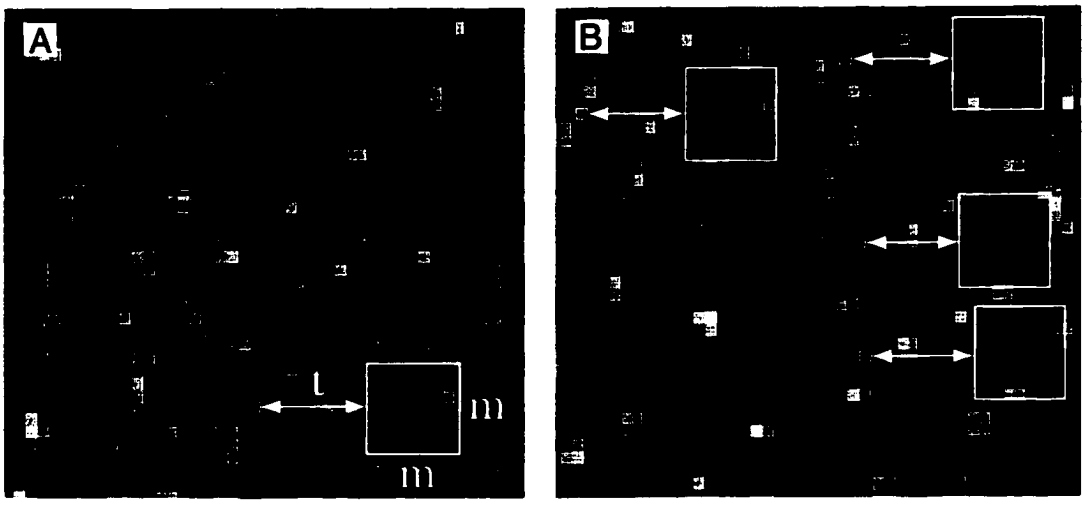

FIGURE 1.9. Pixelated images used in spatial forecasting are drawn from an Espenberg network, modeled networks and five synthetic patterns described in text. Two images, A and B, are chosen from the same network (portions of each shown). *A)* A subregion of $m \times m$ pixels is chosen at random. The value of an associated pixel displaced t pixels from the edge of the subregion is compared to predictions based on image B. *B)* The N most similar subregions to that in A are found (4 are shown). A relationship between the values of the m^2 pixels in these subregions and their associated displaced pixels is found using a least squares fit. A prediction is made by applying this relationship to the values of pixels in the subregion from image A. The resulting predicted pixel value is compared to the actual value of the displaced pixel. An RMS error for predictions is found over many realizations of this procedure.

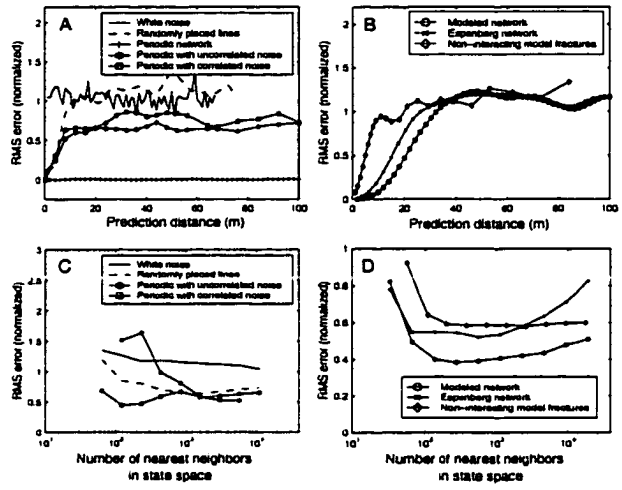

FIGURE 1.10. RMS error of predictions as a function of forecasting distance (t) and number of nearest neighbors in state space (N) used in forming a prediction. *A)* Prediction error vs. distance for five synthetic images described in text; *B)* Prediction error vs. distance for reference model network, Espenberg ice-wedge network and network of non-interacting modeled fractures; *C)* Prediction error vs. number of nearest neighbors in state space (N) for synthetic networks. The periodic network (shown in *A* but not shown here) has zero prediction error. *D)* Prediction error vs. number of nearest neighbors in state space (N) for reference model network, Espenberg ice-wedge network and network of non-interacting modeled fractures. All distance forecasts (*A* and *B*) use values of N that give the best predictions for each image. Distance (t) is measured from the edge of the $m \times m$ region toward the predicted pixel, minus the smoothing distance (see text). t = 10 m for all predictions in *C* and *D*. All predictions are based on 7 × 7 pixel regions with pixel size 2 × 2 m. Errors are normalized by the standard deviation of

pixel values in the image and are calculated over 100 predictions at each value of t and N. For synthetic patterns, prediction error is constant with distance because patterns are deterministic at all length scales and prediction error decreases with number of neighbors in state space because noise reduction is maximized. For Espenberg and modeled networks, prediction error is small at short distances but rises to 1 because of local, stress-mediated interactions between sequentially placed fractures; best predictions are formed at intermediate numbers of nearest neighbors, indicating both deterministic and stochastic mechanisms underlie the development of network patterns.

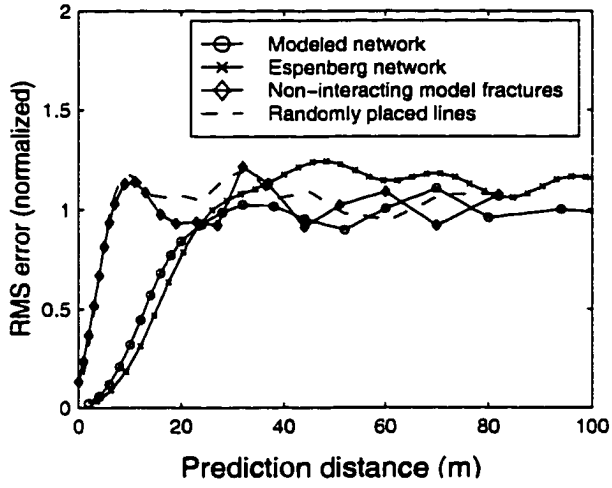

FIGURE 1.11. RMS error of predictions vs. distance for an Espenberg network, for forecasts based on an Espenberg network, reference model network and non-interacting modeled fractures. Modeled networks predict Espenberg network patterns approximately as well as other Espenberg networks.

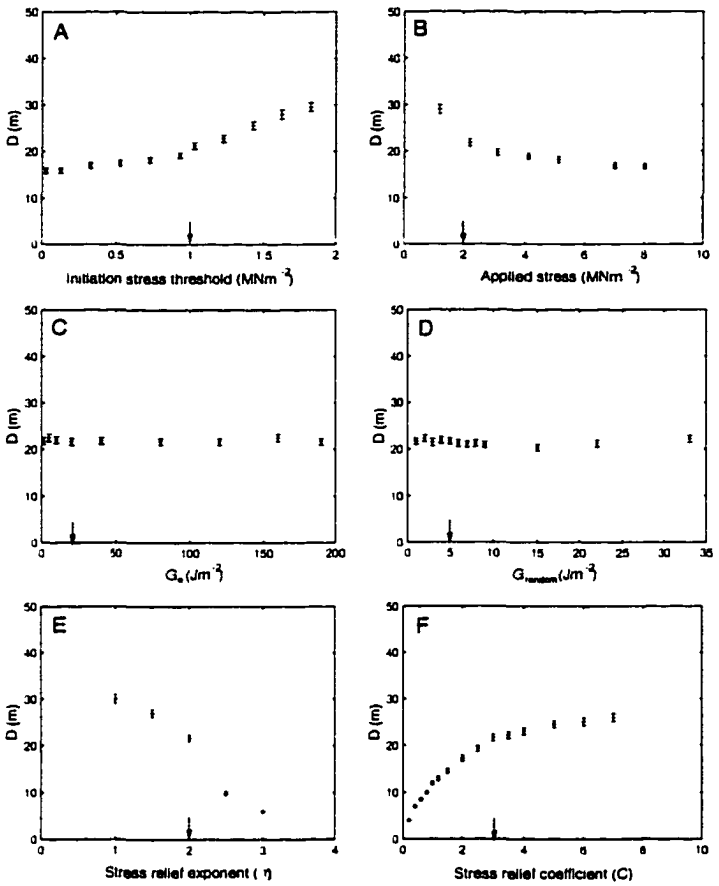

FIGURE 1.12. Sensitivity of characteristic spacing, D, in modeled networks to A) minimum tensile stress required to initiate a fracture; B) applied tensile stress, τ_0; C) energetic propagation threshold, G_O; D) amplitude of random variations in energetic propagation threshold, G_{random}; E) stress relief exponent, η; F) stress relief coefficient, C. Arrows denote reference model values. Error bars indicate the standard deviation of the sample over 5 realizations. Spacing between fractures in modeled networks is principally sensitive to stress relief coefficient C.

Probability level, *P*, for Kolmogorov-Smirnov comparisons between joint distributions of relative orientation and spacing.

	P	*Pairs (P > 0.20)*
Espenberg - Espenberg	0.10 ± 0.06	7/45
Reference - Reference	0.18 ± 0.04	41/190
Random Initiation - Random Initiation	0.15 ± 0.05	6/45
Stress Initiation - Stress Initiation	0.18 ± 0.04	18/45
Reference model - Espenberg (individual)	0.13 ± 0.05	12/200
Reference model - Espenberg (combined)	0.15	0/1
Random Initiation - Espenberg	0.07 ± 0.04	0/100
Stress Initiation - Espenberg	0.14 ± 0.06	8/100
Squares - Espenberg	<0.001	0/10
Hexagons - Espenberg	<0.001	0/10

TABLE 1.1. Probability level, *P*, for Kolmogorov-Smirnov comparisons between joint distributions of relative orientation and spacing for Espenberg, modeled and other network patterns. Tests use 32 × 32 bins with bin size 11.25° by 1.56 m. Uncertainties are reported as standard deviation of the sample.

Summary statistics for spacing and relative orientation between fractures.

	Espenberg (n=10)	Reference (n=20)	Random Initiation (n=10)	Stress Initiation (n=10)	Squares	Random Lines
Characteristic spacing (D)	25 ± 2 m	22.6 ± 0.4 m	22.5 ± 0.4 m	23.7 ± 0.3 m	N/A	N/A
Orthogonality (O)	19 ± 3°	18 ± 2°	23 ± 6°	18 ± 2°	0	55°
Parallelity (P)	30 ± 6°	33 ± 3°	38 ± 11°	31 ± 2°	0	55°
R	1.5 ± 0.4	1.4 ± 0.3	1.8 ± 0.8	1.4 ± 0.3	1.5	1

TABLE 1.2. Summary statistics for spacing and relative orientation between fractures in Espenberg, modeled and other network patterns. Uncertainties are reported as standard deviation of the sample.

Development of Ice-Wedge Networks by Annual Fracturing[1]

Abstract

Wedges of ice in perennially frozen ground self-organize into connected networks over thousands of years through interactions between tensile stress from ground cooling, fractures in frozen ground that fill with ice and the developing network of ice wedges. In a model encapsulating these interactions, networks similar to natural ice-wedge networks develop in which the annual pattern of fractures diverges from the ice-wedge pattern, with only 1/3 - 3/4 of wedges fracturing in a single year. Short-lived sequences of high stress from cooling can permanently alter the spacing between and fracture frequency of ice wedges, suggesting that the extent and characteristics of existing and relic ice-wedge networks reflect extreme, not mean, climate conditions.

Text

Patterns of interconnected subsurface wedges of ice, expressed at the ground surface by networks of ridges or troughs spaced 10 - 20 m apart (Fig. 2.1), are a common feature of Arctic and sub-Arctic landscapes (*1*). These ice-wedge networks originate with fractures opened asynchronously in perennially frozen ground by tensile stress owing to falling temperatures in winter (*2-4*). Open fractures partially fill with ice from blowing

[1]L.J. Plug and B.T. Werner. Prepared for submission to *Science*.

snow or frozen melt water and then close when the ground warms (*3,4*). The paths of fractures are affected by patterns of stress from already open nearby fractures (*2, 5*), by heterogeneity in frozen ground and snow depth (*2-4*) and by the paths of fractures in previous winters, which are more susceptible to subsequent fracture because ice is weaker than frozen ground (*3, 4, 6-10*). Over tens to thousands of years, V-shaped wedges of ice consistently 3 - 5 m deep and up to several meters wide develop along recurring fracture paths (*6, 10*). Upward deformation at the ground surface ranging from decimeters to 1 meter reveals the position of growing ice wedges below (*10-12*).

The width of existing ice wedges (*10, 13*) and the geographical distribution of traces of now-melted ice wedge networks (*13-16*) have been used to infer characteristics of past cold climates. Evidence for growth of ice wedges in deformed soils and measured changes in the frequency of fracturing for existing ice wedges have been interpreted as reflecting changes in climate at high latitudes over the past 10 - 2000 years (*17*). These inferences regarding climate have been made with the assumption that the response of an ice-wedge network to variations in winter climate is monotonic and intuitive in that it is equivalent to the response of a single ice wedge within a field of ice wedges characterized only by their bulk properties. However, the nonlinearity of fracture initiation and propagation, the influence of open fractures on subsequent fracturing during a single winter and the long-term memory of fracture patterns from previous winters stored in ice wedges all constitute building blocks of a system that could exhibit complex dynamical behavior diverging from the behavior of a single ice wedge. To investigate the complexity of ice-wedge network dynamics and their reaction to climate change, we

present a numerical model for fracture, ice wedges and ice-wedge network development and describe its behavior over a range of climate scenarios.

Reflecting the essentially two-dimensional nature of ice-wedge networks (*2*, *5-7*), fractures and ice wedges are modeled on a two-dimensional array of cells representing the top several meters of frozen ground and ice: here, the array consists of 200 × 200 1 m^2 cells. Each cell contains either frozen ground, with strength 1.5 MPa, or ice, with strength 0.5 MPa (*18*), and can contain a segment of an open fracture, the orientation of which is continuous and smoothly varies with that of fracture segments in adjoining cells along the same fracture. Cells with ice are assigned an ice-wedge width that increases each time the cell fractures. A modeled year consists of a single episode of fracture in which thermally-induced tensile stress increases uniformly over all cells from 0 MPa by increments of 0.04 MPa to a specified maximum that varies with the climate scenario. Fracture segments reduce this tensile stress nearby in a manner that varies with the inverse square of distance, is maximized along a line perpendicular to the segment and approximates stress reduction near an infinitely long, 4 m deep fracture in an elastic half space (*19*). Stress reduction by fracture segments is summed linearly to determine the tensile stress in each cell.

As tensile stress increases, fractures in the model sequentially initiate, propagate in two opposing directions from their cell of origin, and arrest. We have chosen for the model a representation of these processes that encapsulates the mechanics of linear-elastic fracture, with fast-time-scale processes parameterized or ignored. The cell in

which a modeled fracture initiates and its orientation are chosen to maximize the ratio of tensile stress to strength over the entire array. At each increment of imposed tensile stress, fractures are initiated until this ratio is below one for all cells that remain unfractured. The direction of propagation of a fracture is determined by a tendency to maximize the elastic energy released by opening a fracture minus the energy required to create new fracture surfaces (*20*). The effect of heterogeneity in the properties of frozen ground and in tensile stress on propagation is parameterized by assigning propagation direction from a Boltzmann distribution (*21*). Modeled fractures arrest either when encountering a cell with an open fracture segment or when insufficient elastic energy is released as the fracture opens to cleave the material in the cell ahead of the fracture tip. Given that ice is weaker than frozen ground and requires less energy to open fractures (*22*), fractures tend to initiate in unfractured ice-filled cells and to propagate along paths of ice-filled cells.

At the end of a fracturing episode, the width of ice wedges is increased in cells with open fractures by a positive amount drawn from a normal distribution with both mean and standard deviation 0.0015 m (*6, 10, 23*) and all fractures are then closed. The effect of a growing ice wedge on the ground surface is calculated by raising the surface over the wedge by a volume equal to the volume of ice added, assuming that the depth of the wedge is 4 m (*24*). The elevation increment has a gaussian shape centered on the axis of the ice wedge, with standard deviation equal to the wedge width (*14*). Downslope soil creep from wind, rainsplash, freezing and thawing, and plant and animal activity is

modeled by applying linear diffusion to the resulting morphology, with diffusion constant 10^{-2} m^2 y^{-1} (*25*).

Many details relating to fracture propagation, the tensile stress field and frozen ground deformation are simplified or omitted from the model. As in other systems dominated by strongly nonlinear, dissipative processes, simplifications are warranted for processes with intrinsic time scales that are shorter and well-separated from the pattern of interest, the ice wedges, because the fast processes are controlled by, or slaved to, the slow evolution of the ice-wedge network (*26*). This assumption can be tested by comparing the model to natural ice-wedge networks.

The networks of fractures and ice wedges that assemble in the model (Fig. 2.2) are both qualitatively and quantitatively similar to networks in frozen ground (Fig. 2.1). The ice wedge networks are visually similar, with ice wedges ranging from long and sinuous to short and straight. Many ice wedges terminate at other wedges, but some paths cross, forming four-way junctions. The spacing between modeled ice wedges is approximately 17 m, comparable to the approximately 20 m spacing between ice wedges at Espenberg, Alaska (*5*). The width of ice wedges in the model after 1500 y, about 2 m, is close to widths of ice wedges of comparable age in northern Alaska (*10*). Most intersections between modeled fractures are orthogonal, as are intersections between fractures in frozen ground (*3*). The difference between joint distributions of relative orientation and spacing for ice wedges in the model and at Espenberg, NW Alaska, are comparable to differences between Espenberg networks, as evaluated with a two-dimensional Kolmogorov-Smirnov test (*5*). One prominent difference between modeled and measured

networks is the presence of high peaks over some intersections between ice wedges in the model, which are not apparent in natural ice-wedge networks. This might indicate that ice wedge growth increments near intersections are reduced, possibly because of reduced tensile stress, an effect not included in the model.

In the reference model, with a maximum tensile stress that has the same value of 3 MPa each year (*27*), the pattern of ice wedges diverges from the initial fracture pattern (Fig. 2.2A), as illustrated by a decrease in spacing between ice wedges from 22 m in the first year to 17.5 m after 1000 years (Fig. 2.3A). This divergence arises as different permutations in the ordering of fracturing permit the introduction of new fracture paths (Fig. 2.2A). New ice wedges can form when changes in fracture sequence cause the ratio of tensile stress to strength at some locations in frozen ground to exceed one before neighboring ice wedges fracture and reduce the regional tensile stress below the strength of frozen ground. Changes in fracture sequence also can lead to a new wedge when a fracture that previously had terminated on an open fracture continues beyond it in a subsequent year because that wedge had not yet fractured, thereby converting orthogonal three-way intersections into crossing four-way intersections, which are common in natural ice wedge networks (Fig. 2.1). The modeled ice-wedge network attains a steady state after approximately 1000 years, characterized by a spacing of 20.0 m between fractures in any one year and 17.7 m between ice wedges. Only 75% of ice-wedges fracture per year at this steady state. The spacing between fractures and the percentage of ice wedges that fracture are consistent between different modeled winters, varying by only 0.2 m and 1% respectively. Ice wedges that are long tend to fracture more frequently

because they contain more potential sites for fracture initiation, some of which might not experience reduced tensile stress because of neighboring open fractures, and because once a fracture has initiated in a wedge, it generally propagates along its entire length. Open fractures in these long wedges reduce tensile stress in adjoining short wedges, lowering their fracture frequency and rate of growth. The width of ice wedges reaches 2.2 ± 1.0 m after 1500 y, the high standard deviation reflecting the variation in frequency with which ice wedges fracture and the addition of new wedges during the first 1000 years.

Maximum tensile stress in frozen ground during a winter is a complicated function of temperature, rate of cooling and snow depth, each of which can vary significantly from year to year (*2, 4, 8*). To address whether the properties of ice wedge networks and widths of wedges reflect mean conditions or extreme winters, the development of two networks was modeled using normally distributed maximum tensile stress with mean 3 MPa and standard deviations 1 MPa (narrow stress) and 2 MPa (broad stress) (*28*). The narrow-stress network reaches steady state after approximately 1100 y, with spacing between ice wedges of 15.8 m (Fig. 2.3B), whereas the broad-stress network does not reach steady state until about 1700 y, with ice wedges separated by only 8.5 m (Fig. 2.2B, Fig. 2.3C). In contrast, the spacing between fractures in one year, 18.5 ± 2.2 m and 17.5 ± 3.1 m for low- and broad-stress networks respectively, remains close to the spacing in the reference model. This relative insensitivity of fracture spacing to imposed tensile stress can be attributed to the scaling of stress relief by open fractures with imposed stress (*19, 5*). Correspondingly, the fraction of ice wedges that fracture in a given year is reduced

from and more variable than the reference model: 69 ± 14% for the narrow-stress network and 33 ± 18% for the broad-stress network. These results indicate the sensitivity of the development of ice wedge networks to fluctuations in conditions contributing to maximum tensile stress. This sensitivity is further underlined by a numerical experiment duplicating the reference model, but with a temporary increase in maximum tensile stress after 200 years to 5 MPa lasting just one decade. A permanent decrease in ice wedge spacing from 17.7 to 15.0 m, fracture spacing from 20.0 to 17.5 m, and percentage of ice wedges fracturing from 76% to 66%, results (Fig. 2.3D).

Many ice-wedge networks found in lowland sub-Arctic landscapes have developed in the drained basins of thaw lakes, lakes that formed and expanded by the melting of ice-rich permafrost (*1*, *29*). In this setting, approximately 0.1 m of snow accumulates in the wind-swept basin during the first winters following draining, but snow depth increases to approximately 0.5 m after about 5 y because plants that colonize the lake floor trap blowing snow (*3*). Snow acts to decrease maximum tensile stress because it significantly buffers falling winter temperatures. To model this scenario, maximum tensile stress was set to 5 MPa for the first 5 y of network development and to 1 MPa thereafter. The spacing of the initial ice-wedge pattern in this lake-floor network, 17.7 m, is reduced to 16.7 m after 5 y (Fig. 2.2C, 2.3E); no new wedges are added to the network thereafter because the maximum tensile stress is reduced below the threshold for fracture initiation in permafrost. The mean spacing between fractures increases from 17.8 m in the fifth year to 22.3 m thereafter; the percentage of ice wedges that fracture decreases from 91% at high tensile stress to 65% after tensile stress is reduced. Despite developing principally

under a maximum tensile stress insufficient to fracture frozen ground, ice wedges in the lake-floor network grow at a rate close to that of the reference model. More so than in the other numerical experiments, ice wedges that are long, and therefore contain more potential sites for fracture initiation, tend to fracture with greater frequency than short wedges (*30*). Some short ice wedges rarely fracture, dropping out of the visual pattern of ridges and troughs because of relaxation of ground surface morphology (Fig. 2.2C).

The variations in fracture frequency found in the model suggest a mechanism for the development of the low and narrow, barely visible ramparts that appear at the ground surface of some ice wedge networks (Fig. 2.1). As in the model (Fig. 2.2C), these ridges probably delineate ice wedges that fracture infrequently relative to other wedges in the network. Because this effect is enhanced if ice wedges develop under climatic conditions less extreme than the initial formation of the network, significant variations in wedge width and rampart height might be indicative of climate change. This mechanism for low ridges conflicts with an alternate proposed mechanism in which it is hypothesized that the corresponding ice wedges recently have been added to the network because of changes in climate or changes in vegetation over old ice wedges (*15*).

In the model, ice wedge networks approach a steady-state pattern in which not all wedges fracture in a single year. In an average year, a lower percentage of wedges fractures as variations in tensile stress owing to variations in climatic forcing increase. The networks are highly sensitive to extreme conditions; even a short string of high maximum tensile stress fracture episodes can lead to a permanent reduction in the spacing between wedges. A brief exposure to high tensile stress conditions can lead to the

formation of an ice wedge network that then develops under conditions that would have been insufficient for initial formation. Long ice wedges fracture more frequently than adjacent short wedges. The fate of an ice wedge, once formed, depends on its length, the length and relative position of its neighbors, and the imposed tensile stress, and not on the bulk characteristics of the network.

We interpret these results to have the following implications for using ice wedge networks to infer paleoclimate. First, the characteristics of ice wedge networks, including wedge spacing and width, largely reflect extreme climatic conditions during the formation of the network, not mean conditions. Second, the existence of relic networks delineating ice wedges melted long ago over vast expanses of North America, Europe, Asia and southern South America (*13-16*) are not necessarily indicative of sustained cold climates in these locations during the Pleistocene. Third, measurements that show that only 40-70% of ice wedges at sites in northern Canada and Alaska fracture each winter (*8, 10*) are consistent with steady climate conditions, and do not imply warming. Fourth, information regarding the conditions under which ice wedges have developed and grown versus the conditions under which fractures in permafrost first developed might be contained within the range of ice-wedge widths.

The characteristics of ice wedge networks and their response to climate forcing reflect an interplay between fracturing, ice wedge growth and network development, all nonlinear, dissipative processes with differing intrinsic time scales. Our model for the evolution of ice-wedge networks shows complex behavior under a range of climate scenarios. This suggests the need for caution in inferring the response of ice-wedge

networks and other, more complicated geomorphic systems to climate change using simple models or conceptions of their behavior.

References and Notes

1. H.M. French, *The Periglacial Environment* (Addison Wesley, Harlow, 1996).
2. A.H. Lachenbruch, *Geological Society of America Special Paper* **70**, 69pp. (1962).
3. J.R. Mackay, *Can. J. of Earth Sci.* **23,** 1782 (1986).
4. J.R. Mackay, *Can. J. of Earth Sci.* **30,** 1720 (1993).
5. L.J. Plug and B.T. Werner, *J. of Geophys. Res.* (in revision). L.J. Plug and B.T. Werner, *Permafrost Seventh International Conference Proceedings,* 897, A. Lewkowicz and M. Allard, Eds. (Univ. of Laval Press, Quebec, 1999).
6. J.R. Mackay, *Can. J. of Earth Sci.* **11,** 1366 (1974).
7. J.R. Mackay, *Can. J. of Earth Sci.* **21,** 516 (1984).
8. J.R. Mackay, *Can. J. of Earth Sci.* **29,** 236 (1992).
9. J.R. Mackay, *Can. J. of Earth Sci.* **30,** 509 (1993).
10. R.F. Black, in *Glacial Geomorphology*, D. Coates, Ed. (State Univ. New York, Binghamton, 1974) pp. 247-275.
11. J.R. Mackay, *Permafrost and Periglacial Processes* **1**, 15 (1990).
12. J.R. Mackay, *Can. J. of Earth Sci.* **32,** 1093 (1995).

13. W.H. Johnson, *Quat. Res.* **33**, 51 (1990).

14. T.L. Pewe, *Proceedings of the First International Permafrost Conference*, pp. 76-81, National Academy of Science and National Research Council, Publication 1287 (1966).

15. R.F. Black, *Quat. Res.* **6**, 3 (1976).

16. For examples of relic networks and their use to infer characteristics of paleoclimate, see, for example, H.W. Borns, *Science* **148**, 1223 (1965); J.C. Walters, *Permafrost and Periglacial Processes* **5**, 269 (1984); E. Kohlstrup, *Palaeogeography, Palaeoclimatology, Palaeoecology* **56**, 237 (1986); S.A. Grosso and A. E. Corte, *Geografiska Annaler Series A-Physical Geography* **71**, 125 (1989); L.A. Owen et al., *Journal of Quaternary Science* **13**, 539 (1998).

17. M. Allard, *Proc. AGU Western Section Annual Meeting*, San Fransisco (1998).

18. The values of tensile strength for frozen ground and ice are assumed to lie at the lower limits of the measured peak tensile strengths of small samples of homogenous ice-rich frozen silt and freshwater ice [Y. Zhu and D.L. Carbee, Army Cold Regions Research and Engineering Laboratory, Report 87-14 (1987); L.W. Gold, *Journal of Glaciology* **19**, 197 (1977)].

19. Tensile stress $\sigma_{kl}(\theta)$, the stress perpendicular to angle θ in cell *kl* , is pre-fracture thermal tensile stress, σ_T, minus the sum of reductions from nearby open fracture segments in cells *ij*, according to

$$\sigma_{kl}(\theta) = \sigma_T \left(1 - \sum_{ij} \frac{3}{\left(d_{ijkl}\right)^2} \cos(\beta_{ijkl}) \sin(\alpha_{ijkl}) \right) , \quad (6)$$

where d_{ijkl} is the distance (in m) from the center of cell *ij* to the center of cell *kl*, β_{ijkl} is the difference between the angle of the fracture in cell *ij* and angle θ, and α_{ijkl} is the angle between the line segment connecting cell *kl* and cell *ij* and the normal to the fracture segment in cell *ij* (*5*).

20. The elastic energy released as fractures open, **G**, is calculated from the pre-fracture tensile stress along the 5 m of fracture path preceeding the position of the fracture tip, linearly weighted toward stresses near the tip, and from the shear stress across the fracture plane at the fracture tip, as described in ref. *5* [see also B.R. Lawn, *Fracture of Brittle Solids* (Cambridge Univ. Press, Cambridge, ed. 2, 1993)]. G_o, the energy required to create new fracture surfaces, acts as a material-dependent threshold for propagation. It is estimated as the average of the values of the two cells that lie ahead of the fracture tip along the propagation angle, weighted by the inverse square of distance from the tip.

21. $P(\theta,\Delta\theta) \propto \exp(\Delta G(\theta+\Delta\theta)/G_{random})$, where $P(\theta,\Delta\theta)$ is the probability that propagation angle changes from θ to θ+Δθ, and G_{random} parameterizes the magnitude of heterogeneity in frozen ground and in tensile stress (*5*).

22. G_o is set to 1.5 J m^{-2} in ice-wedge cells [D.J. Goodman and D. Tabor, *Journal of Glaciology* **21**, 651 (1978)] and to 8 J m^{-2} in frozen ground cells. G_o in frozen ground

has not been measured, to our knowledge. It is greater than that for ice, because fractures consistently follow the axis of wedges in natural networks, but is of similar magnitude because the two materials are rheologically similar. G_{random}, is set to 0.5 J m^{-2} so that isolated fractures in the model follow irregular paths similar to paths of first fractures in frozen ground (*3*, *5*).

23. Measured annual increments of ice-wedge growth, typically 0.002 m (*6*, *10*) in ice wedges, are much less than the maximum width of open fractures, typically 0.01 m (*6*), suggesting that these increments are limited by availability and penetration into the fracture of blowing snow, frost hoar and melt water, and therefore are independent of tensile stress.

24. The common case of a ridge that forms over an ice wedge by upward deformation centered on the wedge is assumed. Other modes of deformation, the cause of differences between them not well understood, can result in a range of different morphologic responses (*1*).

25. T.C. Hanks, R.C. Bucknam, K.R. Lajoie, R.E. Wallace, *J. Geophys. Res.* **89**, 5771 (1984). B. Hallet and J. Putkonen, *Science* **265**, 937 (1994).

26. B.T. Werner, *Science* **284**, 102 (1999). H. Haken, *Synergetics* (Springer-Verlag, Berlin, 1983).

27. Maximum annual tensile stress is estimated using the assumption of a viscoelastic rheological model for frozen ground prior to fracture, a cooling rate of 10 °C day^{-1} and a quasi-viscous parameter, $\bar{n}$, of 8 x 10^{25} N^3 m^{-6} s, where $\bar{n}$ relates the rate of

permanent quasi-viscous strain $\dot{E}$ under a constant sustained stress P in $P^n = 2\bar{n}\dot{E}$ (see discussion on stress before fracture in *2*).

28. An increase of maximum annual stress to 5 MPa (from reference model value of 3 MPa) might be caused by a decrease in the absolute ground temperature with a corresponding increase in quasi-viscous parameter, $\bar{n}$ (*2*). For $\bar{n} = 40 \times 10^{25}$ N^3 m^{-6} s, tensile stress = 5 MPa. For $\bar{n} = 0.4 \times 10^{25}$ N^3 m^{-6} s, tensile stress = 1 MPa. Freshwater ice, similar in rheology to ice-rich frozen ground, exhibits these values for $\bar{n}$ at temperatures ranging from -40 °C to -10 °C (*2*). Changes in absolute ground temperature are one route to changes in maximum annual tensile stress; changes in the rate of temperature change can also cause variations in maximum annual tensile stress of similar magnitude (*2*).
29. D.M. Hopkins, *J. of Geol.* **57**, 119 (1949).
30. The abandonment of some wedges by the annual fracture pattern is insensitive to the growth increment of wedges; therefore, model results are not significantly affected by an increase in wedge growth increments to approximately 0.01 m over the first 5 years of network development, as has been measured in a drained lake (*3*).
31. Supported by the National Science Foundation, Arctic Natural Sciences Program (OPP-9530860), and the National Park Service, Bering Land Bridge National Preserve, Beringian Shared Heritage Program.

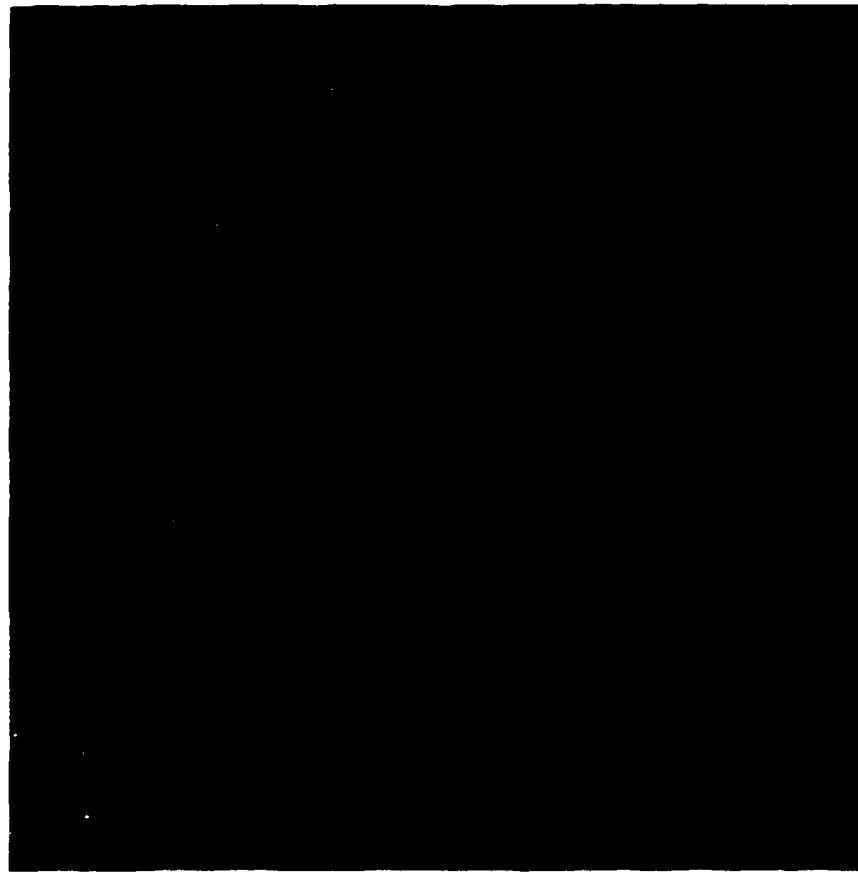

FIGURE 2.1. Near-infrared aerial photograph of ice-wedge network on floor of a drained lake near Espenberg, NW Alaska. Ridges 0.25 - 1 m in height and spaced 10 - 30 m apart overlie ice wedges and appear light because they are dry and covered by herbaceous vegetation. Troughs appear dark because of wet sedge-tundra vegetation or standing water. Provided by the National Park Service.

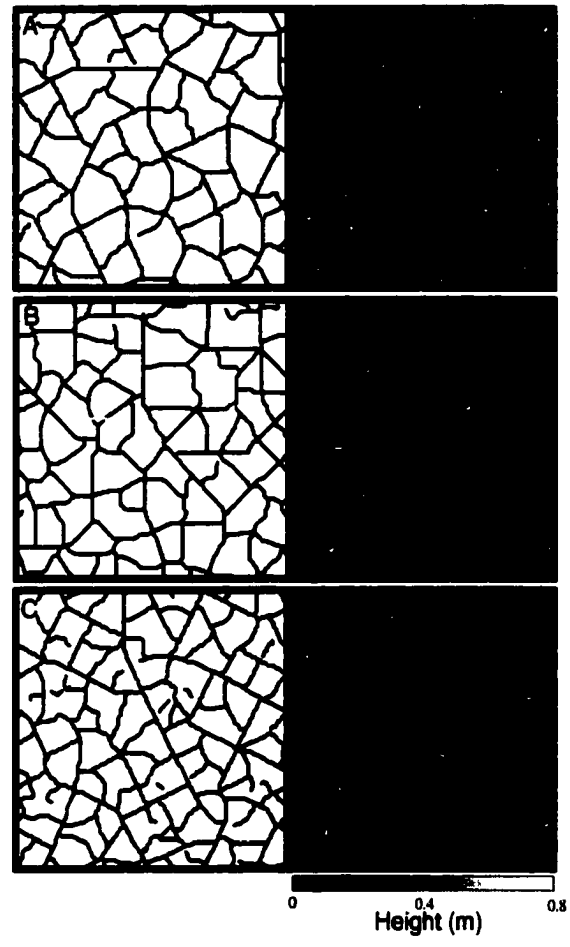

FIGURE 2.2. The pattern of fractures in the first year (A-B) or pattern of ice wedges in the fifth year (C) (left panel) and the ground surface morphology over ice wedges after 1500 fracture episodes (right panel). Three modeled networks, each with different history of maximum annual tensile stress, are shown: *A)* reference network; *B)* broad-stress network; *C)* lake-floor network.

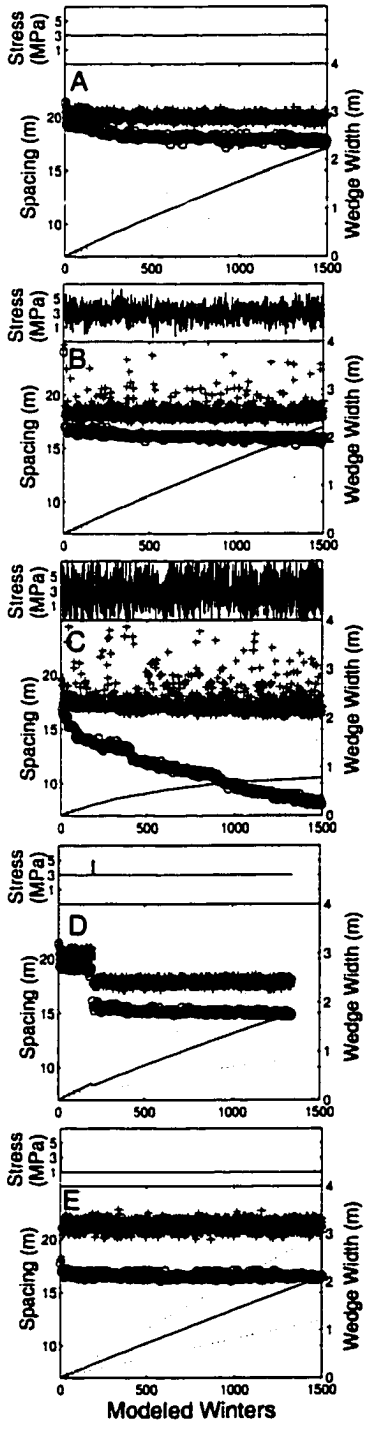

FIGURE 2.3. Changes through time in spacing between ice wedges (circles), spacing between fractures in the annual fracture pattern (crosses) and width of ice wedges (solid line is mean, dotted lines are 1 σ envelope) for five modeled networks, each developed under different scenarios of maximum annual thermal tensile stress (shown in upper panels): *A)* Reference network; *B)* narrow-stress network; *C)* broad-stress network; *D)* temporary high-stress network; *E)* lake-floor network. Spacing is the median of 5000 measurements of spacing between fractures or ice wedges, measured along sample lines that cross a network at randomly selected angles and originate from randomly selected locations (*5*).

Development of Peat-Decomposition Ponds in a Permafrost Wetland[1]

Abstract

Newly-described ponds 2 m across and 1 m deep in permafrost wetlands at the Espenberg beach-ridge plain, Bering Land-Bridge National Preserve, Alaska, initiate and deepen through an interplay between localized decomposition of peat and thawing of ice-rich frozen ground. Groups of tens to hundreds of ponds develop over hundreds to thousands of years, because raised rings (up to 1 m high and 3 m across) of ice-rich moss and shrub peat that surround ponds favor the formation of a new pond by reducing rates of peat accumulation adjacent to the ring. In a rule-based model that encapsulates this hypothesis for interaction between ponds, ponds self-organize into groups with distributions of spacing between ponds consistent with spacings between ponds at Espenberg, whereas models encapsulating stochastic placement of ponds produce groups of ponds inconsistent with groups of ponds at Espenberg. The stability of ponds of the characteristic size, vs. instability of thaw lakes, is attributed to the size of the thermal disturbance caused by ponds, which is a function of depth and diameter of a pond. This stability implies that these ponds are smaller than the minimum size of a pond that can initiate an unstable thaw lake, lakes that grow in lowland sub-Arctic terrain by melting and slumping of ice-rich permafrost at their periphery.

[1]Lawrence J. Plug. Prepared for submission to *Quaternary Research.*

Introduction

Water bodies in Arctic and sub-Arctic landscapes can grow from ponds (m^2) to lakes (km^2) over hundreds to thousands of years by thawing and collapse of ice-rich frozen ground at their margins (Hopkins, 1949; Billings and Peterson, 1980). In tundra lowlands of northern Alaska and Canada, the thaw lakes that grow by this mechanism play a dominant role in determining surface morphology, hydrology, drainage patterns, vegetation, development of organic soils and ocean shoreline erosion (Britton, 1957; French, 1974; Sellman *et al.*, 1975; Billings and Peterson, 1980; Seguin and Allard, 1984; Ruz *et al.*, 1992; Jorgenson *et al.*, 1998) and serve as conduits to the atmosphere for water vapor, CH_4 and CO_2, greenhouse gases sequestered in frozen organic soils (Kling *et al.*, 1991).

Thaw lakes have been described to cyclically initiate as small ponds, enlarge into lakes and drain (Hopkins, 1949; Britton, 1957; Billings and Petersen, 1980). The cycle begins with a disruption of vegetation or soil at the ground surface that leads to deeper than normal seasonal thawing. If the volume of ice in the upper-most permafrost exceeds the porosity of unfrozen material, the ground subsides on thawing and a new pool initiates. Water that pools in the resulting depression because of impermeable underlying permafrost is preferentially warmed by sunlight and conducts and advects heat to margins of the depression where frozen soil thaws. Small ponds increase in size by thaw-derived subsidence, collapse of thawed banks and subaqueous sediment flows (e.g. Hopkins, 1949; Merton, 1996). Lakes can grow to diameters of several kilometers, with ultimate

size limited by cooling of climate or by topographic limits such as horizontal pinching out of ground ice or intersection of a stream channel that causes the lake to drain (e.g., Hopkins, 1949; French, 1974; Walker, 1978; Merton, 1996). Following drainage, new, ice-rich permafrost forms in the lake-floor sediments (Britton, 1957; Billings and Petersen, 1980; Mackay, 1986). The development of a new, unstable thaw pond completes a cycle with duration of order 10^3 - 10^4 years (Billings and Petersen, 1980).

Conditions for the initiation of a new, unstable pond that enlarges into a thaw lake are poorly constrained. Reported and hypothesized mechanisms for locally deeper thawing in summer are numerous, including changes in climate (French, 1987; Tomirdiaro, 1982; Rampton, 1988), and disruption of the ground surface by fire, animals, flood-rafted peat blocks, humans and ice wedges (Hopkins, 1949; Aleshinskaya *et al.*, 1972; Billings and Petersen, 1980; Mackay, 1970; Heginbottom, 1973; Ugolini, 1975; Kerfoot, 1974). Whereas there might be a large number of mechanisms for thermal disruption leading to unstable thawing (French, 1996, p.110), not all perturbations in the extent of seasonal thawing lead to the generation of a new, unstable thaw lake, as suggested by the discontinuous distribution of thaw lakes across thaw-susceptible ice-rich permafrost landscapes. The minimum size of an unstable thermal disturbance, likely to vary as a function of substrate type and climate, is not known.

The limiting size of an unstable pond that can grow into a thaw lake is indicated by new observations, reported here, of stable ponds in ice-rich permafrost (Figure 3.1). These ponds form by an autogenic, biotic mechanism. Large numbers of ponds, organized into groups with a common spacing between ponds, develop over time because

existing ponds effect the initiation of a new pond by causing changes in surface morphology of the adjacent ground. Once formed, ponds are stable features whereas thaw lakes are not. Here, I describe properties of these ponds, present and test a model for the development of new ponds and argue that the stability of ponds constrains the size of a minimum disturbance required for the initiation of a thaw lake in one type of thaw-susceptible permafrost.

The ponds described here are called 'whale-hole ponds' by local residents of the northern Seward Peninsula, because Inupiak legend ascribes their origin to whales that breached while swimming beneath the Espenberg spit (personal communication from Fred Goodhope Jr. and Perry Weioyanna of Shishmaref, Alaska, 1995). In the remainder of this paper, use of the word 'pond' refers specifically to whale-hole ponds except where otherwise specified.

Espenberg Beach-Ridge Plain

Whale-hole ponds occur in permafrost wetlands on the Espenberg beach-ridge plain, a 30 × 2 km shore-attached sandy spit on the northern coast of the Seward Peninsula, Alaska (Figure 3.2). The beach-ridge plain has been constructed over the period from approximately 4500 BP to the present, interrupted by an interval of shoreline transgression and dune building from approximately 3300 - 1700 BP and an interval of dune building at approximately 1200 - 0 BP. These interruptions are evident from fore-dune complexes along the modern shoreline and relic dunes that form the 14th ridge (Figure 3.3) (Mason *et al.*, 1997). The ages of ridge and swale surfaces at Espenberg are

established by a suite of C_{14} dates on artifacts, basal peats, marine shells and organic stringers buried in beach sand (Figure 3.3). These radiocarbon-dated samples provide a chronology for the evolution of landforms on the Espenberg spit, including the whale-hole ponds discussed here, that form in the swales between beach ridges (Plug, 1994a). Because of intervals when shoreline position was stationary or transgressive, not all surfaces of a given age are equally represented at Espenberg, with some absent because of the 3300 - 1700 BP transgression. Swales older than 1200 y have variable widths but tend to be wide (up to 100 m across) whereas younger swales, where present, are only tens of meters across.

Peat accumulates in the swales at Espenberg because soils are cool and permafrost, once formed, maintains a high water table that slows decomposition of plant litter. The development of vegetation in swales follows a successional sequence from beach species through to mixed wetland communities (Plug, unpublished data; Schaaf and Barker, nd). On the modern beach and in the first swales, which are not yet underlain by permafrost, disturbance-favored xeric species such as *Elymus arenarius mollis* (rye grass) are found, followed in the next swales by the introduction of shrub-tundra species including *Empetrum nigrum* (crowberry), *Vaccinium uliginosum* (blueberry), and *Salix* spp. (willow). Permafrost has developed to within 1.5 m below the surface of the third swale and here the first wetland species, including *Carex saxatalis* (sedge), appear on moist sandy soils. Peat accumulates rapidly in response to this change in vegetation and soil moisture and reaches depths of 30-40 cm in the 4th swale. The 4th and 5th swales are underlain by permafrost < 0.75 m below the surface and support a mesic sedge-

dominated community of *C. lyngbyaii*, *C. aquatilis*, *Petasites hyperboreus*, *Betula nana* (dwarf birch) and *Salix spp.* (willow). The smooth surface of peat is disrupted by hummock development in the 6th swale, marked by the addition of *Ledum palustre* (Labrador tea), *Rubus chamaemorus* (salmonberry), *Eriophorum angustifolium*, and *E. subarcticum* (cotton grass). From the 8th swale onward, a stable community of fen and poor fen vegetation dominated by sedge and cotton grass grows in wet organic soils with a shallow active layer (< 0.5 m). This assemblage is interrupted by patches of bog vegetation of sphagnum and ericaceous shrubs on the raised surfaces of palsa mounds and ramparts over ice wedges. Depth of peat increases with swale age, reaching 1.75 m on the 4500 BP swale at the lagoon shore.

Climate and Ground Ice

The northern Seward Peninsula is near the southern margin of the zone of continuous permafrost, a region generally susceptible to thawing and subsidence of ice-rich frozen ground (French, 1996 p. 112). The mean annual air temperature is -5.8°C at the nearest permanent meteorological station, at Kotzebue, Alaska, which is at a similar coastal position 40 km to the east and has comparable climate (all climatological measurements from NOAA, 1999 and WRCC, 1999). Summer and autumn seasons are moderated by proximity to the Chukchi Sea (mean July temperature is 12.0°C). Ice covers the Chukchi Sea most winters, and winter climate is therefore cold and dry. The average daily minimum temperature in December through March is -23°C; daily minima range as low as -47°C. Mean maximum annual snow depth is 0.5 m, occurring in early April. Snow is

redistributed into drifts and snow-free patches by winter winds, as sustained gusts greater than 32 kmh^{-1} occur most days during winter.

The perennially frozen organic soils in swales at Espenberg have excess ice and therefore are susceptible to consolidation and subsidence upon thawing. In eight cores through peat to the underlying sand (distributed along transect A, Figure 3.2), pore ice and ice lenses up to several centimeters thick are common. Based on measured values of consolidation in samples from a core extracted near the lagoon shore at site B (Figure 3.2, Table 3.1), the average consolidation on thawing for perennially frozen organic soils at Espenberg is estimated to be 50%. An even greater consolidation is likely owing to the presence of ice wedges (bodies of massive ice in frozen ground), marked by networks of ramparts that criss-cross swales older than approximately 1200 BP.

Ponds and Raised Rings

Properties of ponds and the swale pedants in which they are set were documented during five trips to the Espenberg beach-ridge plain from 7/93 to 10/96, spanning late spring to early in the freezing season (Appendix A), and from 1:6000 scale aerial photographs (NPS, 1986).

Ponds with diameters of approximately 2 ± 1.2 m and water depths of 1.1 ± 0.4 m (over 20 ponds drawn at random) are widely distributed in swale wetlands at Espenberg (Figures 3.1, 3.4 and 3.5). Ponds have roughly cylindrical bathymetry, characterized by steep sides, flat or gently concave floors and nearly round surfaces (ratio of the major to minor axis of pond diameter is 1.5 ± 0.5 over 100 measured ponds). Floors of ponds are

frozen sand or peat, commonly covered by a < 5 cm layer of unconsolidated woody detritus. Highly decomposed flocculent peat covers the floor of some particularly shallow ponds. The water in ponds is clear of suspended sediment but is stained a deep humic brown. Ponds are devoid of terrestrial vegetation, but some ponds contain floating algal mats. Pond water is roughly neutral (pH = 7.2 ± 0.1). Soil water in adjacent fen and poor fen wetlands is slightly more acidic (values of soil water pH range from 6.7 ± 0.3 to 6.3 ± 0.4, generally decreasing with swale age (Plug, unpublished data).

Most ponds at Espenberg are surrounded by rings 1 - 2 m wide (Figure 3.1), which rise 0.25 - 1 m above the surface of the surrounding wetland. Permafrost beneath rings rises in a pattern that mimics the topography of the surface and is particularly rich in ice lenses and in pore ice. The vegetation community on rings includes *Sphagnum* spp., *Rubus chamaemorus, Vaccinium uliginosum, V. vitis-idaea, Betula nana, Andromeda polifolia.* This assemblage and the acidic soil water in rings (pH = 4.5 ± 0.2) are characteristic of bogs and hummocks. A thin mat of reindeer lichen commonly spans upper surfaces of rings that are > 0.5 m high. In fen surfaces adjacent to raised rings, discontinuous shallow depressions and regions of degrading peat are common (Figure 3.1).

Although isolated ponds are common, particularly on young swales (approximately 1000 - 1200 BP) with peat at Espenberg, most ponds occur in groups of tens to hundreds of ponds (Figure 3.1A-C, Figure 3.4). The number of ponds within these groups generally increases with swale age. The minimum edge-to-edge spacing between ponds is typically

2 - 3 m. Within groups of ponds, raised rings around individual ponds merge to form uneven plateaus standing 0.5 - 1 m above the surrounding wetland. Vegetation on these raised areas is identical to vegetation on individual rings. Many large groups of ponds are adjacent to lakes (>100 m^2 in area) that appear to have grown through breaching and incorporation of ponds, as shown by lake margins that are frilled by breached pond basins (Figure 3.1C) and by remnants of pond basins visible on floors of some lake basins.

Pond Basins

Basins of three ponds were examined to document the stratigraphy of peat around and beneath the floor of ponds (Figure 3.2, sites C-E), including *1)* a pond on a swale approximately 1500 years old that was manually bailed (Figure 3.5); *2)* a partly eroded pond basin on a 4500 BP swale, revealed in section at the subsiding and eroding lagoon bluff (Figure 3.6); *3)* a pond basin 2 m from the lagoon shore and ~20 m from 2, naturally drained by landward thawing of permafrost (Figure 3.7). Basins of the eroded pond and the naturally drained pond are located approximately 20 m from the site of a long core through frozen peat and into the underlying sand (Table 3.1).

Initiation and Development of Ponds

Numerous mechanisms have been proposed for the development of ponds in lowland permafrost terrain. However, these mechanisms are inconsistent with properties of ponds at Espenberg. Thawing of ice wedges can form patterns of ponds, but the characteristic spacing between ice wedges in the Espenberg region (~20 m) is much larger than the spacing between ponds (~ 3 m) and this mechanism does not account for well-developed,

isolated ponds found on young swales that do not yet have ice-wedge ramparts. Thawing of isolated pockets of ice-rich permafrost in peat can form shallow ponds in regions of discontinuous permafrost (Seppälä, 1986), but the climate of Espenberg is sufficiently cold to form and maintain continuous permafrost. Ponds in some peatlands might also be relics of the morphology of the initial mineral surface that have subsequently deepened by accumulation of peat around, but not in, the pond (Boatman *et al.*, 1981). However, precursors to ponds are not found in flat, sandy surfaces of young swales at Espenberg. Proposed mechanisms in which linear ponds initiate by flowing water or slush across a sloping wetland (Seppälä and Koutaniemi, 1985) are implausible on flat swales and inconsistent with round ponds at Espenberg.

The formation and deepening of pools by decomposition of peat has been proposed for pools in patterned peatlands (called 'strangemoor' or string mires) in regions without permafrost (e.g. see review in Seppälä and Koutaniemi, 1985; Foster *et al.*, 1988; 1983). Palsas, regions of raised peat several m^2 in area and larger, have been observed to form by heaving of the ground surface over several freezing seasons in response to local shallow snow cover and abundant supply of water (Seppälä, 1982; 1986). I argue that ponds and raised rings at Espenberg form by localized peat degradation concomitant with heaving of adjacent frozen ground, in combination with lowering of pond floors by thawing of ice-rich permafrost. In the following, the hypothesized mechanism is outlined and observations consistent with this hypothesis are described.

Conceptual Model

The hypothesized mechanism has four steps: *(1)* initial accumulation of a blanket of peat in swales; *(2)* localized onset of peat decomposition and formation of a pool; *(3)* development of a raised ring around a pond through frost heaving; *(4)* decrease in peat accumulation rate and formation of a pool adjacent to the raised ring. Repetition of steps 2 - 4 leads to the development of groups of ponds through time.

(1) Peat forms in swales at Espenberg in response to the formation of permafrost, which impedes drainage and leads to a water table near the ground surface in the otherwise (when unfrozen) well-drained sandy substrate. There is no swale-parallel slope to drive drainage along swales. The top of permafrost in the beach ridges commonly is higher than swale surfaces, impeding groundwater flow perpendicular to swales.

(2) Micromorphology develops in the wetland surface as hummock-forming vegetation, which accumulates peat rapidly, grows alongside poor peat producers (e.g. Foster *et al.*, 1983; Robinson and Moore, 1999). Because humified peat has low hydraulic conductivity, surface water tends to pool at low spots on the surface. During the spring snowmelt and following summer rain storms when the water table is high, plant growth is inhibited in shallow pools leading to local deepening with respect to the wetland surface. Once standing water persists in pools throughout most of the growing season, growth of vascular plants slows and peat accumulation ceases (Foster and King, 1984). Microbial decomposition of peat is favored in the oxygenated, well-mixed water of the pool (Sjörs, 1963). As the insolated surface area of the pool expands, increased heat flow into the

ground causes deeper seasonal thawing of underlying permafrost. The pool deepens as the floor subsides by consolidation of thawed, ice-rich permafrost.

(3) In late fall, when the water table at Espenberg is lowest, frost penetrates early into the banks of a pool where peat is cooled by air from the top and from the side. Segregation ice forms through migration of water toward the freezing front from the still-unfrozen pond and the surrounding wetland and raises this surface slightly above the level of the wetland (Seppälä, 1982; 1986). During the growing season, an annulus around the pool is drier than the surrounding wetland because the surface remains slightly raised. *Sphagnum* becomes dominant, increasing early penetration of frost in winter because of exposure and reduced water depth (Worsley *et al.*, 1995). Bog vegetation taxa that colonize the ring accumulate peat twice as rapidly as fen species (Robinson and Moore, 1999). Enhanced frost penetration promotes further growth of ice beneath the ring as the sides of the ring steepen (Seppälä, 1986; Seppälä, 1994). Once the ring is high enough to collect drifting snow during freeze-up, the horizontal expansion of the ring ceases because frost heaving is inhibited at the edge of the ring (Seppälä, 1994). The ring grows higher by accumulation of peat until lichen appears at the summit (Zoltai, 1993).

(4) The growth of vascular plants is reduced and peat accumulation slows adjacent to raised rings, where snow that drifts against rings persists into the growing season and where permafrost in raised rings dams movement of water through the active layer, forming shallow pools. Micromorphology that develops in this region where hummocks grow beside poor peat producers marks the initiation of a new pond.

Peat Decomposition, Stratigraphy and the Distribution of Ponds

The distribution of hummock-forming vegetation vs. the distribution of ponds at Espenberg is consistent with an autogenic, biotic origin for differential peat accumulation in the initiation of ponds. The youngest surface on which ponds occur is older than the youngest swale in which hummocks have formed; hummocks and shallow depressions appear in the 6th swale (600-800 BP) whereas the youngest swale with ponds is the 8th swale (1200 BP). Shallow pools that have standing water even in autumn, when the wetland is driest, are found on the youngest hummocky surfaces and might be analogues for early stages in the development of ponds. Conditions in these pools are favorable for decomposition; measured concentrations of dissolved oxygen range from 3 to 11 mg l^{-1}, comparable to values from freshwater lakes and ponds where organic material are rapidly decomposed (Schwoerbel, 1987).

Stratigraphy of walls and floors of the three pond basins (the bailed, the drained and the eroded basins) is consistent with the hypothesis that these pools have deepened through peat decomposition (Figures 3.5-3.7). Frozen beach sand, topped by a thin mat of detrital twigs, forms the floor of the bailed pond which lies in a 1500 BP swale. In excavations of the floors and walls of the drained pond and the eroded pond, the firm peat below the loose mat of woody detritus is continuous with peat in the pond walls (Figures 3.6-3.7). A radiocarbon date on a twig *in situ* in peat beneath the floor of the eroded pond is 4480 ± 80 (β-67696), indicating that peat has not accumulated since this time or that the pond has deepened by decomposition. The unconsolidated mat of woody detritus on

the bottom of most pools is consistent with concentration of woody material by decomposition of less fibrous sedges and mosses. In addition to the absence of organic sediment in ponds, active humification of peat might be indicated by the increasing darkness of peat toward the water interface in pond walls (Foster *et al.*, 1984) and by the release of gas bubbles (probably methane and carbon dioxide) when walls and floors of some ponds are agitated.

The depth of ponds and the dip of peat in pond walls into ponds are consistent with deepening of pond basins by localized thawing of ice-rich frozen ground. Unfrozen sedge peat around the bailed pond (Figure 3.5, Unit D) dips into the basin at an angle of approximately 15°, suggesting subsidence centered on the pond. Horizontally layered, perennially-frozen sedge peat beyond this region of dipping peat might represent the original, flat wetland topography. Disregarding possible thaw-subsidence, a peat decomposition rate of roughly 3-4 mm y^{-1} is required to account for the development of a 1 m deep pond on a 1400 BP surface within 300 y, assuming the formation of ponds shortly follows the first occurrence of hummocks. This rate is significantly higher than the rate that can be inferred from stratigraphic evidence for development of ponds by peat decomposition in patterned fens in Labrador (Foster and King, 1984).

The composition of peat in raised rings is consistent with the view that rings grow through frost heaving and through a shift from fen to bog vegetation. Peat in raised rings is primarily ericad and moss peat, whereas sedge peat is found at greater depths beneath rings (e.g. Figure 3.5) and in the rest of the wetland. The character of the modern vegetation and the acidity of the soil water are consistent with an ombrotrophic bog,

which accumulates peat rapidly, in contrast to fen and poor-fen conditions in the rest of a swale.

Peat and thin mineral-rich layers that compose rings are involuted and folded, characteristic of post-depositional vertical and horizontal deformation owing to accumulation of segregation ice, as shown in a section through the now-thawed ring of a drained pond (site D) (Figure 3.7). These properties are consistent with the view that rings are a form of palsa, long-lasting raised features 1 - 100 m^2 in area that develop in peatlands by migration of water toward a local freezing front along free-energy gradients (Williams and Smith, 1991). Palsas have been observed to form in peat where rapid local freezing during early winter is facilitated by shallow snow cover or disruptions in vegetation and where a supply of liquid water is available nearby during freeze-up (Seppälä, 1982; 1986), conditions compatible with slightly elevated surfaces at the margin of a pond.

Observations of pooling and peat degradation around rings and at the margins of groups of ponds are consistent with the onset of a new pond by differential peat accumulation around the raised ring of an earlier pond. The depressions around rings are sporadic (e.g. Figure 3.1), rather than forming an undifferentiated annulus, perhaps because snow drifts around rings are not uniform but depend on local wind patterns. Shallow ponds occupying similar depressions in peat around palsas are common in Fennoscandia (Seppälä, 1986). Their origin has been attributed to melting of ice in a decaying palsa, but moat-like depressions are also apparent around young and mature

palsa that are still growing (Seppälä, 1986, Figure 3.8), suggesting that the onset of these pools may also be due to persistent snow drifts or another mechanism.

The increase with swale age of the number of ponds and the size of groups of ponds is compatible with the hypothesis that rings around ponds favor the formation of new, adjacent ponds, but does not preclude other mechanisms. In the youngest swales with ponds, the ponds occur alone or in small groups (e.g. Figure 3.1A-B). In the swales immediately north of the 14th ridge (~1800 BP) most ponds occur in groups of 10-50 ponds. On old surfaces, groups of ponds typically span the width of a swale or are bounded by lakes (Figure 3.1C). Although these observations are consistent with Step 4 in the conceptual model presented above, in which the placement of a ring around a pond leads to the onset of a new pond, an increase in the size of groups of ponds through time might also occur through other mechanisms. For example, peat degradation might have been more favored under mid-Holocene climates than today, thereby causing more ponds to have formed on older surfaces. Alternatively, the number of ponds might increase through time by slow addition of new ponds, randomly distributed across a peat surface susceptible to melting or to localized peat decomposition. A more thorough test is needed to discriminate between different hypotheses for the development of groups of ponds.

Modeled Groups of Ponds

One approach to testing hypotheses for the distribution of ponds is to compare the geometry of groups of ponds at Espenberg with the geometry that would be predicted by each hypothesis.

To achieve this, the development of a group of ponds is represented by the sequential placement of ponds onto a two-dimensional lattice that represents the surface of frozen ground in a swale at Espenberg. Ponds are placed into the swale according to rules that encapsulate hypotheses for pond formation, described below. Ponds are represented as circles of the characteristic size of ponds (2 m diameter), a representation based on the assumption that ponds grow to their characteristic diameter over time scales significantly shorter than that for the development of groups of ponds. Modeled groups of ponds develop within lattices of size 200 × 200 m, an area as large as the width of broad swales and large enough to enclose the large groups of ponds in old swales at Espenberg. The size of a cell in the lattice is 0.2 × 0.2 m. Each cell *kl* in the lattice has a value T_{kl} that is proportional to the probability that a new pond will form centered at that cell.

Three hypotheses for pond placement are represented in the fashion described above:

1) Self-organization model. New ponds primarily form because of localized variations in the rate of peat accumulation on the wetland surface caused by rings surrounding existing ponds, and secondarily because of randomly-distributed variations in micromorphology of the wetland surface, such as hummocks and depressions. In the model, the probability that a new pond will be placed at any position on the plane is

modeled by a Boltzmann equation, according to $P(kl) \propto \exp(T_{kl}/T_{random})$, where T_{random} specifies the degree of randomness in the mechanisms for pond initiation. Each cell *kl* in the lattice representing a swale has an initial value T_o, which is proportional to the probability that a new pond will form at that site. Once placed on the lattice, each pond is surrounded by a ring with radius *r* (Figure 3.8). Beyond this ring is an annulus of width *w*, which represents the region beyond raised rings where the initiation of most new ponds is hypothesized to occur. T_{kl} is set to a new, larger value at all positions *kl* within this annulus. The value of T_{kl} is set to 1 for wetland surfaces, 2 in annuli and 0 in rings and ponds. These values of T_{kl} are arbitrary because the relative likelihood that a new pond will be placed in the annulus beyond the ring of an existing pond vs. another region of the swale can be constrained by varying T_{random}. Ponds are placed one at a time into the modeled swale until the number of ponds is equal to an imposed maximum value, *n*.

2) Random model. New ponds form at randomly distributed irregularities, such as micromorphology in the wetland surface or variations in snow depth. In the model, all positions in the lattice, excluding existing ponds (where T_{kl} is set to 0), are equally likely to develop a new pond because $T_{ring} = T_{annulus} = T_{wetland}$. Ponds are placed one at a time into the modeled swale until the number of ponds equals an imposed maximum value, *n*.

3) Random-spaced model. New ponds form at random irregularities, as above, but rings around ponds develop over time scales shorter than the formation of new ponds and new ponds cannot form in the elevated, well-drained surfaces of rings. This is represented in the model by setting T_{kl} to 0 within ponds and within rings of width *r* around each pond

but to a uniform value throughout the remainder of the swale ($T_{annulus} = T_{wetland}$). Ponds are placed one at a time into the modeled swale until the number of ponds equals an imposed maximum value, n.

Groups of Ponds at Espenberg

For comparison with modeled groups of ponds, four regions of ponds were selected from swales at the Espenberg beach-ridge plain; two from a swale of age ~1800 BP, immediately north of the 14th ridge, and two from old swales near the lagoon bluff (3500 BP and 4500 BP). The positions of ponds were recorded by manually locating ponds on 1:6000 scale color-infrared aerial photographs, using moisture and vegetation differences to delineate ponds. Rather than digitize the somewhat irregular margins of ponds, the outlines of ponds were visually fitted to circles of varying diameter, because resolution of photographs is insufficient to record < 0.5 m scale details of pond margins. The pattern of ponds represented by circles (example in Figure 3.9A) is only slightly different than a pattern of ponds where irregularities in the shapes of ponds are digitized (to the degree possible); for a 50 × 50 m region containing 30 ponds, the difference between circular ponds and digitized ponds is small, less than the difference between two groups of ponds at Espenberg, as measured by the analysis methods used to compare groups of ponds described below.

Analysis Methods

Espenberg and modeled groups of ponds display a wide range of spacings between ponds (Figure 3.9A-B) that cannot be adequately described by a single spacing metric. To quantify and compare the properties of different groups of ponds, measurements of the distributions of pond spacing over a region of ponds are needed. This is accomplished by measuring the spacing between successive ponds along sample lines that cross a group of ponds at randomly selected angles and originate from randomly selected locations (Plug and Werner, in revision). Spacing is the distance between two successive intersections between the sample line and a pond margin, measured along the sample line.

Distributions of spacing drawn from Espenberg and modeled groups are compared using two-sample Kolmogorov-Smirnov (K-S) tests. The essence of the K-S test is to characterize the difference between two distributions using the maximum value of the difference between the corresponding cumulative distributions, D. The significance level, P, of a measured value of D is a function of D and number of observations (Press *et al.*, 1988). Small values of P show that the two distributions are significantly different, whereas large P implies that there is no detectable difference between the two distributions. The number of observations of spacing used to characterize each group of ponds was set to 1000, the largest number at which two groups of ponds generated using the same set of synthetic rules are consistently deemed similar by K-S comparisons (as indicated by a very low confidence for the null hypothesis, $P > 0.1$). P decreases with

increases in the number of observations from this value as the K-S test becomes more rigorous, but no new information has been added because observations are correlated.

Parameter Values

Parameter values for the different models were explicitly chosen to fit modeled groups of ponds to groups of ponds at Espenberg, using the simulated annealing method of optimization (Kirkpatrick *et al.*, 1983). In my implementation, the algorithm initially operates on a modeled group of ponds generated using randomly chosen values for parameters. The modeled group of ponds is compared to an Espenberg group of ponds, using the maximum difference between the cumulative distributions of spacing (D in the K-S test). The probability that the set of model parameters is adopted is a function of this maximum difference and of a control parameter (the annealing temperature) that defines the likelihood that a model configuration that is less optimum than the current configuration will be accepted. By iterating this procedure and perturbing the value of one parameter each iteration, while slowly decreasing the value of the annealing temperature, a set of parameters that is at or near the best fit of the model to an Espenberg group of ponds is reached. This procedure was repeated using all four Espenberg groups of ponds for comparison, with the best-fit parameters for each case saved. Sets of parameters for all three models were chosen in this fashion.

This explicit fitting of the models to groups of ponds at Espenberg was performed to address three questions: *(1)* How well can each of the hypothesized mechanisms, as represented here, account for patterns of ponds at Espenberg? *(2)* Are the parameters that

generate this best prediction consistent with measurable properties of ponds and rings at Espenberg? *(3)* Do groups of ponds, as modeled using parameters chosen to fit models to static patterns of large groups of ponds on old swales, develop in a sequence that resembles the development of groups of ponds at Espenberg, as shown by groups of ponds on swales of increasing age?

Results

A peak around 3-5 m in distributions of spacing drawn from the four Espenberg groups (Figure 3.10A) indicates the characteristic edge-to-edge spacing between ponds. Few ponds are spaced more closely than this. Larger spacings between ponds arise because of variability in pond spacing and because of large spacing between some subgroups of ponds.

These properties of groups of ponds at Espenberg can be qualitatively reproduced by the self-organization model and, to a lesser degree, by the random-spaced model, as indicated by asymmetric peaks at close spacings in their respective distributions (Figure 3.10B-C). In random-spaced groups, the position of the peak in the spacing distribution is determined by r, the width of a ring. Large spacings arise through stochastic placement and the constraint of a maximum number of ponds, which leaves gaps in the pattern of ponds in the modeled swale. In self-organization groups, the peak in the spacing distribution is determined by r and by w, the width of the annulus where the formation of new ponds is hypothesized to be probable. A range of spacings larger than this distance develop in the self-organization model through suboptimal placement of ponds (because

ponds are placed sequentially and their position cannot be adjusted to improve 'packing') and because of gaps left between subgroups that develop around the initially placed ponds.

Groups of ponds developed by the same mechanism can be discerned by K-S comparisons of distributions of pond spacing. This is shown by comparisons between different realizations of the same model; large values of P (> 0.1) imply that there is little difference between the compared distributions (Table 3.2). Self-organized groups of ponds have the largest variability amongst the modeled groups of pond; this variability between realizations arises because the final pattern of self-organized groups is sensitive to the random placement of the first few ponds that determine the position and spacing between subgroups of ponds. The large variability between groups of ponds at Espenberg might be due to a similar mechanism, or to variations in the numbers of ponds in groups at Espenberg.

Properties of three of the four Espenberg groups (1,2 and 4) can be reproduced ($P > 0.1$) by the self-organization model, for which parameters were chosen by simulated annealing (Table 3.3). The degree of similarity between the self-organization model and Espenberg group 3 is only slightly poorer ($P = 0.09$). These comparisons are consistent with the view that self-organized and Espenberg groups of ponds are drawn from the same ensemble. In contrast, the null hypothesis, that groups of ponds are different, can be accepted with a high level of confidence for all comparisons of random and random-spaced groups of ponds with groups of ponds at Espenberg, indicating that these are clearly different from groups of ponds at Espenberg.

The parameter values for which modeled groups of ponds are most similar to Espenberg ponds are consistent with the hypothesis that most new ponds form in a region adjacent to raised rings around earlier ponds (Table 3.3). The values of r (3.2 - 3.7 m) are comparable to the measured width of rings at Espenberg. The values of w (2.9 - 3.8 m) are comparable to distances across regions where discontinuous depressions occur around rings at Espenberg, as observed by the author (these distances have not been quantified, however). Values of T_{random}, 0.29 to 0.38, are a fraction of the relative likelihood of pond placement at a ring versus away from a ring (2.0). This indicates that the effect of modeled rings on favoring the position of a new pond is strong (for T_{random} = 0.3, the probability that a modeled pond will be placed around a ring is approximately 28× greater than the probability of pond emplacement at a position in other regions of the lattice; for T_{random} = 2, for example, the relative probability is only 1.7, so ponds are not highly favored to form adjacent to rings). Parameters for the four realizations of the self-organization model, each realization fitted to a different region of ponds at Espenberg, are alike; this similarity in parameters is consistent with the hypothesis that all groups of ponds at Espenberg form by the mechanism of rings around ponds favoring the initiation of a new pond.

In the self-organization model, groups of ponds assemble by stochastic emplacement of new ponds at positions near the margins of existing ponds (Figure 3.11). Subgroups of ponds grow because new ponds are preferentially placed adjacent to existing ponds. Subgroups of ponds merge as more ponds are emplaced. The final patterns of self-

organized groups of ponds (those where the imposed maximum number of ponds have been placed) is qualitatively similar to Espenberg pond groups, in that ponds within subgroups are closely spaced while larger gaps occur between subgroups and where ponds are sub-optimally placed. This sequence is qualitatively similar to the development of groups of ponds at Espenberg, as shown by changes in the size of groups of ponds across swales of increasing age (Figure 3.1). This result indicates that the hypothesized interaction between ponds is similar to dynamics by which groups of ponds assemble at Espenberg, as well as reproducing the static patterns of ponds on old swales.

Stability of Ponds

Stable Ponds vs. Growing Lakes

Ponds at Espenberg are stable or grow slowly by peat decomposition, whereas the hypothesized first step in the formation of a thaw lake is the expansion of ponds by thawing and collapse of ice-rich frozen ground at their banks. The stability of ponds at Espenberg over hundreds of years is indicated by measures of their uniform size; if ponds were growing by slumping at their banks, ponds would have a wide range of sizes, as is observed for active thaw lakes (e.g. Sellman *et al.* 1975), and ponds set in old swales would be larger than ponds in young swales. However, the mean diameter of ponds is approximately independent of swale age (Figure 3.12). Over a 4 y period (7/1993 - 9/1996) in which the circumference of five ponds was measured at the elevation of lowest terrestrial vegetation, none of the ponds expanded. Slumping of material from the margin of a pond into its basin also was not observed at these or any other ponds at Espenberg

during this time. Moreover, the deep accumulation of shrub and moss peat in raised rings around ponds indicates that this vegetation community persists beside ponds for long periods of time, and so rates of lateral pond expansion are negligible.

In contrast to ponds, the size and frequency of lakes generally increases with surface age at Espenberg, indicating either that large lakes formed early in the development of old surfaces or that lakes are unstable and have grown through time. The absence of large lakes in young swales today and the permeability of unfrozen sand suggest that it is unlikely that large lakes have been present on young swales in the past. Moreover, enlargement of lakes is evident in patterns formed by breached ponds at lake margins (e.g. Figure 3.1C).

Size of Thermal Disturbance

One hypothesis for the stability of ponds at Espenberg is that the thermal disturbance caused by these ponds is too small to grow the pond laterally; specifically, that the maximum size of the seasonally-thawed margin of ground around the pond lies below a material-specific minimum value; $d < d_T$. If thawing exceeds d_T before the end of a summer, the now unfrozen peat can collapse into the body of water that caused the thermal disturbance and thereby enlarge its basin. To evaluate implications of this hypothesis, an estimate of the dependence of d on the size of a pond is needed.

Ice in a pond and in the surrounding frozen ground is melted during the thaw season by heat added to a pond through the pond surface. Little heat is added to the surrounding frozen ground by heat flux through the overlying seasonally frozen and thawed layer,

because this heat is spent in phase change within the active layer. Heat into the pond surface is transported downward, primarily by convection and advection in water and, over much longer time scales, by conduction downward in still-frozen ice. Heat is also conducted horizontally from the pond walls into the adjacent frozen ground, where it melts ice. Of the annual flux of heat that enters a pond surface, most is spent in melting ice in the pond and in the frozen ground because heat expended in temperature change is small compared to that for phase change in ice-rich frozen ground (Plug, 1994b; Hinzman *et al.*, 1998).

In this picture, the total volume of seasonally thawed ice in a pond and in adjacent frozen ground below the active layer is dependent on the total heat flux into the pond over a thaw season, Q_{T_p}. For a cylindrical pond with radius r_p and depth h (Figure 3.13), the heat budget over a thaw season for a pond and the surrounding frozen ground that melts can be approximated as

$$Q_{T_p}\pi r_p^{\,2} = L_f \pi h\left[r_p^{\,2} + \alpha\left(r_r^{\,2} - r_p^{\,2}\right)\right] \tag{7}$$

where L_f is the latent heat of fusion for water and r_r is the outer radius of the ground that thaws around the pond. The volumetric ice content of the frozen ground, α, is close to 60%, because that value is roughly the mean ice content of the upper 1.75 m of frozen peat at Espenberg. Since $d = r_r - r_p$, the horizontal distance across the seasonally thawed ground is

$$d = \left(r_p^2 \left(\left(\frac{Q_{T_p}}{L\rho h} - 1 \right) \frac{1}{\alpha} - 1 \right) \right)^{\frac{1}{2}} - r_p \quad . \tag{8}$$

In this representation, r_r is uniform with depth, an assumption supported by rapid transfer of heat downward into a pond vs. slow transfer from a pond into the surrounding ground (The thermal conductivity of ice is 3.85 $Wm^{-1}\,°C^{-1}$ and for frozen moist sedge peat, is 0.58 $Wm^{-1}\,°C^{-1}$. After thawing, convective transfer of heat, via water in the pond, to the underlying thaw front is rapid over the time scales considered here, while the thermal conductivity of sedge peat is 0.38 $Wm^{-1}\,°C^{-1}$ (all values from Hinzman *et al.*, 1991)). In Espenberg ponds, d decreases as a function of depth because some heat is lost to frozen ground around a pond as the ice in the pond thaws. The measured shape of thawed ground around ponds at the end of the thawing season is only roughly cylindrical because the extent of thawing is greater near the surface (e.g. Figure 3.5); therefore, the approach used here is only an approximation of the length scale of seasonal thawing of frozen ground around a pond.

Net fluxes across all boundaries other than the pond surface are assumed to be zero: the upward geothermal heat flux is negligible (0.4 Wm^{-2} compared to surface heat fluxes of order 100-300 Wm^{-2} during the thaw season in the subArctic) and horizontal conduction into frozen ground beyond the thawed region probably is small (horizontal thermal diffusion gradients in frozen ground are generally orders of magnitude smaller than vertical gradients (Hinzman *et al.*, 1998)). A pond is surrounded by permafrost that

rises above the wetland water table, therefore the heat transported by flow of water between a pond and the wetland surface is assumed to be negligible. For example, a bailed pond 1 m deep took 1.5 days to refill to within 0.2 m of its original level, demonstrating that even under hydraulic gradients many orders of magnitude larger than normal, water moves slowly through permafrost around ponds.

Heat flux into a pond surface available to thaw ice, Q_{Tp}, is a function of a net solar radiation flux to the pond surface and convective and evaporative fluxes (Figure 3.13), given by (e.g. Peixoto and Oort, 1992)

$$Q^{\downarrow}_{net_p} - Q^{\uparrow}_{C_p} - Q^{\uparrow}_{E_p} - Q_{T_p} = 0 \qquad (9)$$

where the net solar flux, $Q^{\downarrow}_{net_p}$, results from unreflected shortwave solar radiation minus the net long wave terrestrial and atmospheric radiation fluxes. Convective heat flux, $Q^{\uparrow}_{C_p}$, depends on surface roughness, wind speed and temperature gradient above the surface. Evaporative heat flux, $Q^{\uparrow}_{E_p}$, depends on humidity gradient and turbulence in wind above the surface.

Although no measurements of surface heat flux have been conducted in the region of the Espenberg beach-ridge plain, to my knowledge, these can be approximated from measurements at a similar site with similar surface type and summer climate. I use a measurement from a small lake in a sedge wetland near Baker Lake, Northwest Territories, Canada, a site which is north of tree line and near the southern margins of the zone of continuous permafrost. At the site, July daily mean temperature is 11.1°C and

mean depth of the active layer is 0.50 m (Roulet and Woo, 1986), comparable to that at Espenberg. $Q^{\downarrow}_{net_p}$ was measured at approximately 12 MJm^{-2} day^{-1} (Roulet and Woo, 1986) during late June through early August. Integrating over a 90 day thaw season at Espenberg (where snow cover ends in the beginning of June and freezing temperatures resume in early September (WRCC, 1999)) gives an estimate for heat flux of 1100 MJm^{-2}. An upper limit on $Q^{\uparrow}_{E_p}$ over the thaw season is the potential mean annual evaporation rate for the Northern Seward Peninsula region, which, at roughly 0.2 m y^{-1} (Baumgartner and Reichel, 1975), gives an evaporative heat flux of 670 MJm^{-2} y^{-1}. A value of 250 MJm^{-2} for $Q^{\uparrow}_{E_p}$ over the thaw season has been measured for coastal tundra at Barrow, Alaska (Mather, 1958; Waelbroeck, 1993). This value is probably a minimum limit for evaporative heat flux from a pond at Espenberg because Barrow is considerably cooler than Espenberg during the thaw season (mean July temperature is 5°C). Convective heat loss, $Q^{\uparrow}_{C_p}$, is probably small from ponds at Espenberg because the water surface is smooth on small ponds (Roulet and Woo, 1986) and because sheltering from raised rings reduces wind speed across pond surfaces. Based on the constraints that $Q^{\downarrow}_{net_p}$ $\approx$ 1100 MJm^{-2}, $Q^{\uparrow}_{E_p} \approx$ 400 MJm^{-2} and $Q^{\uparrow}_{C_p} \approx$ 100 MJm^{-2}, I use a reference value for Q_{T_p} of 600 MJm^{-2}. Sensitivity of results to this value is described in the next section.

Results

Results of heat flux calculations using reference model values for Q_{T_p} and α are consistent with measurements of thawed ground around the bailed pond near the close of a thaw season (Figure 3.5). A pond of the typical 2 m diameter and 1 m depth has a calculated value for d of approximately 0.5 m (Figure 3.14A), comparable to the measured distance across thawed peat around the bailed pond near the end of the thawing season. This suggests that the simple approach used here can give reasonable estimates of the extent of thawing around a pond.

The predicted value of d is sensitive to heat flux into a pond surface and to ice-content of adjacent frozen ground (Figure 3.14B-C). The thawed margin around a pond increases with an increase in net heat flux into a pond, which can be caused by an increase in direct solar radiation or by a decrease in convective and evaporative fluxes away from the surface. Increases in volumetric ice content decrease the maximum extent of horizontal thaw because of the higher total latent heat content of adjacent frozen ground.

The predicted value of d is highly sensitive to the dimensions of a pond (Figure 3.14A). Shallow ponds with large surface area cause a large thermal disturbance in surrounding frozen ground (d is large) because total heat flux into the pond is great compared to the volume of ice in the pond to be melted. In deep, narrow ponds, d is small because the total latent heat of ice in the pond is large whereas the insolated surface area of the pond is small. For ponds at Espenberg of measured depth and diameter, the

predicted value of d is less than 0.6 m, whereas the size of the thawed region around ponds of larger diameter is greater (Figure 3.14A). This result is consistent with the hypothesis that ponds in ice-rich frozen ground at Espenberg persist because the dimensions of these ponds are such that the extent of thaw at their margins is too small to lead to growth by thaw-driven collapse ($d < d_T$), whereas lakes, which are larger, can expand by unstable thawing of frozen ground at their margins.

Discussion

Ponds with roughly cylindrical bathymetry of diameter 2 m and depth 1 m, called whale-hole ponds, form through an interaction between differential accumulation and degradation of peat and the thawing of ice-rich permafrost, as shown by stratigraphy and distribution of ponds and by active peat decomposition. Raised rings around ponds form by rapid accumulation of peat beneath shrub and moss vegetation and by frost heaving. In a rule-based model that encapsulates a hypothesized interaction between raised rings and the formation of a new pond, groups of ponds assemble in a sequence similar to that shown by groups of ponds on surfaces of increasing age at Espenberg. This model can better account for the pattern of spacings between ponds than other mechanisms, as shown by K-S comparisons of the distribution of spacings between modeled and Espenberg ponds.

The stability of ponds at Espenberg, coupled with the sensitivity of the size of a thermal disturbance caused by a pond on the pond's size, indicates that a thaw lake cannot initiate from disturbances below a minimum threshold size. In ice-rich frozen

peat, this threshold size is apparently greater than the size of stable ponds at Espenberg (diameter ≤ 4 m) and less than the size of lakes at Espenberg (diameter > 10 m). Depth of a pond might also play an important role in initiation of a thaw lake through unstable thawing, as the calculated size of thermal disturbance around a pond is dependent on pond depth as well as diameter. Distance across the thawed region of frozen ground decreases with increasing depth of a pond, because the volume of ice in the pond increases with respect to the surface area. Ice in the pond is preferentially melted because the transport of heat is much faster to ice in a pond than to ice in frozen ground. The minimum size of a pond necessary to initiate a thaw lake is likely material dependent. Thawing of frozen ice-rich silt, for example, releases water that can be trapped within the soil by its low hydraulic conductivity. This trapped water elevates pore-water pressures and aids gravity slumping (McRoberts and Morgenstern, 1974). For a material of this type, with little coherence on thawing, the stable size of a thermal disturbance is likely to be smaller than that in ice-rich fibrous peat at the Espenberg beach-ridge plain. Not all perturbations in seasonal thawing lead to the development of a thaw lake in ice-rich silt terranes, suggesting that this substrate also has a threshold disturbance size below which the a disturbance does not lead to unstable growth. Determination of the threshold size of disturbance for this and other thaw-susceptible permafrost, by examination of disturbances in ice-rich frozen ground that do not grow, would be useful.

The growth of a pond through gravity-slumping at its margins is irreversible. This observation, in combination with the sensitivity of the extent of thermal disturbance in

frozen ground on the size of a pond, suggests that instability of ponds at Espenberg and elsewhere can be triggered by extreme events. For example, ponds below their maximum stable size (with respect to mean summer conditions) might enlarge by slumping in response to a single very warm summer. Because surface area of, and hence heat flux into, the pond is increased, horizontal expansion of the pond might continue during following summers with mean climate. This issue, and the expansion of unstable ponds into lakes through thawing, subsidence and collapse cannot be addressed by a model for equilibrium stability of ponds. An approach that coupled thawing of heterogeneous frozen ground and enlargement of ponds by bank erosion and subsidence would be useful.

Acknowledgments

This manuscript benefited from reviews by D.M. Hopkins, O.K. Mason, D. Kane, J. Beget (all at UAF), B.T. Werner (UCSD) and K. Tae (San Diego State University). D. Mann, M. Rouleau, K. Tae, L. Tae, T. Tannenbaum and Buck Maxson provided cheerful assistance at Espenberg. Coring equipment was loaned by M. Kunz at the Fairbanks office of the Bureau of Land Management. Supported by the National Park Service, Bering Land Bridge National Preserve (Espenberg/Thaw-lake subcomponent of the Beringian Shared Heritage Project to D.M. Hopkins and L.J. Plug) and the National Science Foundation, Arctic Natural Sciences Program (OPP-9530860 to B.T. Werner).

Appendix -- Sampling Methods

pH of water was measured for 18 ponds and from water squeezed from peat in 10 raised rings. Dissolved oxygen measurements were taken from 6 areas of shallow

degrading peat. Dissolved oxygen and pH was measured in the field using a calibrated Corning Checkmate meter accurate to ± 0.01 pH and ± 1% DO. Sample containers were rinsed three times with the sampling water before measurement.

Active layer depth, depth to permafrost and depth of ponds were measurements with a 1.8 m steel rod. Morphologic measurements in Section 3 are for 20 ponds. Error is the standard deviation of the sample. All botanical names follow those of Hultén, 1968.

References

Aleshinskaya, Z.V., Bondarev, L.H. and Gorbunov, A.P. (1972). Periglacial phenomena and some palaeo-geographical problems of Central Tien-Shan. *Biuletyn Peryglacjalny* **21**, 5-14.

Baumgartner, A. and Reichel, E. (1975). "The World Water Balance." Elsevier, Amsterdam.

Billings, W.D., and Peterson, K.M. (1980). Vegetational change and ice-wedge polygons through the thaw-lake cycle in arctic Alaska. *Arctic and Alpine Research* **12**, 413-432.

Boatman, D.J., Goode, D.A. and Hulme, P.D. (1981). The Silver Flowe III. Pattern development on Long Loch B and the Craigeazle Mires. *Journal of Ecology* **69**, 897-918.

Britton, M.E. (1957). Vegetation of the arctic tundra. *In* "Arctic Biology." (H.P. Hansen, Ed.), pp. 26-72. Oregon State University Press, Corvallis.

Foster, D.R., King, G.A., Glaser, P.H. and Wright H.E. Jr., (1983). Origin of string patterns in boreal peatlands. *Nature* **306**, 256-258.

Foster, D.R., and King, G.A. (1984). Landscape features, vegetation and developmental history of a patterned fen in south-eastern Labrador, Canada. *Journal of Ecology* **72**, 115-143.

Foster, D.R., Wright, H.E. Jr., Thelaus, M., and King, G.A. (1988). Bog development and landform dynamics in central Sweden and south-eastern Labrador, Canada. *Journal of Ecology* **76**, 1164-1185.

French, H.M. (1974). Active thermokarst processes, eastern Banks Island, Western Canadian Arctic. *Can. J. Earth Sci.* **11**, 785-94.

French, H.M. (1987). Periglacial geomorphology in North America: current research and future trends. *Progress in Physical Geography* **11**, 569-587.

French, H.M. (1996). "The Periglacial Environment." Addison Wesley, Harlow.

Heginbottom, J.A. (1973). "Effects of surface disturbance upon permafrost." Report 73-16, Task Force on Northern Oil Development, Information Canada, Ottawa.

Hinzman, L.D., Kane, D.L., Benson, C.S., and Everett, K.R. (1991). Hydrologic and thermal properties of the active layer in the Alaskan Arctic. *Cold Reg. Sci. and Tech.* **19**, 95-110.

Hinzman, D.L., Goering, D.J., and Kane, D.L. (1998). A distributed thermal model for calculating soil temperature profiles and depth of thaw in permafrost regions. *J. Geophys. Res.* **103**, 28,975-28,991.

Hopkins, D.M. (1949). Thaw lakes and thaw sinks in the Imuruk Lake area, Seward Peninsula, Alaska. *Journal of Geology* **57**, 119-131.

Hultén, E. (1968). "Flora of Alaska and Neighboring Territories." Stanford University Press, Stanford.

Jorgenson, M.T., Shur, Y., and Walker, H.J. (1998). Evolution of a permafrost-dominated landscape on the Colville River Delta, northern Alaska. *In* "Proceeding of the Seventh International Conference on Permafrost", (A.G. Lewkowicz and M. Allard, Eds.), pp. 523-530. University of Laval, Quebec.

Kerfoot, D.E. (1974). Thermokarst features produced by man-made disturbances to the tundra terrain. *In* "Research in Polar and Alpine Geomorphology Proceedings, Third Guelph Symposium on Geomorphology", pp. 60-72.

Kirkpatrick, S., Gelatt C.D. Jr., and Vecchi, M.P. (1983). Optimization by simulated annealing. *Science* **220**, 671-680.

Kling, G.W., Kipphut, G.W., and Miller, M.C. (1991). Arctic lakes and streams as gas conduits to the atmosphere; implications for tundra carbon budgets. *Science* **251**, 298-301.

Mackay, J.R. (1970). Disturbances to the tundra and forest tundra environment of the western Arctic. *Canadian Geotechnical Journal* **7**, 420-432.

Mackay, J.R. (1986). The first 7 years (1978-1985) of ice wedge growth, Illisarvik experimental drained lake site, western Arctic coast, *Can. J. Earth Sci. 23,* 1782-1795.

Mason, O.K., Hopkins, D.M. and Plug, L.J. (1997). Chronology and paleoclimate of storm-induced erosion and episodic dune growth across Cape Espenberg Spit, Alaska, U.S.A. *Journal of Coastal Research* **13**, 770-797.

Mather, J.R. (1958). "Microclimate investigations at Point Barrow, Alaska, 1957-1958." Drexel Institute of Technology, Publications in Climatology, 11(2), 63-239.

McRoberts, E.C., and Morgenstern, N.R. (1974). The stability of thawing slopes. *Can. Geotechnical J.* **11**, 447-469.

Merton, J.B., (1996). Thermokarst-lake-basin sediments, Tuktoyaktuk Coastlands, western arctic, Canada. *Sedimentology* **43**, 737-760.

NPS (National Park Service) (1986). Near-infrared aerial photographs of coastal regions of the Bering Land-Bridge National Preserve, Anchorage.

NOAA (National Oceanographic and Atmospheric Administration) (1999). Unedited Local Daily Climatological Data for Kotzbue Ralph Wein Memorial Airport, Alaska.

Piexoto, J.P. and Oort, A.H. (1992). "Physics of Climate." American Institute of Physics, New York.

Plug, L.J. (1994a). Chronosequence Of Geomorphic Evolution In A Beach-Ridge Wetland In Northwest Alaska. Proceedings of the Arctic Workshop. Institute of Arctic and Alpine Research, Boulder.

Plug, L.J. (1994b). Active-layer depths during Full Glacial conditions for Fairbanks, Alaska. *Current Research in the Pleistocene* **11**, 146-148.

Plug, L.J., and Werner, B.T. (in revision) Fracture networks in frozen ground. *Journal of Geophysical Research.*

Press, W.H., Flannery, B.P., Teukolsky, S.A., and Vetterling, W. T. (1988). "Numerical Recipes in C." Cambridge University Press, Cambridge.

Rampton, V.N. (1988). Quaternary Geology of the Tuktoyaktuk Coastlands, Northwest Territories. *Geological Survey of Canada Memoir* **423.**

Robinson, S.D. and Moore, T.R. (1999). Carbon and peat accumulation over the past 1200 years in a landscape with discontinuous permafrost, northwestern Canada. *Global Biogeochemical Cycles* **13**, 591-601.

Roulet, N.T., and Woo, M. (1986). Wetland and lake evaporation in the low Arctic. *Arctic and Alpine Research* **18**, 195-200.

Ruz, M.-H., Héquette, A., and Hill, P.R. (1992). A model of coastal evolution in a transgressed thermokarst topography, Canadian Beaufort Sea. *Marine Geology* **106**, 251-278.

Schaaf, J. and Barker, M. (nd). Vegetation study along transect IV at Cape Espenberg. Unpublished report, Bering Land-bridge National Preserve, National Park Service, Anchorage, Alaska.

Schwoerbel, J. (1987). "Handbook of Limnology." Ellis Horwood, Chichester.

Seguin, M.K. and Allard, M. (1984). Le pergelisol et les processus thermokarstiques de la région de la Rivière Nastapoca, Nouveau Quebec. *Geographie Physique et Quaternaire* **38**, 11-25.

Sellman, P.V., Brown, J., Lewellen, R.I., McKim, H., and Merry, C. (1975). "The classification and geomorphic implications of thaw lakes on the Arctic coastal plain, Alaska." United States Army, Cold Regions Research and Engineering Laboratory, Report No. 344, 21p.

Seppälä, M. (1982). An experimental study of the formation of palsas. *In* "Proceedings: 4th Canadian Permafrost Conference, Calgary, Alberta." (H.M. French, Ed.) pp. 36-42, National Research Council, Ottawa.

Seppälä, M. (1986). The origin of palsas. *Geografiska Annaler* **68A**, 141-147.

Seppälä, M. (1994). Snow depth controls palsa growth. *Permafrost and Periglacial Processes* **5**, 283-288.

Seppälä, M. and Koutaniemi, L. (1985). Formation of string and pool topography as expressed by morphology, stratigraphy and current processes on a mire in Kuusamo, Finland. *Boreas* **14**, 287-309.

Sjors, M. (1963). Bogs and fens on Attawapiskat River, northern Ontario. *Nat. Mus. Can. Bull.* **186**, 1-133.

Tomirdiaro, S.V. (1982). Evolution of lowland landscapes in northeastern Asia during Late Quaternary time. *In* "Paleoecology of Beringia" (D.M. Hopkins, Ed.) pp. 29-41. Academic Press, New York.

Ugolini, F. (1975). Ice-rafted sediment as a cause of some thermokarst lakes in the Noatak River Delta, Alaska. *Science* **188**, 51-53.

Waelbroeck, C. (1993). Climate-soil processes in the presence of permafrost: a systems modelling approach. *Ecological Modelling* **69**, 185-225.

Walker, H.J. (1978). Lake tapping in the Colville River delta. *In* "International Conference on Permafrost, Proceedings" pp. 233-238. National Academy Press, Washington.

Werner, B.T. (1999). Complexity in natural landform patterns. *Science* **284**, 102-104.

Williams, P.J., and Smith, M.W. (1991). "The Frozen Earth: Fundamentals of Geocryology." Cambridge University Press, Cambridge.

Worsley, P., Gurney, S.D., and Collins, P.E.F. (1995). Late Holocene 'mineral palsas' and associated vegetation patterns: a case study from Lac Hendry, Northern Quebec, Canada and significance for European Pleistocene thermokarst. *Quaternary Science Reviews* **14**, 179-192.

WRCC (Western Regional Climate Center) (1999). Kotzebue WSO Airport, Alaska Climate Summary, 9/1/1949 to 12/31/1998, http://www.wrcc.dri.edu.

Zoltai, S.C. (1993). Cyclic development of permafrost in the peatlands of northwestern Alberta, Canada. *Arct. Alp. Res.* **25**, 240-246.

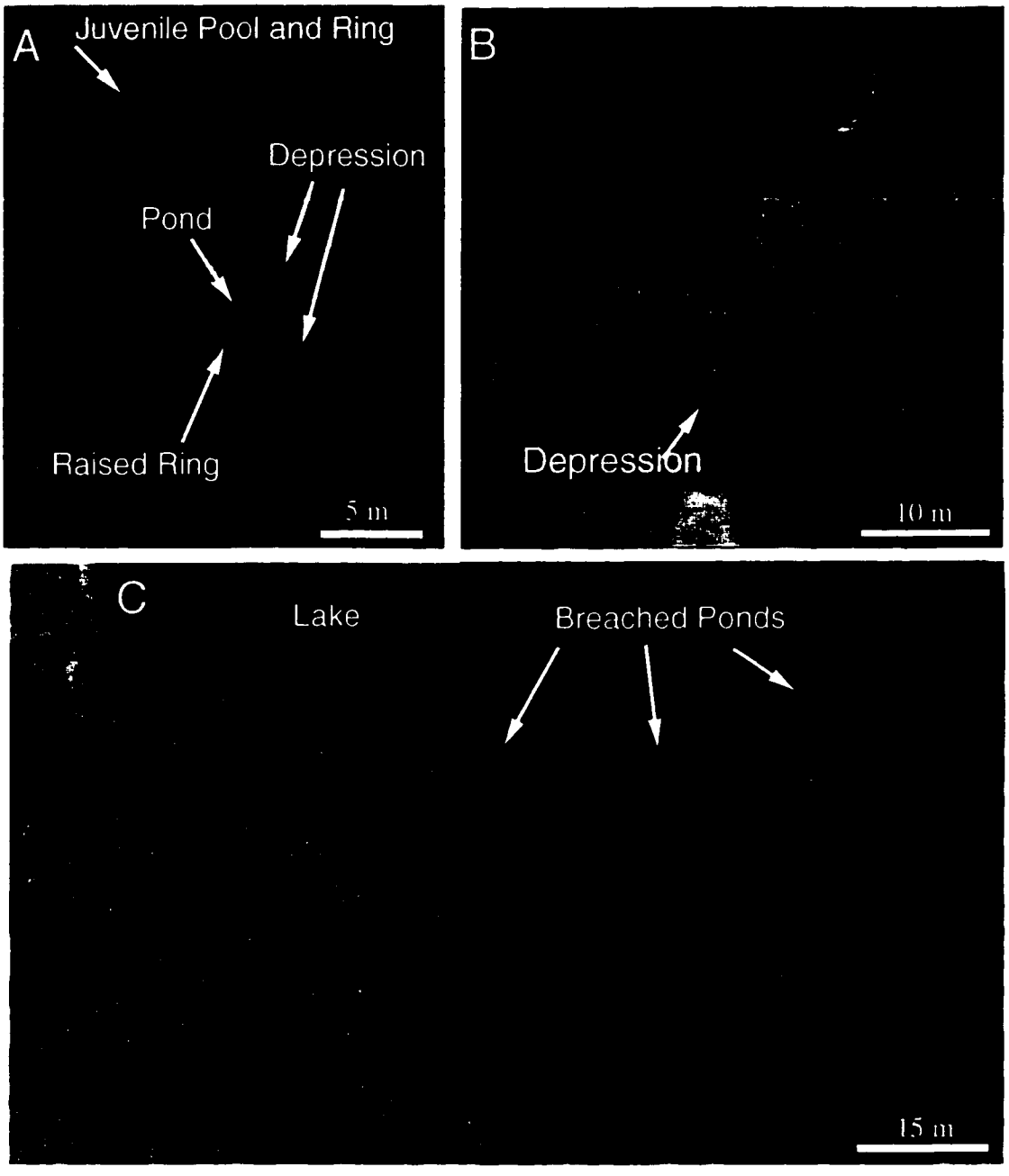

FIGURE 3.1. Near-infrared aerial photographs of ponds in permafrost wetlands on the Espenberg beach-ridge plain. Deep water in ponds is black. Areas of shallow standing water and wet fen vegetation are dark gray. Raised rings around ponds appear light

because they are dry and covered by shrubs and lichen. *(A)* A single pond surrounded by a raised ring 0.5 m high. Shallow pools formed by differential accumulation of peat are adjacent to the ring, possibly marking the onset of new ponds. *(B)* Small group of ponds near the center of a swale approximately 1500 years old. *(C)* Large group of ponds located between two lakes in a wide swale approximately 3300 years old. The lake margin is frilled by pond basins that have been breached by the expanding lake. Images are enlarged from 1:6000 scale photographs provided by the National Park Service (NPS, 1987).

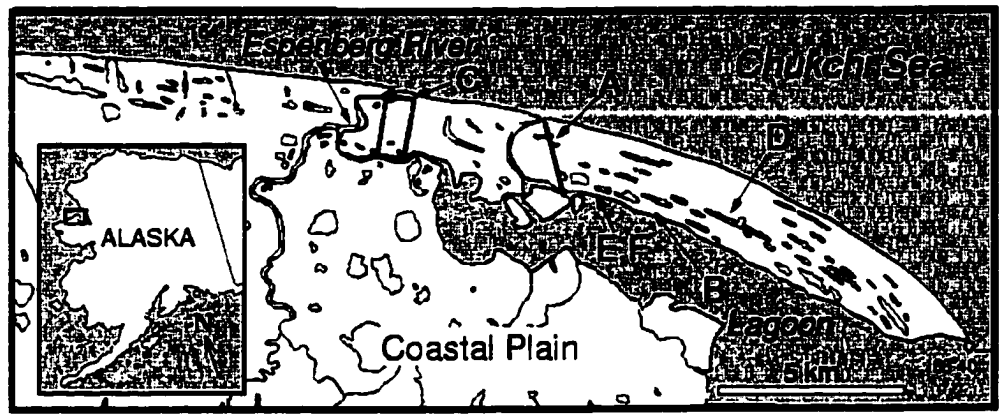

FIGURE 3.2. The Espenberg beach-ridge plain is a shore-attached sandy spit that has aggraded during the Late Holocene. Sites described in text are shown: (A) transect of elevation, pond distribution and peat depth across the beach-ridge plain (Figure 3.3); (B) 2 m core (Table 3.1); (C) Region shown in Figure 3.4; (D) bailed pond (Figure 3.5); (E) pond basin, thawed and partly revealed in profile by erosion of peat along the lagoon bluff (Figure 3.6); (F) excavated pond basin and ring approximately 2 m from the lagoon bluff, drained and thawed by landward melting of permafrost (Figure 3.7).

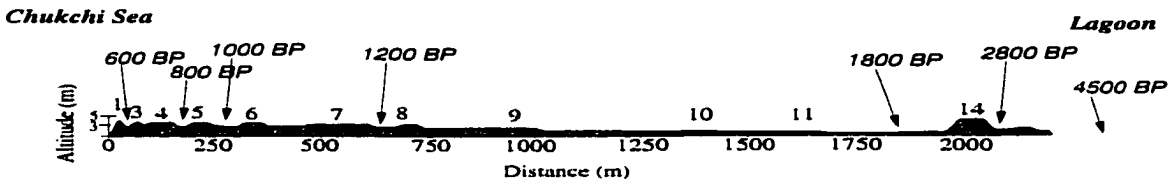

FIGURE 3.3. Chronology and elevation for transect A (Figure 3.2) across the Espenberg beach-ridge plain. Altitudes are meters above low tide, measured in a closed survey using an optical theodolite. Ridges are numbered according to the classification scheme described in Mason et al., 1997. Italicized numbers with arrows are estimated ages of swales. The oldest swale at Espenberg (radiocarbon age 4480 ± 80 (β-67696)) is absent from the region crossed by this transect because of erosion at the lagoon bluff. Swales ages are estimates based on 55 radiocarbon ages from archaeology, marine shells and buried soils in beach ridges and on driftwood and basal peats in swales (compiled in Mason et al., 1997).

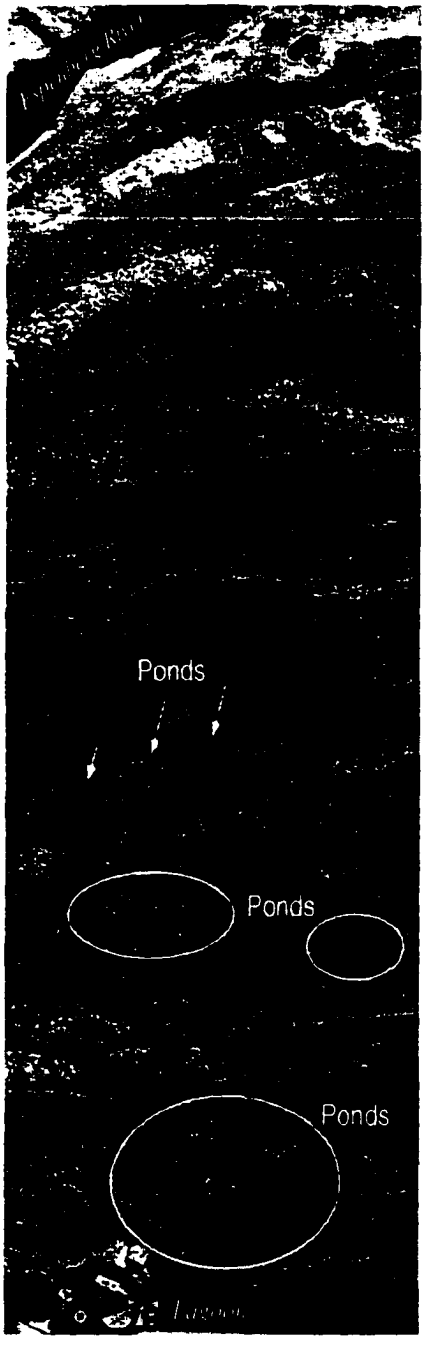

FIGURE 3.4. Example of the distribution of ponds across the Espenberg beach-ridge plain. At the top of the photo is the mouth of the Espenberg River. At the bottom of the photo is a tidal channel leading to the Espenberg lagoon. Ponds occur as single ponds or in small groups on young swales. The size of groups of ponds increases with swale age.

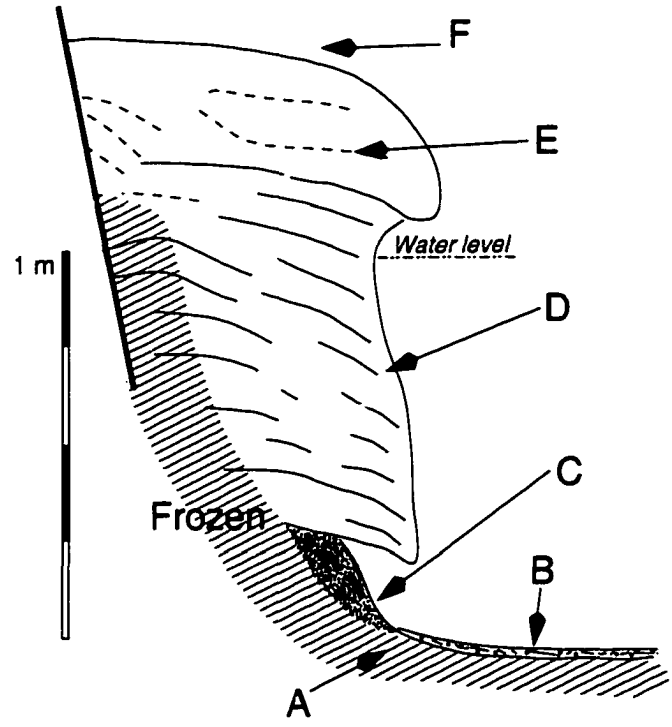

FIGURE 3.5. Stratigraphy and position of the thaw front in the wall of a bailed pond: (A) Frozen silty sand; (B) Unconsolidated and unfrozen mat primarily of woody stems and ericad leaves; (C) Unfrozen medium sand with wood fragments up to 20 × 2 cm and rare monocot stems; (D) Layered sedge peat dipping at 15° into the pond basin; (E) Moss and shrub peat with mineral-rich involutions; (F) Modern vegetation. Pond was bailed and the extent of thawing measured August 29, near the close of the thawing season. Scale is for vertical and horizontal directions.

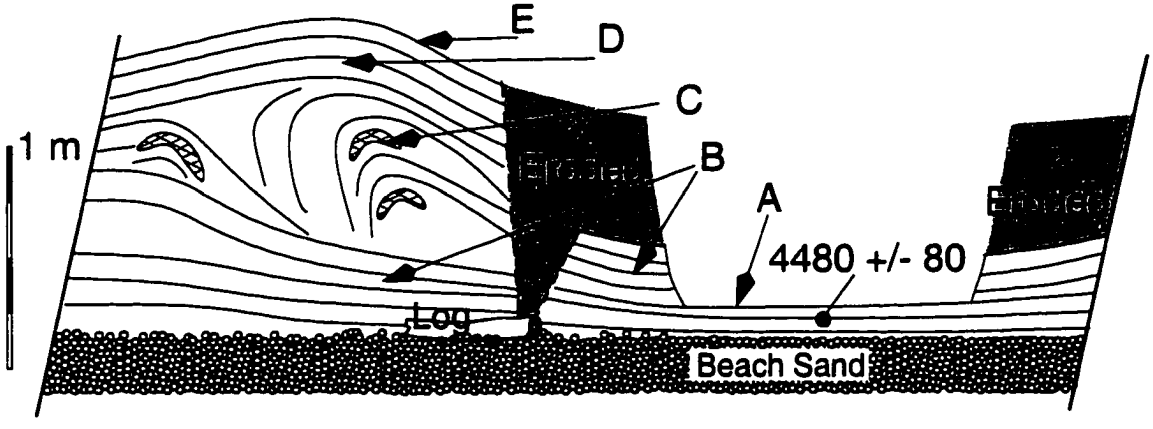

FIGURE 3.6. Eroded pond basin and ring exposed in section at the lagoon bluff: (A) Horizontally layered peat floor of pond (round in plan view) continuous with peat in adjacent ring. A twig set into peat dates to 4480 ± 80 BP; (B) Horizontally layered sedge peat with vertically decreasing fraction of intermixed sand; (C) Folded sedge and shrub/sphagnum peat with inclusions of mineral rich and highly humified material; (D) Mixed shrub/sphagnum and sedge peat; (E) Modern vegetation of ericaceous shrubs and moss.

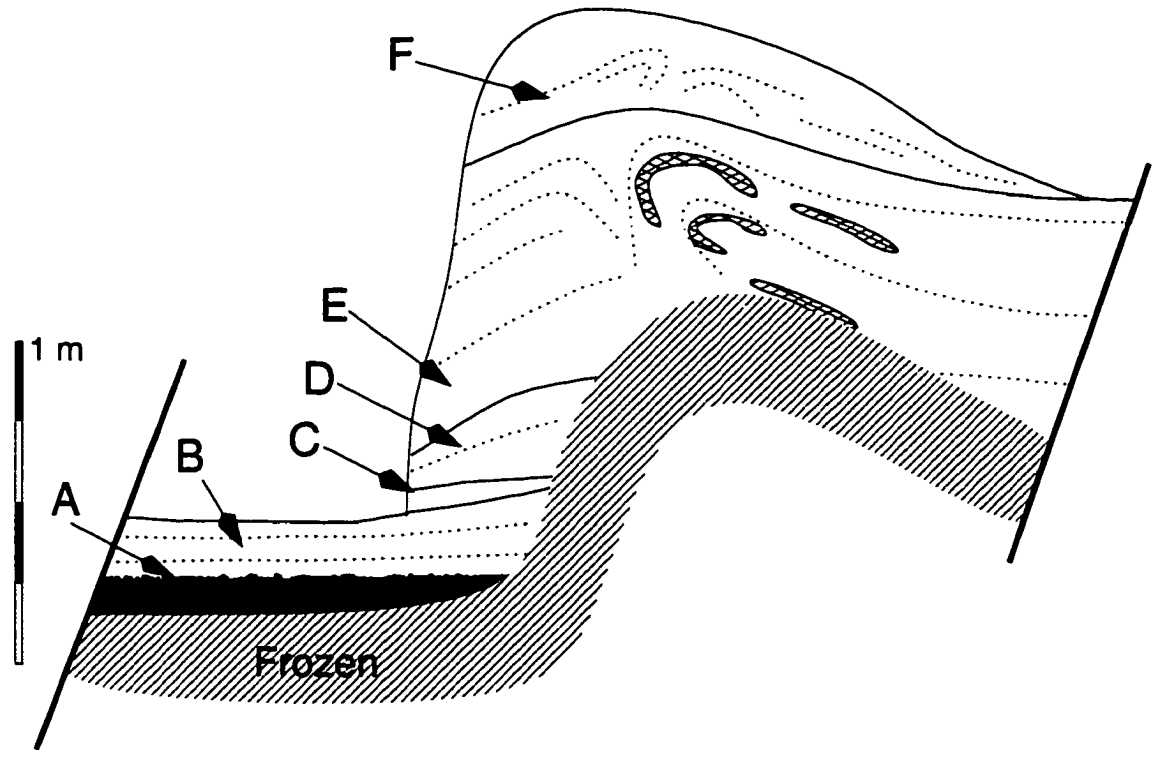

FIGURE 3.7. Basin and raised ring of a naturally drained pond near the lagoon bluff. The frost table represents its position at the end of the excavation, which is probably much deeper than its seasonal maximum pre-drained position because of landward thawing from the nearby (~1 m) lagoon bluff. (A) Sand with wood fragments; (B) Poorly decomposed sedge and moss peat, continuous beneath floor of pond and into walls; (C) Sand with intermixed organics; (D) Poorly decomposed sedge and shrub peat; (E) Well-decomposed peat with sedge fragments common, rich in intermixed sand and sandy layers; (F) Shrub and moss peat.

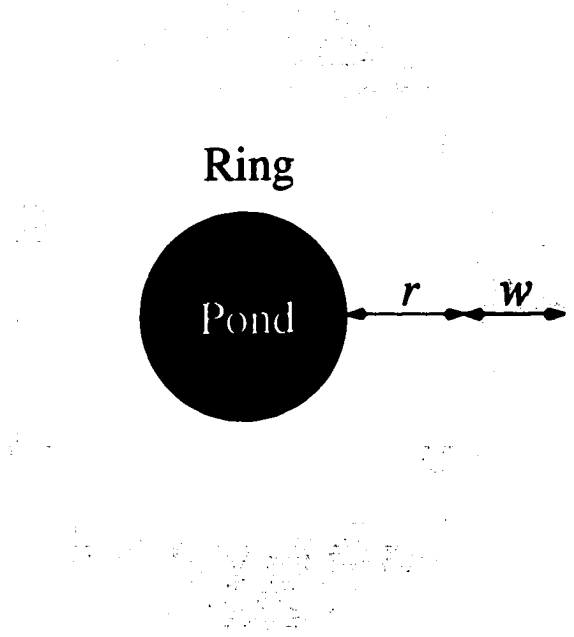

FIGURE 3.8. Representation of ponds and rings in a rule-based model for the sequential placement of ponds. Each raised ring (width *r*) is surrounded by an annulus *w* wide, in which the probability that a new pond will form is enhanced vs. probability of pond forming at other positions in the modeled swale.

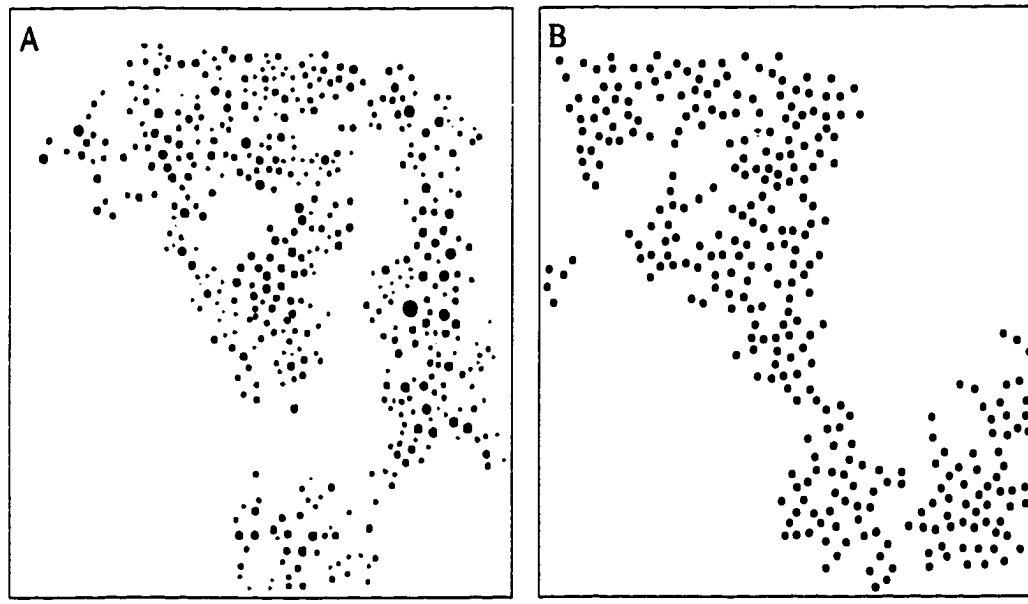

FIGURE 3.9. Examples of groups of ponds compared using K-S comparisons of pond spacing distributions: *(A)* digitized Espenberg; *(B)* self-organization model.

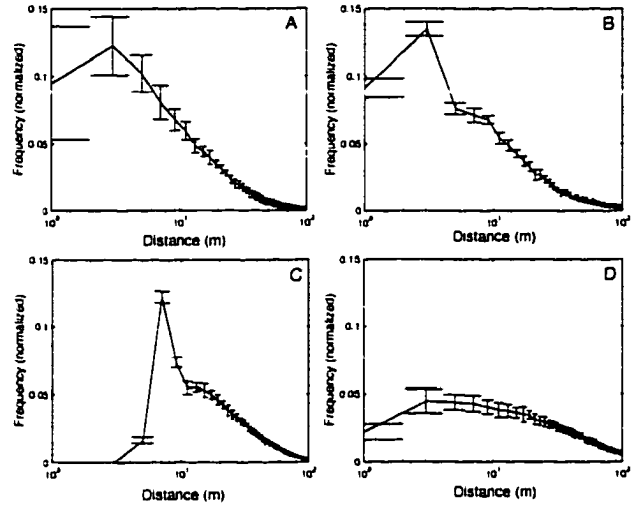

FIGURE 3.10. Distributions of spacing between ponds in groups drawn from *(A)* Espenberg (4 groups); *(B)* self-organization model (20 groups); *(C)* random-spaced (20 groups); *(D)* random (20 groups). Espenberg and self-organization model distributions are qualitatively similar.

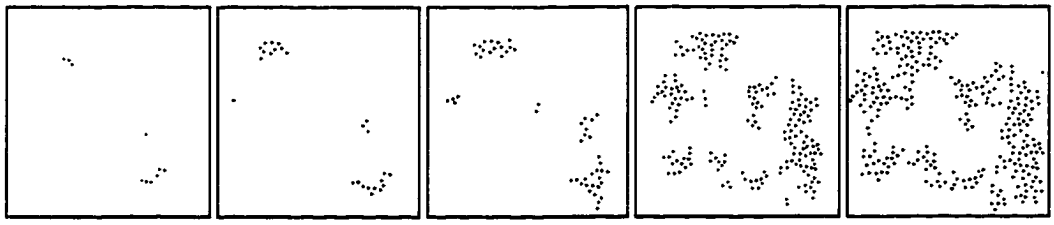

FIGURE 3.11. Development of a modeled group of ponds through addition of new ponds. The first ponds are widely distributed and isolated because all areas are equally likely to develop a new pond. Most subsequent ponds appear around these early ponds because of greater probability at these positions, as modeled with a Boltzman distribution, which encapsulates an hypothesized mechanism for interaction between elevated rings around ponds and the development of a new pond through differential accumulation of peat. The final pattern of ponds (where the number of ponds has reached an imposed maximum) has irregular spacings because of suboptimal packing of ponds, which arises through sequential placement of ponds, and because of joining of subgroups of ponds. This sequence is qualitatively similar to the development of groups of ponds at the Espenberg beach-ridge plain.

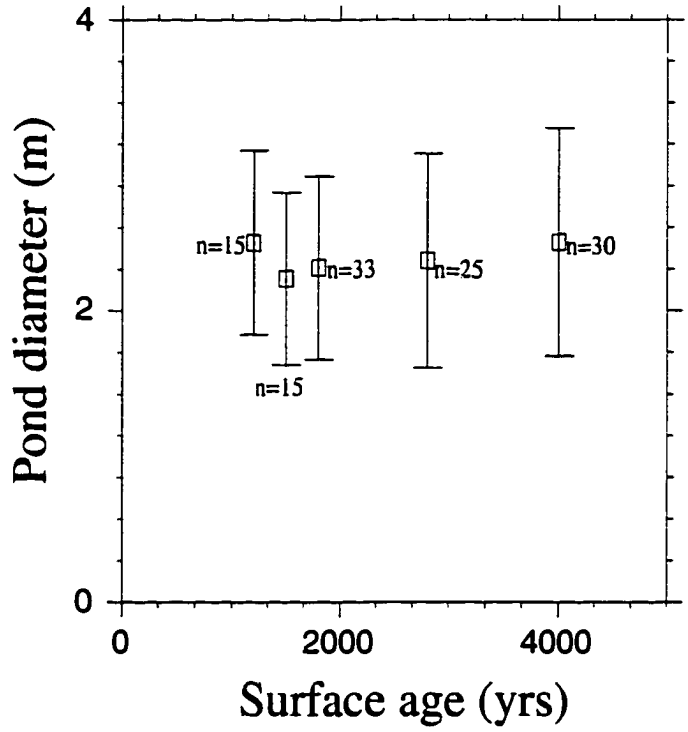

FIGURE 3.12. Diameter of ponds vs. swale age, as measured from enlargements of 1:6000 near-infrared aerial photographs (NPS, 1987). Ponds have a characteristic diameter of roughly 2 m, independent of swale age.

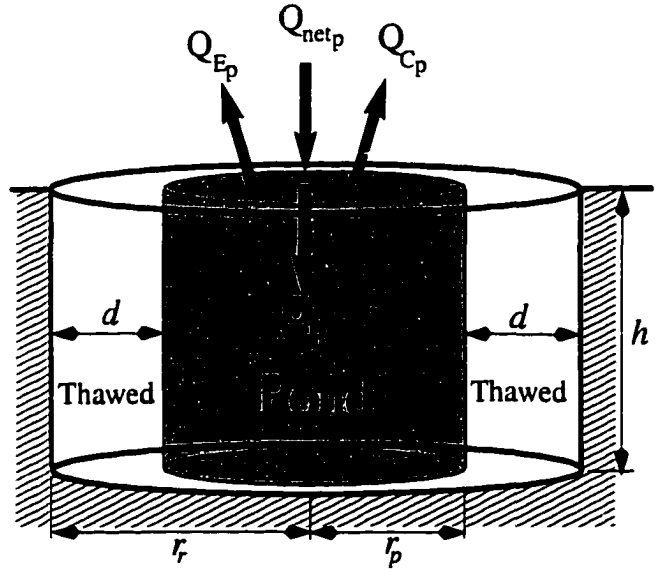

FIGURE 3.13. Representation of a pond and surrounding frozen ground in a heat flux calculation.

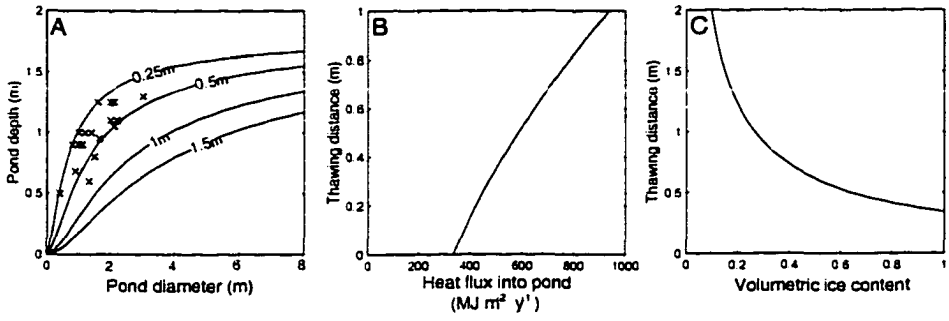

FIGURE 3.14. Sensitivity of the distance across the seasonally-thawed frozen ground around a pond to parameters in a heat flux calculation: *(A)* Contours of horizontal thaw distance around a pond (*d*) as a function of the diameter and depth of a pond. Ponds with small diameter have less insolated surface and so less heat is available to drive thawing of ice in the adjacent frozen ground. Horizontal thawing is greater around a shallow pond than a deep pond, because the surface area of the pond bed is decreased. The calculated thaw distance for ponds measured at Espenberg (shown by × marks) are generally less than 0.5 m; *(B)* Sensitivity of calculated thaw distance to net radiation flux over a thaw season into the pond; *(C)* Sensitivity of calculated thaw distance to the volumetric ice content of frozen ground around the pond.

Ice content and stratigraphy of frozen samples in a ore from a peat-filled swale.

Sample Depth *(cm)*	C *(%)*	Description
42-51	49	Sedge fragments and rootlets mixed with medium sand
61-70	46	Sedge peat
81-90	57	Humified sedge peat with intermixed sand and 0.5 - 1 cm ice lenses.
93-102	50	Humified sedge peat with intermixed sand and 0.5 - 1 cm ice lenses.
106-115	63	0.5 - 2 cm ice lenses, humified sedge peat with intermixed sand.
131-140	33	Humified sedge peat with <1 cm sandy layers
149-158	38	Sedge peat with sandy layers
166-175	39	Sedge peat with sand throughout
175 - ??	nd	Sand with < 0.5 cm thick organic-rich horizontal stringers

TABLE 3.1. Ice content (C) and stratigraphy of frozen samples from a core taken in a peat-filled swale at the Espenberg beach-ridge plain (Site A). Swale is approximately 4500 years old. Core was extracted with CRREL ice coring equipment. Consolidation (C) is the measured reduction in volume of a 9 cm long by 7.6 cm diameter cylindrical frozen core sample after thawing and tamping with a 5 kg weight. Samples were tamped because peat is highly compressible on thawing (Williams and Smith, 1991).

Similarity of different realizations of groups of ponds drawn from the same set, as evaluated by K-S comparisons of spacing distributions.

	P
Espenberg - Espenberg (4)	0.14 ± 0.2
Self-organization Model - SO Model (10)	0.4 ± 0.3
Random - Random (20)	0.5 ± 0.3
Random spaced - Random spaced (20)	0.5 ± 0.3

TABLE 3.2. Similarity of different realizations of groups of ponds drawn from the same set, as evaluated by Kolmogorov-Smirnov (K-S) comparisons of spacing distributions. Small values of *P* indicate a significant difference between two groups of ponds. Model parameters are given in Table 3.3.

Results of fitting self-organization model, random-spaced and random groups of ponds to four groups of ponds at Espenberg.

	Self-organization model groups					Random-spaced groups			Random groups	
	P	*r(m)*	*w(m)*	*n*	*Trandom*	*P*	*r*	*n*	*P*	*n*
Espenberg group 1 (n=505)	0.12	3.2	3.8	414	0.21	<0.0001	6.7	408	<0.0001	105
Espenberg group 2 (n=196)	0.13	3.7	3.1	295	0.32	<0.0001	5.4	500	<0.0001	177
Espenberg group 3 (n=522)	0.09	3.5	2.9	510	0.29	<0.0001	6.6	219	<0.0001	245
Espenberg group 4 (n=379)	0.15	3.2	3.3	327	0.33	<0.0001	6.1	195	<0.0001	227

TABLE 3.3. Results of fitting self-organization model, random-spaced and random groups of ponds to four groups of ponds at Espenberg. P is the confidence interval for the null hypothesis that the two groups of ponds are significantly different. $P > 0.1$ implies that two groups of ponds are similar. Model parameters r and w are as shown in Figure 3.6, n is the total number of ponds placed into a group and T_{random} is the degree of randomness in the mechanism for pond placement, as modeled by a Boltzmann function. Some self-organization modeled groups of ponds are indistinguishable from Espenberg groups of ponds, at the level of variation amongst groups of ponds at Espenberg. Random and random-spaced models, using best-fit parameters, generate groups of ponds that are clearly different from groups of ponds at Espenberg. The consistency of model parameters across the four realizations of the self-organization model (each fitted to a different groups of ponds at Espenberg) is consistent with the hypothesis that groups of ponds at Espenberg similarly self-organize because raised rings around ponds locally depress peat accumulation rates, thereby favoring the initiation of a new adjacent pond.